In vitro measurements of immunogenic cell death after radiation treatment combined with ATR inhibition

Potential effects on anti-cancer immunity

Adrian Eek Mariampillai

Thesis for the degree of
Master of Science in Molecular Biosciences
60 credits

Department of Biosciences
Faculty of Mathematics and Natural Sciences

UNIVERSITY OF OSLO

May 2018

Oslo University Hospital

In vitro measurements of immunogenic cell death after treatment with radiation combined with ATR inhibition:

Potential effects on anti-cancer immunity

2018

In vitro *measurements of immunogenic cell death after radiation treatment combined with ATR inhibition: Potential effects on anti-cancer immunity*

Adrian Eek Mariampillai

http://www.duo.uio.no/

Print: Reprosentralen, Universitetet i Oslo

Abstract

Radiation therapy is widely used to treat cancer, and exerts its cytotoxic effects by inducing DNA damage. However, radiation therapy may also partially promote systemic anti-tumour effects through induction of immunogenic cell death (ICD). ICD is characterised by the three hallmark factors surface presentation of calreticulin (ecto-CRT), secretion of ATP and exodus of HMGB1 from the nucleus, which together stimulate systemic T-cell responses towards tumour-associated antigens. In this project, we hypothesised that co-treatment of cancer cells with radiation and inhibitors of the ATR cell cycle checkpoint kinase can cause increased ICD signalling compared to radiation treatment alone. Inhibition of ATR abrogates the G_2/M cell cycle checkpoint, thereby resulting in more mitotic catastrophe, and hence more death which potentially may be immunogenic.

We optimised methods for *in vitro* detection of the aforementioned hallmarks in H1975 lung cancer cells and U2OS osteocarcoma cells. Ecto-CRT was measured by flow cytometric analysis of live cell samples barcoded with permeable Hoechst 33342 and stained with anti-CRT antibody. ATP was spectrophotometrically measured in the culture medium supernatant of treated samples, after a two-step centrifugation, by use of the *CellTiter-Glo* reagent. HMGB1 exodus was flow cytometrically monitored by loss of intracellular GFP signals in cells transiently transfected with *GFP-HMGB1*. At 24-72 hours after treatment of H1975 cells with radiation alone, we found increased ecto-CRT presentation and ATP secretion, but unaltered HMGB1 exodus. In samples co-treated with radiation and ATR inhibitors (VE822, AZD6738), ecto-CRT signalling at 24 and 72 hours and ATP secretion at 24 hours were decreased, whereas ATP secretion at 48h increased. Preliminary results from the HMGB1 assay showed increased HMGB1 exodus after co-treatment with radiation and ATR inhibition, compared to radiation treatment alone. We have also monitored type I interferon signalling in the aftermath of radiation by Western blotting of phosphorylated STAT1, as DNA from micronuclei will activate innate immune responses when present in the cytosol. We found increased STAT1 expression in the aftermath of radiation, in compliance with recent publications.

Table of contents

1 Introduction

1.1 General introduction

Cancer is, in humans, the common appellation of over 100 characterised genomic diseases [1]. The different cancer diseases arise from mutations in the genomic DNA, leading to uncontrolled cell proliferation and growth. Cancers have an accumulative nature, and several mutations – whether they are point mutations, insertions, deletions, inversions or fusions – are needed for the genomic alterations to become cancerous.

Over the last 50 years, global cancer incidence has increased. This may partially be due to better detection methods and higher worldwide quality of offered medical services, but trends in lifestyle development over the past decades (with obesity and intake of mutagens) is stated to be one of the main reasons for the increase. It is estimated that 30-50% of the global cancer incidence could be prevented through protection from risk factors [2]. Statistical analyses prefigure the increase to sustain, urging the need for more sophisticated strategies to therapeutically confront and eradicate the cancer diseases. In Norway, the total cancer incidence as of 2016 was 32 827 [3].

Tumours tend to show a high degree of heterogeneity, with genetically varied cells of the same tumour and tumour discrepancy between patients making conventional cancer therapy suboptimal. This has urged the recent exploration of personalised cancer medicine and cancer immunology. In cancer immunology, the ultimate goal is to recruit the patient's own immune system to the fight against cancer. As cancer diseases arise from the patient's own cells, it was thought that the immune system would not be capable of curing the illness. Over the past years, this view has changed, with immune checkpoint blockade and antibody therapy becoming increasingly explored.

One way of recruiting the immune system is to promote immunogenic cancer cell death. In this strategy, the immune system will respond to dying cell signalling, for thereby to recognise cancerous cells as dangerous. Both therapy with ionising radiation and some chemotherapies have shown to initiate immunogenic cell death, but unfortunately most often to a clinically insignificant degree. In this master's thesis it is explored whether the

degree of immunogenic cell death rises when combining ionising radiation with DNA damage checkpoint inhibition *in vitro*. Inducing immunogenic cell death by this strategy may contribute to optimise conventional local radiation therapy, and potentially generate an abscopal effect on distal metastases. In addition, it may provide increased sensitivity to subsequent immunotherapy.

1.2 Cellular responses to DNA damage

1.2.1 DNA damage in general

The DNA of cells is prone to damage from many sources, amongst these radiation, chemical compounds and reactive molecule species. With damage caused by both endogenous and exogenous factors, cells are typically exposed to up above ten thousands of DNA lesions on a daily basis (reviewed in [4, 5]). The damage can be of different natures, commonly alteration of single bases or nucleotides, single-stranded DNA-breaks (SSB) and double-stranded DNA-breaks (DSB). The latter is regarded the most harmful subgroup of DNA damage [6, 7]. If not repaired in time, such DNA damages may be lethal to the cells [6]. In addition, DNA damage may lead to mutations that could make the cells cancerous [4].

1.2.2 DNA lesions: Strand breaks and single base damage

There are two types of DNA strand breaks, namely single-stranded breaks and double-stranded breaks. The breaks occur in the phosphate sugar backbone of the helices, leading to partly (as in SSB) or complete (as in DSB) breakage of the DNA double-helix. The breakage of the DNA strands consists of reorganisation of the atomic bonds between or inside the ribose and the phosphate group of the backbone. Strand breaks can arise from different sources, amongst these ionising radiation and reactive molecule species (reviewed in [8, 9]).

Damage to the individual bases of the DNA can occur as reductions, oxidations and fragmentations. A subset of base modification products – such as O^6-methyle guanine, thymine glycols, thymine dimers, cyclobutane pyrimidine dimers and photoproducts – can arise, in which the first three modifications can result from ionising radiation and reactive oxygen species (reviewed in [9]). Base modifications as such may lead to replication stalling, strand breaks and mutations, and may therefore be lethal if not repaired.

1.2.3 The DNA damage response

Eukaryotic cells have developed several mechanisms to detect and repair DNA lesions, and molecular checkpoints will halt cells with DNA damage from proceeding through cell division (reviewed in [9-12]). These checkpoints supply the cells with sufficient time to repair the

damage. The repair mechanisms are collectively referred to as the DNA damage response (DDR), and consists of damage detection, damage signal transduction and initiation of responses to the damage (reviewed in [10]) (figure 1.1).

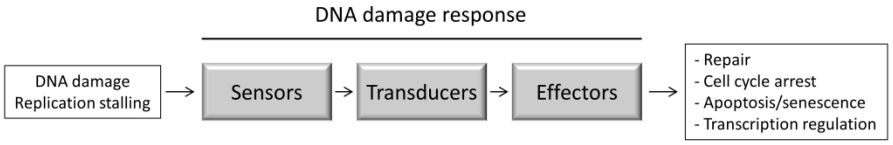

Figure 1.1. The DNA damage response (DDR) initiated by DNA damage or stalling of replication forks. The DDR consists of sensors, transducers and effectors. The sensors will detect the initiating factors, and activate transducers that convey the DDR signalling to downstream effectors. The effectors execute the actual response to the initiating factors (reviewed in [10]).

When cells encounter DNA damage, the initial effect of the DDR is to discover the damage and implement signalling cascades. Upon DSBs, two major signalling cascades are initiated through the ATR–CHK1 and the ATM–CHK2 pathways (reviewed in [13]).

The formed termini in a DSB will be recognised and bound by the protein kinase Ataxia telangiectasia mutated (ATM) and its regulator MRN, leading to ATM activation [14, 15] (figure 1.2a). MRN is a complex consisting of the three proteins Meiotic recombination 11 (MRE11), RAD50 and Nijmegen breakage syndrome 1 (NBS1) [16](reviewed in [9]). Normally, ATM is present as an inactive homodimer [17]. When activated by DSBs, ATM monomerises, and may phosphorylate several downstream effectors, including Checkpoint kinase 2 (CHK2) and p53, along with the DNA repair protein Breast cancer type 1 susceptibility protein (BRCA1) and the histone H2AX [16]. The latter phosphorylation gives rise to foci of phosphorylated γH2AX, a well-established marker for DNA damage.

Activation of the protein kinase ATM and RAD3 related (ATR) occurs through binding of ssDNA arising from processed (resected) DSBs (figure 1.2b). ATR binds to ssDNA *via* Replication protein A (RPA), often in complex with the regulator ATR-interacting protein (ATRIP) [14] (reviewed in [9]). From here, ATR phosphorylates its downstream effector Checkpoint kinase 1 (CHK1) by help of the mediators DNA topoisomerase-II-binding protein 1 (TopBP1), Claspin and Erwing's tumour-associated antigen 1 (ETAA1) [18-20]. ATR can also be activated in a similar manner by ssDNA occurring at stalled replication forks [14].

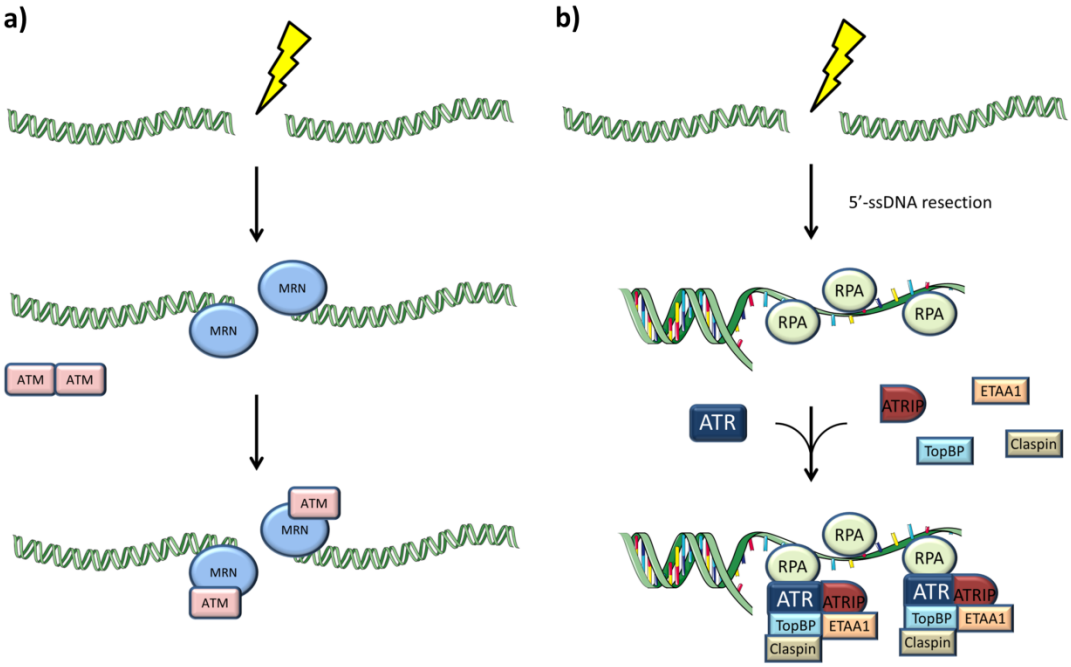

Figure 1.2. The figure is showing the initial activation of the DNA damage response following strand breakage. **a)** Upon double-stranded DNA breaks, the resulting ends of the break will be bound by the MRN complex. Subsequent binding of monomerised ATM to the MRN complexes activates the kinase activity of ATM. **b)** Double-stranded breaks may also result in 5'-ssDNA resection of the break ends. The resulting single-stranded DNA will be bound by RPA. From there, RPA recruits ATR along with ATRIP and the mediators TopBP1, Claspin and ETAA1 to form an ATR activating complex.

1.2.4 DNA damage-induced cell cycle checkpoints

Cells divide and replicate through a cyclic collection of events called the cell cycle. The cell cycle consists of four phases called gap phase 1 (G_1), synthesis phase (S), gap phase 2 (G_2) and mitosis/meiosis (M) (reviewed in [21]). The three first phases are collectively termed interphase (reviewed in [22]), and straight after the M phase, the cell undergoes cytokinesis to produce two (or four in meiosis) new G_1-cells. The cells can also circumvent the cell cycle by entering the growth-dormant phase G_0.

The progression through the cell cycle is governed by different complexes of proteins called cyclins and cyclin-dependent kinases (CDK) (figure 1.3a). Whereas the CDK level is constantly expressed in the cell, the levels of cyclins fluctuate in a cyclic fashion (figure 1.3b). By activating their respective CDK protein at their peaking concentration, cyclins propel the entry into subsequent phases (reviewed in [23]). The progression through the cell cycle is

determined by different intra- and extracellular factors and events. Signals can regulate the levels of CDK-inhibitors (CDI), which again regulate the different cyclin–CDK levels (reviewed in [23]).

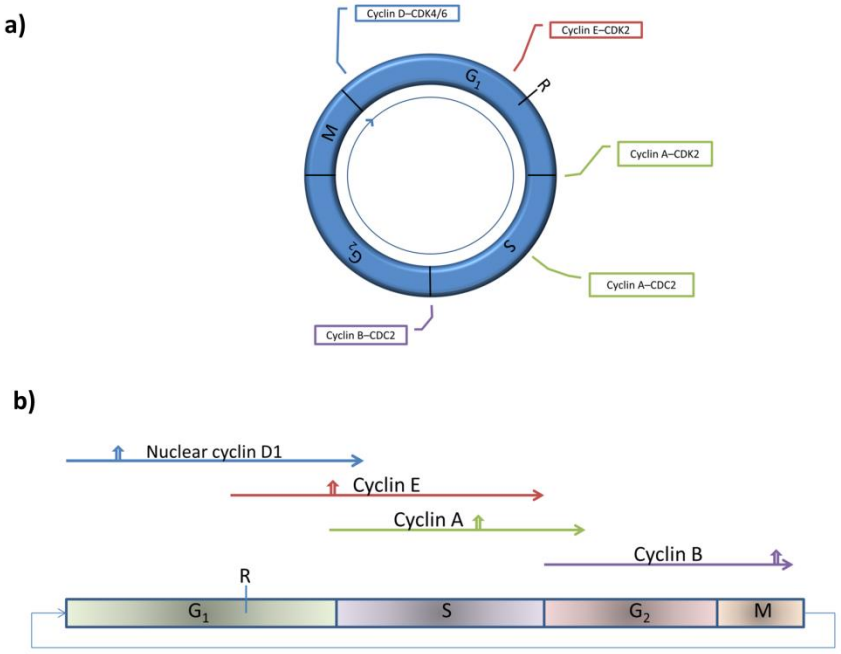

Figure 1.3. Figure showing the cyclin–CDK complexes driving the progression through the cell cycle. **a)** The cell cycle with the particular cyclin-CDK complexes involved in the different phases. **b)** The timing of the cyclic levels of the cyclins, with vertical arrows indicating the peaking concentration. (Technical information of the figures is described in [24]).

The proceeding through the cell cycle is strictly regulated by several molecular checkpoints, making sure that cells do not enter the subsequent phases before time. In each of the cell cycle phases, the cells prepare for division by phase-specific events, and rushing into the consecutive phase before finalising these events may result in DNA damage and lethality. Furthermore, it is crucial for the cells to prevent cell cycle progression following DNA damage, as this could lead to mutagenesis and/or cell death. The actions of cell cycle checkpoints prevent such occurrences. There are four checkpoints in the cell cycle, the G_1/S checkpoint (or restriction point) in G_1 phase, an intra-S phase checkpoint, the G_2/M checkpoint in G_2 phase (reviewed in [9]) and an M checkpoint in the mitotic metaphase (figure 1.4a).

The first cell cycle checkpoint a cell must transcend is the restriction point (R-point, also known as the G_1/S checkpoint). This checkpoint occurs about two-thirds into the timeline of

the G_1 phase, and is regulated by the tumour suppressor Retinoblastoma protein (pRB). The R-point is the 'point of no return' for further progress in the cell cycle, and thereby decisive of whether a cell shall divide or remain quiescent [25](reviewed in [21, 26]). From this point on, the cell will no longer be responsive to mitogens or other extracellular, growth-manipulating factors (reviewed in [27]). Active pRB inhibits a group of transcription factors called E2F, which are essential for the expression of proteins needed for G_1 to S phase transition [28]. CyclinD–CDK4/6, which is present in early G_1 phase, hypophosphorylates – and thereby activates – pRB. This makes pRB bind to and inhibit the E2F transcription factors [29]. As the cell cycle progress towards the R-point, and the level of cyclinE–CDK2 starts to rise, this complex will hyperphosphorylate – and thereby inactivate – pRB. With pRB inactivated, the E2F transcription factors can conduct their action, and the cell cycle will progress through the R-point.

The G_1/S checkpoint is also dependent on the tumour suppressor protein p53 [30] (figure 1.4b). p53 is an important mediator of cell cycle arrest, DNA repair and apoptosis as response to different cellular stresses. In a normal state, p53 is under control by the protein MDM2, which polyubiquitinates the protein and thereby initiates its 26S-proteasomal degradation. In turn, p53 is the transcription factor for *MDM2*. Upon DNA damage, p53 will be phosphorylated by CHK2, preventing the protein from ubiquitination, and thereby increasing its intracellular concentration (reviewed in [31]). The now active p53 will function as a transcription factor, and thereby conduct its effects. The initial action of p53 is to promote the expression of the CDI p21. p21 will then cause G_1/S arrest by inhibitory interactions with cyclin–CDK complexes. In addition, p21 prevents replication of the DNA by inhibitory interactions with the DNA clamp protein Proliferating cell nuclear antigen (PCNA) [32, 33]. Furthermore, CHK1 activation after DNA damage can result in G_1/S arrest by p53-independent signalling pathways. By phosphorylating the phosphatase Cell division cycle 25A (CDC25A), which is required for the G_1 to S transit, CHK1 promotes degradation of CDC25A and arrest at the G_1/S transition (and throughout S-phase, see below) [34](reviewed in [35]).

The next cell cycle checkpoint is the intra-S phase checkpoint. This is a p53 independent checkpoint that slows replication of DNA in response to DNA damage (especially DSB), for

instance by inhibiting replicon formation (reviewed in [36]). In this way, cells exposed to DNA damages after transit to the S phase will be slowed down, and the synthesis of DNA necessary for the cell to divide will be retarded. Mechanistically, the intra-S phase checkpoint is mainly implemented through reduced CDK activity, which is mediated by the ATR–CHK1 pathway and WEE1 (reviewed in [37]) (figure 1.4b)

The final DNA damage-induced checkpoint is the G_2/M checkpoint, located in the G_2 phase of the cell cycle. Cells with unrepaired DNA damage will be arrested in this checkpoint in order to give time for DNA repair before division. The G_2/M checkpoint is executed by ATM–CHK2, ATR–CHK1 and WEE1 in mostly p53-independent manners [38](reviewed in [37]) (figure 1.4b). Through inhibition of CDC25C by ATM and both CDC25C and CDC25A by CHK1, the cyclin B–CDK1 complex (necessary for entry into the M phase) will be indirectly inhibited, as this complex relies on the two cell division cycle proteins (reviewed in [37]). In addition to the CHK1/CHK2 mediated inhibition of CDC25A, it has been shown that Chk1 in fission yeast (*Schizosaccharomyces pombe*) may phosphorylate – and thus activate – the nuclear kinase Wee1 [39]. Activated WEE1 will phosphorylate CDK1, and thereby inactivate the cyclinB–CDK1 complex necessary for cell cycle advancement [40]. Other proteins are also involved in the G_2/M checkpoint; the tumour suppressor protein BRCA1 is important for the G_2/M checkpoint (arrest by activating CHK1), and the proteins BRCA2 and Partner and localiser of BRCA2 (PALB2) are necessary for the maintenance of it [41, 42]. Of note is that these proteins are frequently found to be mutated in several cancer diseases [43].

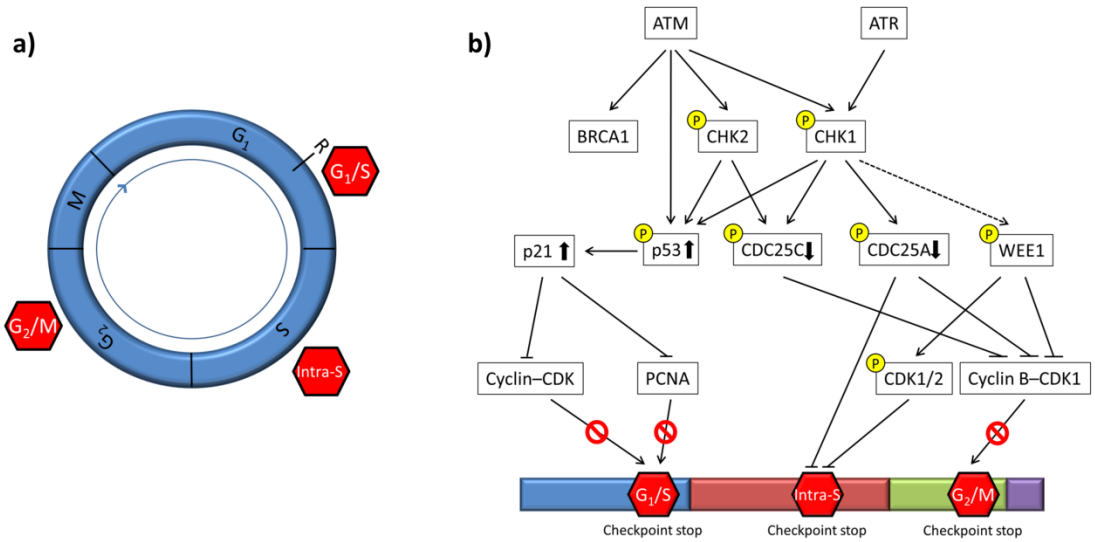

Figure 1.4. Activation of cell cycle checkpoints results in arrested cell cycle progression. **a)** The cell cycle with the DNA damage checkpoints in their respective phases. **b)** The downstream effects of the kinases ATM and ATR, and how their actions eventually lead to the inhibition of checkpoints. Pointed arrows indicate activating actions, whilst blunt arrows indicate inhibitory actions. Bold up- or down-arrow indicate up- and down-regulation, respectively. Stop signs indicate prevented actions, whereas yellow circles indicate phosphorylations.

1.2.5 DNA damage repair

The DDR has different repair pathways for different types of damage. Whereas bulky lesions and cross-binding in DNA is repaired by a process named nucleotide excision repair (NER), SSBs and individual base damages are processed by base excision repair (BER). In addition, DSBs will be repaired either by homologous recombination (HR) or different variants of non-homologous end-joining (NHEJ). Non-covalent damages will be detected and repaired by the mismatch repair pathways (MMR). As this thesis emphasises on ionising radiation-induced strand breaks, only repair pathways used in such encounters will be described in detail.

Individual SSBs are presented as nicks in one of the DNA strands in the double-helix, and is repaired by BER, or in this case called single-strand break repair (SSBR). BER is originally initiated by the removal of a damaged base by 8-oxoguanine DNA glycosylase (OGG1), producing an apurinic/apyrimidinic site (AP site) [44]. By the consecutive actions of a recruited AP endonuclease 1 (APE1), a nick is produced 3’ to the AP site, thereby forming a loose 5’-strand end [45]. In the case of SSBs, this is where the SSBR mechanism initiates. The nick will then recruit Poly-[ADP-ribose] polymerase-1 (PARP1) and PARP2, which will mediate the downstream pathway [46, 47](reviewed in [48]). From this point forward, the BER/SSBR pathway can take two paths, namely the short patch path or the long patch path. In the short patch path, a 5’-deoxyribose phosphate (dRP) lyase will then resect the loose 5’-strand, which is then replaced by the action of DNA polymerase β in complex with X-ray repair cross-complementing protein 1 (XRCC1) [49]. The newly synthesised strand will then be completely inserted by a complex of XRCC1 and DNA ligase-III [49]. In the long patch path, DNA polymerase β, δ and ε, in combination with Proliferating cell nuclear antigen (PCNA) and replication factor C (RF-C), starts complementary synthesis from the 3’ end of the nick, and continues the synthesis 2-6nt beyond the AP site [50]. Flap endonuclease 1 (FEN1), by help of PCNA [51], will then resect the now considerably longer 5’-strand end in a 5’->3’

fashion, before DNA ligase-I combine the newly synthesised replacement strand with the original strand [52].

Double-stranded breaks can be repaired by two separate mechanisms, namely homologous recombination (HR) and non-homologous end-joining (NHEJ). In HR, a homologous (identical) DNA sequence in a sister chromatid is used as a guiding template for the repair. Consequently, HR is an accurate repair mechanism, but is restrained to the S and G_2 phases of the cell cycle. In contrast, NHEJ may occur throughout the cell cycle, but is error-prone due to resection and direct fusion of DNA ends (reviewed in [10]).

In homologous recombination, the break repair is initiated by binding of a complex of C-terminal binding protein 1 interacting protein (CtIP) and the three proteins MRE11, RAD50 and NBS1 (collectively abbreviated the MRN complex) to each of the two double-stranded ends in the break (reviewed in [9])[53] (figure 1.5). The MRN complexes will then resect the ends in a 5'->3' fashion, yielding overhanging ('sticky') ends coated with RPA [54]. Once the ends have been processed, the protein RAD52 binds the resulting 3'-extension, removing the RPA [55, 56]. From here, RAD52 may bind the two respective single-strands together by a mechanism called single-stranded annealing [57], thereby finalising the repair, or continue with the HR mechanism. In the latter case, RAD51 proteins will attach to the single-strand upstream of the bound RAD52 [56]. By additional mediation from RAD51, BRCA1 and BRCA2, the RAD52-bound single-strand will perform a strand-invasion of a homologous molecule of DNA, producing a D-loop (reviewed in [9]). Non-homologous regions, if any, are thereafter cleaved off the invading 3'-extension (reviewed in [9]), before the extensions of the two ends will be prolonged by DNA polymerase δ and ε synthesis – according to the invaded template stands – in a process called branch migration [58-60]. This will produce either a Holliday junction or its equivalent four-stranded intermediate [61]. Eventually, a recruited MMS4•MUS81 heterodimer dissociates the junction [62], and DNA ligase-I re-ligates the strand-ends to form a repaired DNA strand [63], either with or without a cross-over of the strands.

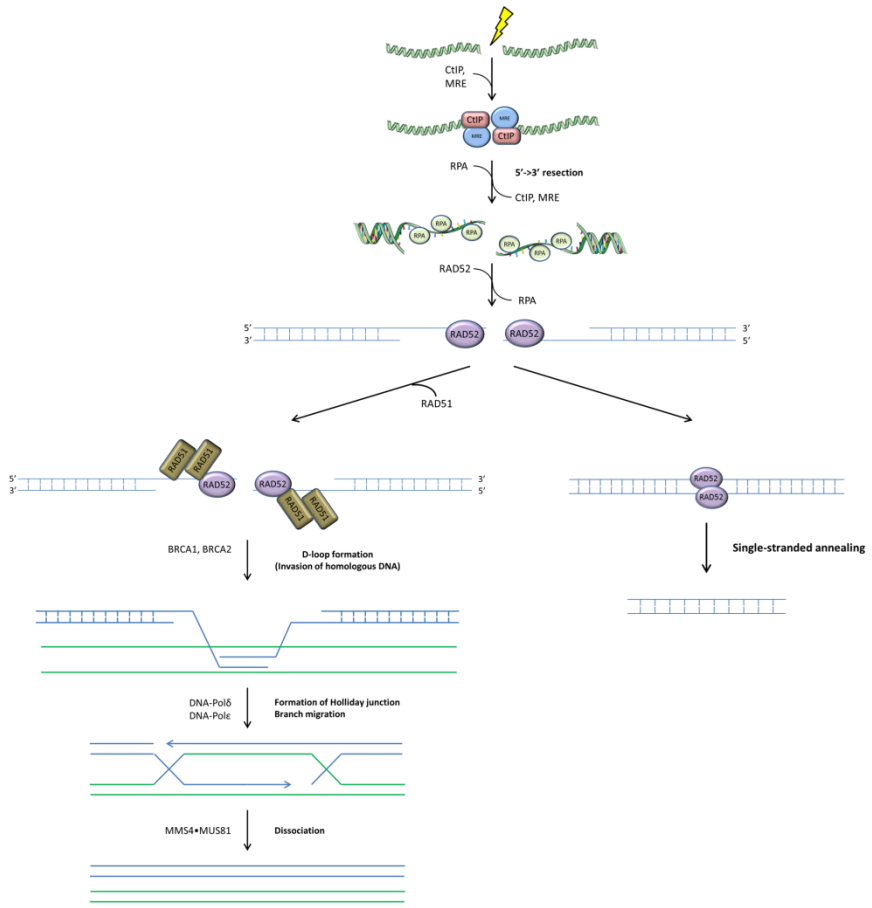

Figure 1.5. Homologous recombination in eukaryotic cells. Upon double-stranded breaks, the formed termini will be bound by C-terminal binding protein 1 interacting protein (CtIP) and the MRE11-RAD50-NBS1 (MRN) complex. Following MRE-mediated 5'->3' resection, Replication protein A (RPA) will bind the 3'-single-strands, before the protein are substituted by RAD52. RAD52 may anneal the two strands together directly, or recruit RAD51 to the strands. With RAD51 bound to the strands, the strands may invade a homologous DNA molecule (in green) and form a D-loop, mediated by Breast cancer type 1 susceptibility protein (BRCA1) and BRCA2. With resection of non-homologous regions, and synthesis/elongation performed by DNA polymerase (DNA-Pol) δ and ε with the homologous DNA as template, the two DNA molecules form a Holliday junction. Finally, the recruited heterodimer MMS4•MUS81 will disassociate the junction, producing a repaired DNA molecule.

When DSB is repaired by non-homologous end-joining, the initial step is the binding of a heterodimeric complex of the proteins KU70 and KU80 to each ends (reviewed in [64]) (figure 1.6). From there, the KU70/80 complexes recruit DNA-dependent protein kinases (DNA-PKs), MRN complexes and Artemis (reviewed in [64]). The following machinery will then process the two ends, before recruiting X-ray repair cross-complementing protein 4 (XRCC4), XRCC4-like factor (XLF/Cernunnos) and DNA ligase-IV [65-67]. Heterodimeric XRCC4•DNA ligase-IV then re-ligates the two ends, and the repair is completed [68].

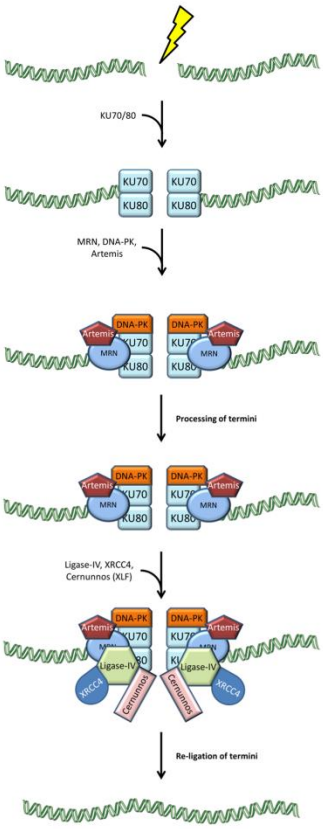

Figure 1.6. The process of non-homologous end-joining (NHEJ). After introduction of a double-stranded break in the DNA, a heterodimer of KU70 and KU80 is bound to the termini. From there, the KU70/80 complex recruits the MRE11-RAD50-NBS1 (MRN) complex, together with DNA-dependent protein kinase (DNA-PK) and the endonuclease Artemis. The resulting complex process the termini by removing damaged strand ends, before DNA ligase-IV (Ligase-IV), X-ray repair cross-complementing protein 4 (XRCC4) and XRCC4-like factor Cernunnos (XLF) is added to the repair machinery. The three latter proteins will then re-ligate the processed termini, and thereby repair the break.

In addition to the aforementioned conventional NHEJ (also called C- or D-NHEJ), there are also two other variants of the NHEJ mechanism, called alternative NHEJ or microhomology-mediated end-joining (Alt-NHEJ and MMEJ, respectively) and backup NHEJ (B-NHEJ). In short, the Alt-NHEJ mechanism makes use of the helicase Bloom (BLM), exonuclease 1 (EXO1) and FEN1 together with DNA ligase I, or DNA ligase-III in complex with XRRC1, for the break repair. On the other hand, the MRN complex bind the DSB ends together with PARP1 in B-NHEJ, and uses the helicase Werner (WRN) and DNA ligase-I for the repair of the break. These sub-mechanisms of NHEJ are reviewed in [69].

1.3 Ionising radiation

1.3.1 Ionising radiation in general

Ionising radiation (IR) is radiation that has the potential to transfer energy to, and thereby ionise, molecules. On that basis, ionising radiation includes α-, β-, γ-, neutron and X-ray radiation [70]. If this energy transfer is below an electron's effective ionisation potential, electrons in the irradiated molecules will be moved to a higher-energy orbital, and the molecules will be excited. If, on the other hand, the transfer is of higher energy than the effective ionisation potential, this will lead to a positively ionised molecule. In other words, such an ionised molecule is a molecule that has ejected a negative charge (electron), and hence has a redundancy of positive charge. Positive ionisations start chains of reactions, as the ejected electrons carry with them energy that may ionise or excite secondary molecules, and so on, until the energy has been sufficiently reduced to no longer being able to ionise (reviewed in [8]).

In biological samples, ionising radiation affects cellular components in both a direct and an indirect way. The direct interaction between the radiation and macromolecules may lead to substantial damage, *e.g.* strand breaks and single-nucleotide damage in the DNA, with its extent reflecting the number of electrons in the sample. The energy transferred from the radiation will affect the phosphate bonds in the DNA backbone, leading to breakage. Despite this direct effect, the main effect of irradiation will be the formation of reactive molecule species (or radicals), especially reactive oxygen species (ROS). The radicals will interfere with bonds in the DNA, eventually leading to breakage (reviewed in [8, 9]).

Whether from the direct or indirect effect of ionising radiation, SSB will occur at random localisations throughout irradiated DNA. At these sites, activated electrons will produce clustered damage. These clusters arise as the electrons eventually leave behind grouped effects in the end of their reaction course, in compliance with the loss of energy transferred. The clustered damage will unveil as DSBs (reviewed in [8]).

The dose of ionising radiation can be depicted as equivalent (*H*) and absorbed dose (*D*) [71]. Absorbed dose is the amount of energy that a matter absorbs during ionising irradiation, and

when referring to the absorbed dose of ionising radiation to a specimen, the unit gray (Gy) is used [72]. A dose of 1Gy will correspond to 1 joule absorbed energy per kilogram specimen.

$$1Gy = 1\ J\ kg^{-1}$$

Equation 1. The equation describes the radiation unit gray (Gy) in terms of absorbed energy (joule, J) per weight of irradiated matter (kilogram, kg).

1.3.2 X-rays

X-rays are ionising electromagnetic radiation with wavelength commonly regarded between 0.01-10nm. X-rays may occur as characteristic radiation formed by excited atoms, or as deceleration radiation (*bremsstrahlung*) from electrons. The common way of producing X-rays is by use of an X-ray tube, which produces *bremsstrahlung* with a continuous spectre. In modern X-ray tubes, electrons are ejected with high velocity from a heated hot cathode, directed against an anode containing a heavy metal target, *e.g.* tungsten (wolfram). As the electrons hit the heavy metal target, they are heavily decelerated/scattered, and their kinetic energy is converted into high-energy photons. These photons then constitute the X-ray radiation [73].

1.3.3 Reactive molecule species

The cell can be prone to damage from several types of reactive radical molecules, including reactive oxygen species (ROS) and reactive nitrogen species (RNS). These reactive molecules, or free radicals, are characterised by having at least one unpaired (and therefore reactive) electron [74]. The main, and most damaging, ROS originating from primary ionising radiation events is the hydroxyl radical ($HO^{\bullet}$) (reviewed in [74, 75]). With up to 2000 primary ionisation events per Gy per cell, and with $HO^{\bullet}$ being able to diffuse a length of about 4nm before reacting, DNA damage arising from hydroxyl radicals constitute a considerable part of the IR-induced cellular damage (reviewed in [8, 11, 75]). It has been estimated that only one-third of X-ray-induced DNA damage is due to the direct means of the radiation, whereas the remaining two-thirds is held responsible by ROS.

Radicals will lead to DNA damage by pairing their unpaired electrons through formation of chemical bonds. As most cellular compounds have their valence electrons paired in bonds,

this means that the paring of radical electrons most often leads to breakage of already existing chemical bonds. When interfering with DNA, $HO^{\bullet}$ will attack sugar moieties in 22% of the cases, whereas nucleotide bases are subject to attack in 78% of the cases. $HO^{\bullet}$ may cause excitation of the hydrogen atoms bound to the 4'-C or 5'-C of pentoses in the DNA, which – in oxygenated environments – leads to strand breakage (reviewed in [8]).

1.3.4 Cell death following ionising radiation

When applied to cells, 1Gy of ionising radiation is estimated to yield about 10^5 ionisation events, over 1000 single base damages, around 1000 SSBs and 20-40 DSBs in the DNA of each cell [76]. Most of these damages are effectively repaired by the cells, and only about 30 per cent of irradiated populations of human/mammalian cells will succumb to this radiation dose [76]. Cells exposed to IR may die by several distinct death mechanisms – including apoptosis, autophagic death, necrosis and mitotic death – or enter the state of senescence [76](reviewed in [77]). Several of the death mechanisms can be initiated simultaneously, but in cancer cells – in which *TP53* is often found mutated – the apoptotic pathway following DNA damage may be discontinuous, rendering the apoptotic response defect [76].

Cell death following IR may be grouped into three classes, namely pre-mitotic death (or interphase death), post-mitotic death and 'bystander' death. With pre-mitotic death being uncommon in solid tumours, most IR-associated cell death is regarded post-mitotic, and occurs after one or repeated attempts of mitosis. Hence, population-wise death will mostly occur in the timespan of at least one cell division after the irradiation event. The 'bystander' death is an interesting, yet far from understood, death mode in untreated cells neighbouring irradiated ones. It is thought that this death is initiated by secretion of signal molecules from the irradiated cell to the surrounding cells either *via* the extracellular space or through gap junctions [76].

Mitotic death – the death mechanism following mitotic catastrophe – is regarded the primary death mechanism following IR. Unrepaired damage to the DNA of cells generally leads to distorted chromosomes, often with dicentric or acentric fragments. As cells lacking normal centromeres attempt cell division, the chromosomes will be faulty separated, thereby giving rise to micronuclei [76]. With the cell division leaving the progeny genomically

incomplete, with randomly distributed fragments of the chromosomes, the resulting daughter cells are in grave danger of losing essential gene products necessary for their survival. Hence, mitotic catastrophe eventually leads to cell death, which can occur at various times after cell division [78].

1.4 Radiation therapy and inhibitors of the ATR pathway

1.4.1 Radiotherapy

Besides surgery, radiation therapy is one of the most established cancer therapies. Over 50% of diagnosed solid tumours will be subjected to local X-ray based radiotherapy [79](reviewed in [7]). The ultimate goal of the radiotherapy is to promote cell death amongst the tumour cells, and at the same time minimise side effects in surrounding normal tissue. Strictly localised radiotherapy is crucial for the outcome, as the often-used X-ray radiation itself is mutagenic, and may lead to secondary cancers through DNA damage (reviewed in [7]). In addition, other late effects in normal tissue (*e.g.* fibrosis) are of major concern in radiotherapy [80].

Today, radiotherapy is most commonly applied as fractionated therapy. To alleviate normal-tissue toxicity, daily fractions of 1.8-2Gy are commonly applied to a total radiation dose of 40-70Gy [81](reviewed in [82]). Fractionated therapy is based upon the so-called 'four Rs of radiobiology'; repair (of sublethal DNA damages), reoxygenation (of hypoxic tumours/areas), redistribution (of cells in the cell cycle) and repopulation [81](reviewed in [82]). Fractionation of the total radiation dose gives time for these events to occur between the irradiations, and is considered the most efficient utilisation of the radiation dose in order to achieve killing of tumour cells and at the same time spare surrounding normal tissue.

Despite its widely usage, radiotherapy is often not curative on its own, neither locally nor systemically [79]. Therefore, radiotherapy is typically used in combination with other treatment modalities, such as surgery and chemotherapy. Recently, combined treatment of radiotherapy and immunotherapy has become very attractive, and several clinical trials testing this co-treatment are now ongoing (*ClinicalTrials.gov*).

1.4.2 ATR inhibition and cancer treatment

By inhibiting ATR, ATR-dependent cell cycle checkpoints (especially the G_2/M checkpoint) will be abrogated (figure 1.7a). In essence, what follows is that the cell will enter mitosis without repairing damaged DNA, which will eventually lead to mitotic catastrophe and cell death as described in section 1.3.4 (reviewed in [83]).

The use of combined radio- and chemotherapy as performed at present time often results in high toxicity in healthy tissues [84]. An important reasoning for using ATR inhibitors in combination with radiation, is to make the effects of radiation more cancer specific: As healthy cells have the p53-dependent G_1/S cell cycle checkpoint intact, the use of ATR inhibitors is more targeted towards the often p53 mutated cancer cells [85]. Tumour cells lacking the G_1/S checkpoint may depend more on the G_2/M checkpoint for the repair of DNA. Hence, ATR inhibitors (which can be employed in low and non-toxic concentrations) can potentially cause mitotic death in tumour cells, whilst normal cells with wild-type p53 and a functional G_1/S checkpoint are spared [84] (figure 1.7b).

In addition to direct inhibition of ATR, inhibition of the downstream kinase CHK1 will implement the same resulting G_2/M checkpoint abrogation. Furthermore, inhibition of WEE1 will also cause G_2/M checkpoint abrogation. Thus, the G_2/M checkpoint can be abrogated by inhibitors of either ATR, CHK1 or WEE1 (figure 1.7a). The WEE1 inhibitor MK1775 is presently in clinical trials combined with radiation (*ClinicalTrials.gov*). The CHK1 inhibitor AZD7762 (which have been used in this project) has been terminated from clinical trials due to unpredicted toxicity [86], but other CHK1 inhibitors remain in clinical trials (*ClinicalTrials.gov*). Of note is that ATR, CHK1 and WEE1 inhibitors also lead to abrogation of the intra-S phase checkpoint, and that they can cause additional DNA damage in S phase through initiation of unscheduled replication [87].

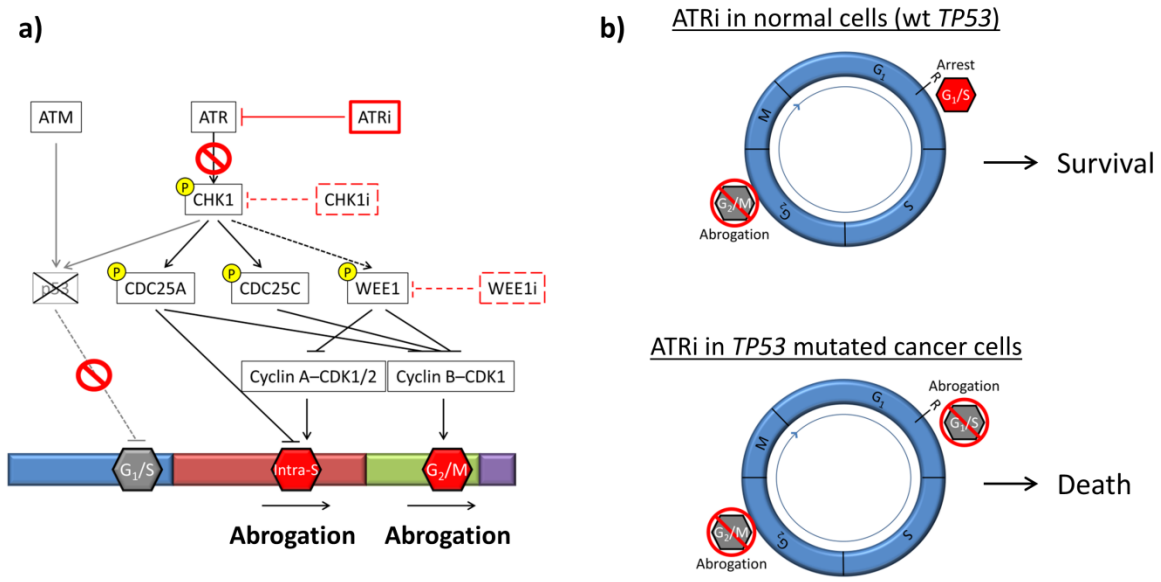

Figure 1.7. The effect of ATR inhibition on cell cycle checkpoints. **a)** The network shows the rationale behind inhibition of ATR, CHK1 and WEE1 in *TP53* mutated cancer cells, resulting in the abrogation of all the DNA damage cell cycle checkpoints. Inhibitors of the aforementioned proteins are indicated as ATRi, CHK1i and WEE1i, respectively. Pointed arrows indicate activating actions, whilst blunt arrows indicate inhibitory actions. Bold up- or down-arrow indicate up- and down-regulation, respectively. Stop signs indicate prevented actions, whereas yellow circles indicate phosphorylations. **b)** The figures show how ATR inhibition of cells with mutated *TP53* disables both checkpoint pathways for DNA repair and thus leads to death, whereas cells with wild-type (wt) *TP53* still have a functional G_1/S checkpoint, and therefore survive.

1.4.3 ATR inhibitors VE822 and AZD6738

The two ATR inhibitors VE822 and AZD6738 are now in clinical trials together with radiotherapy (*ClinicalTrials.gov*). VE822 (also referred to as VX970) is an ATR inhibitor developed and ameliorated from its precursor VE821. VE821 was shown to chemo- and radiosensitise cells, depicting the potential of ATR inhibition [85, 88]. The improved VE822 is highly selective towards ATR, with selectivity over hundred-fold higher to ATR than to the close molecular Phosphatidylinositol-3 kinase-related kinase (PIKK)-family relatives ATM and DNA-PK [84]. VE822 inhibits the phosphorylation of CHK1 by ATR, and thus restrain the checkpoint function of the ATR–CHK1 pathway. VE822 has a molecular weight of 463.55, and a half maximal inhibitory concentration (IC_{50}) of 19nM in HT29 colorectal adenocarcinoma cells [89].

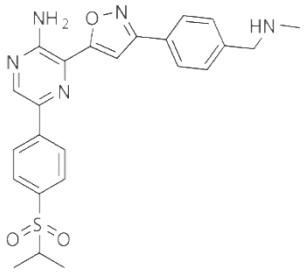

Figure 1.8. Condensed structural formula of the ATR inhibitor VE822. Figure adopted from [89].

AZD6738 is an orally active ATR inhibitor of 412.51 g/mol, with an IC_{50} of 1nM [90].

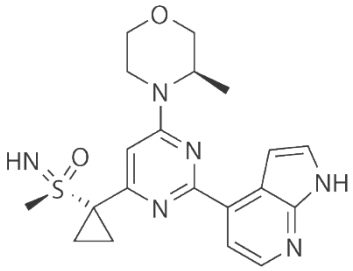

Figure 1.9. Condensed structural formula of the ATR inhibitor AZD6738. Figure adopted from [90].

1.5 Cancer and immunology

Many organisms, both complex and simple, have through evolution adapted defence systems to protect themselves against disease-causing elements. These are referred to as immune systems. In vertebrates at systematically higher levels than jawless fishes, the immune system is subdivided into two separate parts, namely the innate and the adaptive immune system [91]. Whereas the innate immune system is consecutively active, handling most harms and infections within a couple of days, the adaptive immune system is more slow, using about a week to produce specific responses to the stimuli and establish an infection memory [92].

Cancers change their local environment, and this is initially considered harmful by the immune system [93]. An essential property of the immune system is to differentiate between cells and compounds of the animal (termed self-cells and self-compounds) and the cells or compounds of the infectious element (reviewed in [94]) – and also altered-self [95, 96] – in order to react on foreign harms and avoid autoimmunity [97]. In cancer diseases, the cancerous cells are of self-origin, and it is therefore difficult to produce an effective

eradicating immune response towards the cancer (reviewed in [98]), although established immune responses can be lethal to single tumour cells. In this way, cancers usually avoid detrimental immune responses (reviewed in [98]). However, much research in now focused on finding ways to make the immune system able to fully react to and attack tumours.

1.5.1 Basic innate immunology

The innate immune system is the first line of defence against infections in the body. Circulating through the whole body, the innate immune system reacts more or less un-specifically to a wide spectre of foreign and tentatively futile elements. Consisting of different effector cells (including phagocytic macrophages and dendritic cells, granulocytes and natural killer (NK) cells) (reviewed in [99]) and different pathways of activating serum proteins called the complement (reviewed in [100]), the innate immune response disarms most infections, pathogens and non-functional cells within some days without causing illness.

To prevent autoimmunity, it is vital that the innate immune system does not react upon normal cells of the body. Together with the complement's C3b protein subunit binding to pathogens as a non-self label [101], the innate immune system seeks specific pathogen-associated molecular patterns (PAMPs) (reviewed in [102]). The surface of the phagocytic effector cells has several pattern recognition receptors (PRR) for the detection of non-self elements, including lectins, scavenger receptors and Toll-like receptors (TLR) (reviewed in [103-105]). The TLRs are distributed both on the extracellular and the cytosolic side of the plasma membrane, and additional intracellular reaction pathways contribute to intracellular detection of PAMPs. Amongst these pathways is the cGAS–STING pathway for detection of the PAMP cytosolic dsDNA [106, 107].

1.5.2 Basic adaptive immunology

If an infection over-runs the actions of the innate immune system, an adaptive immune response is needed. To establish an adaptive immune response, antigens should be phagocytised by myeloid dendritic cells or other antigen-presenting cells (APC), carrying the antigens to secondary lymphoid tissues. Often, the APCs will carry the antigens to the

nearest draining lymph node, where they are dispatched in an area called the lymphoid follicle (also known as the B-cell area). Here, immature B-cells will bind to the pathogen antigens and aggregate to form germ centres for their activation into effector B-cells (plasma cells) and memory B-cells (reviewed in [108]). In addition, the APCs will move into the T-cell area of the lymphoid tissue, where they activate immature T-cells (reviewed in [109]). Activated $CD4^+$ helper T-cells (T_H) will from there move into the follicle, where the T-cells help maturate the B-cells into plasma cells [110]. The rest of the activated effector T-cells (including $CD8^+$ cytotoxic T-cells and $CD4^+$ T-cells) will then move out of the lymphoid tissue, heading towards the site of infection. Here, they will attack their targets by release of cytotoxic compounds (only $CD8^+$ cells) or cytokines for changing target cell behaviour or recruitment of other immune cells. In this way, the adaptive immune system produces antigen-specific responses to disease-causing factors in the body (reviewed in [111]).

1.5.3 Immune checkpoints as targets for cancer treatment

Despite the fact that one of the hallmarks of cancer is the avoidance of immune destruction (reviewed in [112]), cancerous tumours are not totally neglected by the immune system. Although of self-origin, cancer cells produces foreign-signals (or rather dangerous self-signals) called tumour-associated antigens (TAA) that are detected by the immune system. Upon encounter, the TAAs will be taken up by APCs and presented on Major histocompability complex (MHC) class II for activation of $CD4^+$ T_H, or cross-presented on MHC class I for direct activation of $CD8^+$ cytotoxic T-cells (reviewed in [79]). Part of the reason why these TAA-producing cells don't end up being eradicated by the immune system, is that adaptive immune responses are under negative control of the receptors Cytotoxic T-lymphocyte-associated antigen 4 (CTLA-4) and Programmed cell death receptor 1 (PD-1) [113, 114].

PD-1 is present on T-cells, and the suppression of T-cells through this receptor is called the immune checkpoint. All self-cells in the body will present its ligand, called Programmed cell death receptor 1 ligand (PD-L1), and by binding to this ligand, intracellular inhibitory signalling will be conveyed inside the T-cells, leading to T-cell tolerance (reviewed [115]). It has been shown that many cancers upregulate PD-L1 (reviewed in [116]). During the last

years, inhibition of this immune checkpoint has been explored as a way to make adaptive immune responses to cancer cells, having some effect on several cancer diseases, including some melanomas, carcinomas and lymphomas [117]. PD-1 and PDL-1 inhibitors are now approved for cancer treatment [117].

CTLA-4 is another receptor present on the surface of T-cells. CTLA-4 binds B7 on APCs, the same molecule that is bound by CD28 on T-cells as co-stimulatory signal. In this way, CTLA-4 and CD28 competes for binding the same ligand. Whereas CD28-binding results in T-cell activation, binding by the antagonistic CTLA-4 disables T-cell activation, and thereby prevents a T-cell response (reviewed in [115]). CTLA-4 inhibitors are currently tested in pre-clinical and clinical studies for cancer treatment (*ClinicalTrials.gov*).

1.6 Immunogenic cell death

Another reason for why the immune system does not naturally respond to cancers is the lack of adjuvancy. In order to prime a T-cell response towards TAAs, the APCs are in need of an adjuvant (*i.e.* a danger signal), which often is absent from tumours. In addition, some cancer-secreted adjuvants promote tumour inflammation rather than priming of adaptive immune responses (reviewed in [118]). Immunogenic cell death (ICD) is a cell death modality that modulates systemic immune responses. ICD can be executed both by immunogenic necrosis and by immunogenic apoptosis [119](reviewed in [120]). By secreting specific immune activating signals called damage-associated molecular patterns (DAMPs, occasionally also referred to as danger-associated molecular patterns), the dying cells signal their presence as 'dangerous' to the immune system constituents (reviewed in [121]). Cancer cells have been shown to die in ICD manners following radio- and chemotherapy [122, 123]. APCs will be activated by secreted DAMPs, and thereby also pay more attention towards the otherwise neglected TAAs. This will lead to T-cell priming against the cancer-specific TAAs and neoantigens, producing a systemic anti-tumour immune response. In this way, the DAMPs of ICD function as adjuvants for TAAs in an *in situ* vaccination-like mechanism (reviewed in [121]) (figure 1.10).

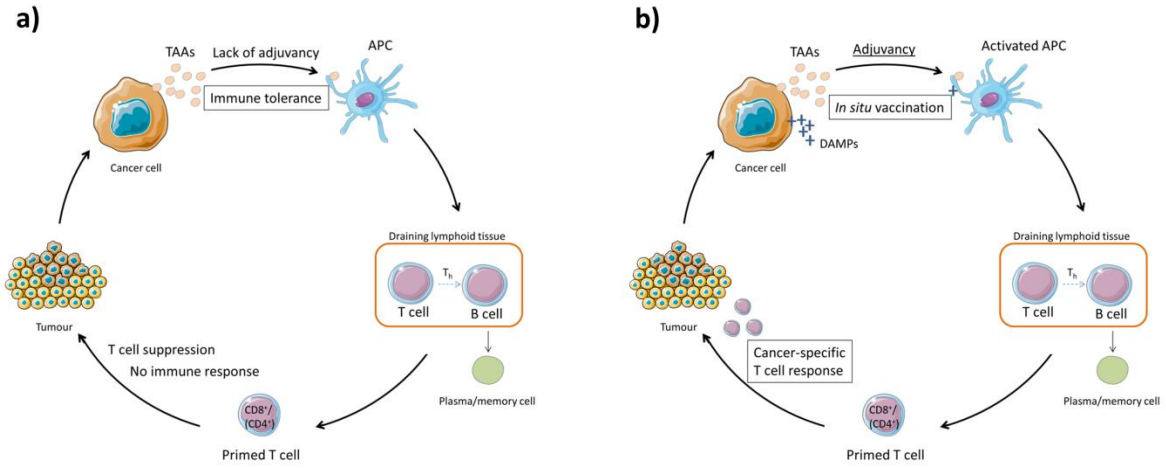

Figure 1.10. Figure showing the altered immune response following immunogenic cell death. **a)** The figure shows how cancer cells avoid detrimental immune responses through immune tolerance and T-cell suppression, despite their presentation of secreted tumour-associated antigens (TAA) to professional antigen-presenting cells (APC). **b)** The figure shows how the additional secretion of danger-associated molecular patterns (DAMPs) as adjuvants from dying cancer cells leads to an *in situ* vaccination, yielding a complete adaptive immune response with T-cell attack on the tumour cells.

Radiation therapy has been shown to induce immunogenic cancer cell death, but almost exclusively at a clinically insignificant level [124](reviewed in [125]). However, rare cases of abscopal effects have been reported, a term first coined by R. H. Mole in the early 1950s [126, 127]. In the abscopal effect, irradiation of local tumours primes an adaptive immune response and leads to suppressive effect on distal tumours and metastases. Originally described merely as an observed IR treatment effect, it was only decades later that the underlying mechanism of the abscopal effect was shown to be immunogenic cell death [127].

ICD is characterised by presentation of a subset of DAMPs. It is the oxidative stress following IR or chemotherapy that is thought to initiate DAMP presentation [128](reviewed in [121]). The best established ICD-associated DAMPs are the surface presentation of calreticulin (ecto-CRT), secretion of adenosine 5'-triphosphate (ATP) and exodus of High-mobility group box 1 (HMGB1) from the nucleus to the cytosol and the extracellular environment (reviewed in [129]). These three hallmarks have been shown to be crucial for induction of effective ICD (reviewed in [129]). In addition to these, surface presentation of Heat-shock protein 70 (HSP70) and HSP90, down-regulation of CD47 and secretion of different cytokines (*e.g.*

tumour necrosis factor α (TNF-α) and interleukin 1β (IL-1β)) are some of the lesser-established DAMPs (reviewed in [11, 121, 130].

1.6.1 Calreticulin

Calreticulin (CRT) is a 46kDa Ca^{2+}-binding lumenal endoplasmic reticulum (ER) chaperone protein involved in folding and organisation of proteins under their synthesis, cellular Ca^{2+} homeostasis and loading of peptides onto MHC class I (reviewed in [131])[132]. In response to ER-stress, CRT is actively and pre-apoptotically translocated from the ER lumen to the extracellular plasma membrane surface [130, 133].

Different mechanisms have been proposed for translocation of CRT to the cell surface. In one model, Protein kinase RNA-like ER kinase (PERK) is activated after induced ER-stress, thereby phosphorylating Eukaryotic translation initiation factor 2A (eIF2a). This activates reaction pathways initiating apoptosis, in which caspase-8 is partly activated. Caspase-8 then mediates cleavage of the ER chaperone B-cell receptor-associated protein 31 (BAP31). Together with conformational activation of the apoptosis regulators Bcl-2-associated X protein (BAX) and Blc-2 homologous antagonist/killer (BAK), CRT will be exocytosed in a Soluble NSF attachment protein receptor (SNARE)-dependent manner *via* the Golgi apparatus to the cell surface, in complex with the ER chaperone ERp57 [133]. Another model suggests CRT to be translocated by classical PI3K-dependent secretion to the cell surface, independent of apoptotic induction [130].

The translocated CRT will attach to the cell surface through the lipid raft anchoring protein CD57 [134], and functions as ‘eat me’ signals for phagocytes. This occurs through binding and activation of the receptor LDL-receptor-related protein (LRP1)/CD91 on the phagocytes [135]. Cells may generally present some calreticulin on their surfaces, but this is non-immunogenic [134, 136]. The vast translocation following ICD is on the other hand very immunogenic, and effectively contributes to the primed immune response [137].

1.6.2 High-mobility group box 1

High-mobility group box 1 (also referred to as amphoterin) is a non-histone chromatin binding nuclear protein of 25/30kDa [138, 139]. HMGB1 interacts directly with the minor

groove of the DNA double-helix without sequence specificity, and is thought to bend the molecule for facilitation of transcription and V(D)J recombination [140-142]. Histones disregarded, HMGB1 is one of the most abundant nuclear proteins, and interacts with a plethora of other transcription-regulating proteins [143]. When present in the cytosol, HMGB1 promotes and sustains autophagy by binding to beclin-1 [144].

HMGB1 proteins can diffuse out of the nucleus through the nuclear pore complexes [145]. Passively extracellular HMGB1 release, on the other hand, is dependent on permeabilisation of the plasma membrane, and thus restricted to necrosis and necroptosis as a *post mortem* event. In addition, HMGB1 may actively be secreted from cells in late immunogenic apoptosis [146]. As HMGB1 is shifted out of the cell, it will be bound by TLR2, TLR4 and Receptor for advanced glycation endproducts (RAGE, also known as AGER) on dendritic cells and macrophages [147-149]. Thus, release of HMGB1 initiates pro-inflammatory cascades, leading to phagocytosis of its originating cell and recruitment of immune cells.

In addition to being released as a DAMP, HMGB1 may also be secreted in a non-ICD – although immunogenic – state, acting as cytokine from IL-1β, TNFα or lipopolysaccharide (LPS) activated macrophages and monocytes [150, 151]. This is an active secretion, mediated by lysosomal exocytosis [145].

1.6.3 Adenosine 5'-triphosphate

Adenosine 5'-triphosphate is the main cellular energy source, involved in a vast number of molecular mechanisms. ATP is a small molecule of 507.18 g/mol, consisting of an adenosine bound to a triplet of phosphate groups. It is the energy-rich phosphate bonds that, upon hydrolysis, exert energy for propelling cellular reactions.

ATP – generally restricted to the intracellular space – can be secreted out of the cell through autophagy [152]. When present outside the cell membrane, the molecule acts as a DAMP [153]. ATP is shown to be pre-apoptotically secreted by an autophagy-mediated lysosomal exocytosis pathway, in which lumenal ATP in lysosomes and autophagosomes is transported out of the cell in a Lysosomal-associated membrane glycoprotein-1 (LAMP1)-, Vesicle-associated membrane protein-1 (VAMP1)- and vesicular nucleotide transporter (VNUT)-dependent manner. Moreover, it was shown that apoptotic blebbing of the plasma

membrane was necessary for the secretion. Actual ATP release over the plasma membrane occurs by transport through Pannexin-1 channels. As the regulatory C-terminal tail of Pannexin-1 is cleaved by caspase-3, the protein remains in an active state, enabling the ATP release. In this way, cytosolic ATP may be released in an autophagy-independent manner, although the translocation of Pannexin-1 to the plasma membrane was shown to rely on the autophagy-associated protein ATG5 [154].

Released ATP will be bound by macrophages and dendritic cells via their purinergic receptors P_2X_7 and P_2Y_2, thereby functioning as a 'find me' signal for phagocytosis [153, 155]. This will convey proinflammatory signalling cascades in the macrophage or dendritic cell, leading to assembly of inflammasome and phagocytosis of the ATP secreting cell [153, 156].

1.6.4 Cytoplasmic dsDNA

The presence of double-stranded DNA in the cytosol is associated with bacterial or viral infection, thereby acting as a PAMP [157](reviewed in [158]). Hence, cells with cytosolic dsDNA are prone to signal their presence as dangerous to cell of the innate immune system, thereby initiating their own perdition. Although cytoplasmic dsDNA is not included in the conventional definition of ICD, this PAMP will mediate death through induction of an immune response. It is the cytosolic protein cyclic GMP/AMP synthase (cGAS) that detects cytosolic dsDNA [107]. Upon binding of dsDNA, cGAS produces cyclic dinucleotide GMP/AMP (cGAMP), which in turn functions as second messenger for the activation of Stimulator of interferon genes (STING) (figure 1.11). Activated STING induces transcription of interferon genes through activation of nuclear factor-κB (NFκB) and Interferon regulatory factor-3 (IRF3) *via* IκB kinase (IKK) and TANK-binding kinase-1 (TBK1) [106].This leads to the production of type I-interferons, *e.g.* IFN-1β, which – when secreted – act both autocrine and paracrine for induction of inflammation responses [159].

Secreted type I interferons bind dimerised receptors in the plasma membrane. The receptors will upon this binding activate associated Janus-like activating kinases (JAK), which in turn phosphorylates the receptor. The phosphorylation of the receptor enables the binding of Signal transducer and activator of transcription-1 (STAT1) molecules, additional JAK-phosphorylation subjects. After being phosphorylated, the STAT1 molecules dimerise and,

following entry into the nucleus, function as a transcription factor for the IFN genes (reviewed in [160]). By this, the IFN signalling is amplified by a positive feedback loop.

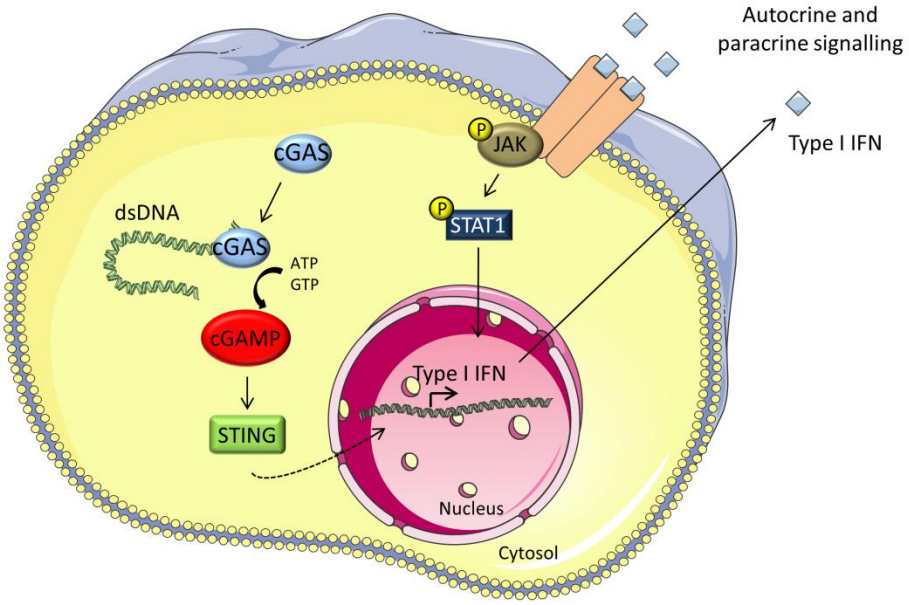

Figure 1.11. Figure showing the detection of cytosolic dsDNA by cGAS, of which downstream signalling pathway leads to transcription of type I interferons (IFN). The IFN is secreted out of the cell, where it can appear as both an autocrine and a paracrine signalling molecule. Upon binding to dimerised surface receptors, JAK is activated. JAK will activate STAT1 by phosphorylation (pSTAT1), and dimerised pSTAT1 will enter the nucleus and induce transcription of type I IFN in a positive feedback loop fashion.

Micronuclei arise as cells with damaged DNA undergo mitosis. The DNA fragments in the micronuclei are prone to be degraded in a mechanism called chromothripsis, which also leads to damages in the nuclear envelope of the micronuclei [161]. Thus, the micronuclear lumen and the cytosol is a continuous milieu, and the dsDNA of the micronuclei may therefore be detected as PAMP DNA [162, 163].

2 Aim

In this Master project, the aim is to evaluate the potential of cell cycle checkpoint kinase inhibitors as inducers of immunogenic cell death when combined with ionising radiation. The overall goal is to address whether inhibitors of the G_2/M checkpoint (more specifically inhibitors for ATR, CHK1 and WEE1 (see Figure 1.4), with emphasis on ATR inhibitors) may affect the presentation of the three hallmark factors of immunogenic cell death, when applied in combination with ionising radiation.

The hypothesis of the project is that cell cycle checkpoint kinase inhibitors may enhance the degree of immunogenic cell death when given as co-treatment with ionising radiation, as this will lead to more mitotic catastrophe and a synchronised wave of death. Radiotherapy has previously been shown to induce ICD signalling, although at therapeutically insignificant levels. By abrogating the G_2/M cell cycle checkpoint, higher numbers of the cancer cells will undergo mitotic catastrophe, which in turn may increase the ICD signalling and thereby produce an increased systemic immune response (figure 2.1).

The project has three specific aims:

I. To optimise methods for detection of three established hallmark factors of immunogenic cell death: Surface presentation of calreticulin, extracellular release of ATP and exodus of HMGB1.
II. To measure the aforementioned three hallmark factors in cancer cell lines after treatment with radiation in presence or absence of ATR inhibitors.
III. To detect increased interferon signalling in cancer cells in the aftermath of radiotherapy, as an innate immune response towards cytosolic DNA.

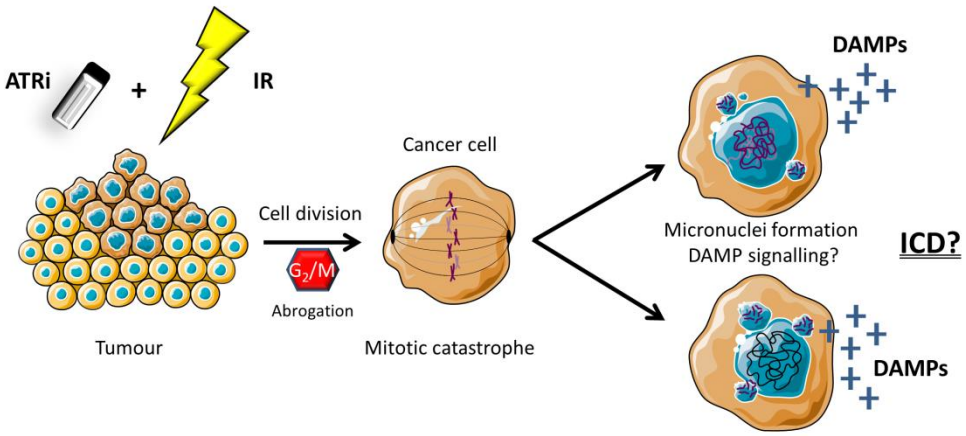

Figure 2.1. Figure showing the hypothesised rationale of co-treatment with cell cycle checkpoint inhibitors (represented by ATRi) and ionising radiation (IR) as inducer of immunogenic cell death (ICD) in cancer cells. Due to the ATRi, the G_2/M checkpoint is abrogated after radiation, and radiation-induced DNA damage will therefore not be repaired. As the cancer cells undergo cell division, this will lead to mitotic catastrophe, giving rise to micronuclei. In this project, cell death in the aftermaths of such mitotic catastophe is hypothesised to increase signalling of damage-associated molecular patterns (DAMPs), rendering the cell death immunogenic.

3 Materials

3.1 General items

Item:	Product:	Supplier:	Catalogue number:
U2OS cells	U-2 OS (ATCC HTB-96)	ATCC	HTB-96-
A549 cells	A549 (ATCC-CCL-185-)	ATCC	CCL-185-
H1975 cells	NCI-H1975 [H-1975, H1975] (ATCC-CRL-5908-)	ATCC	CRL-5908-
Growth medium	Gibco DMEM (1X) + GlutaMAX-I	Life Technologies	31966-047
Growth medium	Gibco RPMI 1640 (1X) + GlutaMAX-I	Life Technologies	61870-044
PBS	Gibco PBS pH 7.2 (1X)	Life Technologies	20012-068
PBS	Gibco PBS pH 7.4 (10X)	Life Technologies	70011-051
Serum	Biowest Foetal bovine serum of South American origin	VWR	S1810-500
Antibiotics	Gibco Pen Strep (penicillin streptomycin, liquid)	Life Technologies	15140-122
Trypsin	Gibco 0.25% Trypsin-EDTA	Life Technologies	25200-056
Trypsin	Gibco TrypLE Express	Life Technologies	
ATR inhibitor	VE822	Selleckchem	S7102-10mg
ATR inhibitor	AZD6738 ATR inhibitor	Selleckchem	S7693-5MG
WEE1 inhibitor	MK1775	Selleckchem	S1525-10mg
CHK1 inhibitor	AZD7762 hydrochloride	Axon Medchem	Axon 1399-5mg
Etoposide		Gift from the clinic	
Mitoxantrone	Mitoxantrone dihydrochloride	Sigma-Aldrich	M6545-10MG
Ethanol	Absolute ethanol	VWR Chemicals	20821.310

3.2 Flow cytometry

Item:	Product:	Supplier:	Catalogue number:
Primary antibody	Anti-Calreticulin antibody [EPR3924] – ER Marker ab92516 (mRb)	Abcam	ab92516
Primary antibody	Anti-Calreticulin antibody ab2907 (pRb)	Abcam	ab2907
Secondary antibody	Invitrogen Alexa Fluor 488 donkey anti-Rb IgG	Life Technologies	A21206
DNA stain	Hoechst 32258	Sigma-Aldrich	14530 SIGMA
DNA stain	Hoechst 33342	Calbiochem	382065
DNA stain	Propidium iodide	Calbiochem	537059
DNA stain	Invitrogen FxCycle Far Red	Life Technologies	F10348
RNase	Life Technologies Invitrogen PureLink Rnase A	ThermoFisher Scientific	12091021
Cell stain	Pacific Blue Succinimidyl Ester, 5mg	ThermoFisher Scientific	P10163
Flow tubes	Falcon 5ml Polystyrene Round-Bottom Tube with Cell-Strainer Cap	VWR International	734-0447

3.3 Immunofluorescence microscopy

Item:	Product:	Supplier:	Catalogue number:
Primary antibody	Anti-Calreticulin antibody [EPR3924] – ER Marker ab92516 (mRb)	Abcam	ab92516
Primary antibody	Anti-Calreticulin antibody ab2907 (pRb)	Abcam	ab2907
Primary antibody	Roche Anti-GFP (mMouse)	Sigma-Aldrich	11 814 460 001
Secondary antibody	Invitrogen Alexa Fluor 488 donkey anti-Rb IgG	Life Technologies	A21206
Secondary antibody	Invitrogen Alexa	Life Technologies	A10037

	Fluor 568 donkey anti-mouse		
Nuclear stain	Hoechst 33342	Calbiochem	382065
Cell lysing reagent	Triton X-100	Sigma-Aldrich	T9284-100ML
Glass coverslips	Thermo Scientific Coverslips Ø 13mm, 0.17 ± 0.01mm	DNR Sentrallager	1014/12
Glass slides	Thermo Scientific Glass slides, 76x26mm	DNR Sentrallager	RH21088
Mounting medium	Vectashield mounting medium (with DAPI)	VECTOR Laboratories	H-1200
Mounting medium	Mowiol 4-88 250g	Sigma-Aldrich	81381

3.4 ATP measurements

Item:	**Product:**	**Supplier:**	**Catalogue number:**
CellTiter-Glo reagent	*CellTiter-Glo® Luminescent Cell Viability Assay*	Promega	G7572
96-well plate	Corning Costar 3610 96 Well Assay Plate, white with clear bottom	Sigma-Aldrich	CLS3610-48EA
ATP standard	rATP, 10mM	Promega	P1132

3.5 Transfection

Item:	**Product:**	**Supplier:**	**Catalogue number:**
Plasmid with *GFP-HMGB1*	Human HMGB1 ORF mammalian expression plasmid, N-GFPSpark tag	Sino Biological Inc.	HG10326-ANG
E. coli TOP10 bacteria		Gift from B. Grallert	
SOC medium		Gift from B. Grallert	
Kanamycin	Kanamycin	Sigma-Aldrich	K0254-20ML
Maxiprep kit	HiSpeed Plasmid Maxi Kit (25)	Qiagen	12663
Transfection medium	Gibco Opti-MEM I (1X) + Glutamax-I Reduced serum medium	Life Technologies	51985-026

Transfection reagent	Promega FuGENE HD Transfection Reagent	Nerliens Meszansky	E2311
Hygromycin	Hygromycin B	Sigma-Aldrich	H5527-250MG

3.6 Western blotting

Item:	**Product:**	**Supplier:**	**Catalogue number:**
Sodium chloride	Sodium chloride	Sigma-Aldrich	S3014-1KG
Magnesium chloride	Magnesium Chloride	Sigma-Aldrich	M8266-100G
Tris-HCl	Trizma® base	Sigma-Aldrich	T1503-1KG
Cell lysing reagent	Triton X-100	Sigma-Aldrich	T9284-100ML
Phosphatase inhibitor	Roche PhosSTOP *EASY*pack	Sigma-Aldrich	4906837001
Protease inhibitor	cOmplete MINI	Roche	4693124001
Benzonase	Benzonase (25U/µl)	Merck MILLIPORE	70664-3
Sodium orthovanadate	Sodium orthovanadate	Sigma-Aldrich	S6508-10G
Protein concentration measurement kit	Thermo Scientific MicroBCA Protein Assay kit	VWR International	PIER23235
Loading buffer	Lane Marker Reducing Sample Buffer, 5ml	ThermoFisher Scientific	39000
Polyacrylamide gel	Mini-PROTEAN TGX Precast Gels 4-15% (15 well)	Bio-Rad	456-1086
Molecular weight standard	Full-range Rainbow marker, 250µl	VWR International	RPN800E
Running buffer	10X Tris/Glycine/SDS Buffer	Bio-Rad	161-0772
Nitrocellulose membrane	Trans-Blot Turbo RTA Mini Nitrocellulose Transfer kit	Bio-Rad	170-4270
Transfer stacks	Trans-Blot Turbo RTA Mini Nitrocellulose Transfer kit	Bio-Rad	170-4270
Transfer buffer	Trans-Blot Turbo RTA Mini Nitrocellulose Transfer kit	Bio-Rad	170-4270
Ponceau stain	Ponceau S solution, 1l	Sigma-Aldrich	P7170-1L
Tween	10% Tween 20	Bio-Rad	161-0781
Milk powder	Skim Milk Powder for microbiology	Sigma-Aldrich	70166-500MG
Primary antibody	Santa Cruz Anti-	Santa Cruz	sc-8394

	pSTAT1 (T701)	Biotechnology	
Primary antibody	Cell Signaling Anti-pSTAT1 (Tyr701) (58D6) Rb mAb	BioNordika	9167S
Primary antibody	Santa Cruz Anti-STAT1 p84/p91 (C-136)	AH Diagnostics	sc-464
Primary antibody	Anti-Calreticulin antibody ab2907 (pRb)	Abcam	ab2907
Primary antibody	Anti-HMGB1	Santa Cruz Biotechnology	sc-56698
Primary antibody	Anti-pDNA-PKcs (phospho-S2065)	Abcam	ab18192
Primary antibody	Anti-PNUTS Mouse mAb	BD Biosciences	611060
Primary antibody	Cell Signaling Anti-pCHK2 (phospho-Thr68) Rb	BioNordikaBergman	2197s
Primary antibody	Anti-Actin Rb	Sigma-Aldrich	A5060 SIGMA
Primary antibody	Anti-CDK1 (CDC2) Mouse mAb	Santa Cruz Biotechnology	sc-54
Primary antibody	Anti-γH2AX (phospho-S139) [EP854(2)Y]	Abcam	ab81299
Primary antibody	Anti-H4 pan Rb	Upstate-Millipore (Merck)	05-858
Secondary antibody	Horseradish peroxidase (HRP) conjugated goat anti-Rb	Jackson ImmunoResearch	111-035-144
Secondary antibody	Horseradish peroxidase (HRP) conjugated donkey anti-mouse	Jackson ImmunoResearch	715-035-150
ECL	Thermo Scientific SuperSignal West Pico Chemiluminescence Substrate	VWR International	PIER34080
ECL	Thermo Scientific SuperSignal West Dura Extended Duration Substrate	VWR International	PIER34076
ECL	Thermo Scientific SuperSignal West	VWR International	PIER34095

	Femto Maximum Sensitivity Substrate		
Stripping buffer	ReBlot Plus Mild Solution (10X)	Millipore	2502

3.7 Buffer list

Buffer:	**Content:**
Flow cytometry live cell harvest buffer	10X PBS pH 7.4 diluted to 1X in mQ water, with 1% (final volume) FBS
Western blotting lysis buffer (immunoprecipitation buffer)	As shown in table 4.3.
SDS-PAGE running buffer	10X Tris/Glycine/SDS buffer diluted to 1X in mQ water
Western blotting transfer buffer	200ml 5X transfer buffer 200ml absolute ethanol 600ml dH_2O

4 Methods

4.1 Cell culturing

All cell culturing was performed in sterile surroundings, and the cells were incubated at 37°C with a humidified atmosphere of 5% CO_2. Regular passaging of cells was conducted with use of trypsin. Growth medium was removed from the culture flask and the flask was washed with 1X phosphate buffered saline solution (PBS), before the cells were flushed with 1X 0.25% trypsin-EDTA for 20 seconds. Redundant trypsin was removed and the flask was incubated for 1-4 minutes, until the cells spherified and detached from the culture flask. The remaining trypsin was then inactivated by addition of medium. Upon seeding of cells for experiments, the cell concentration was measured by diluting 500µl of cell suspension in 9.5ml 0.9% NaCl solution (*i.e.* 1:20), before this cell suspension was injected and counted in a Beckman Coulter Life Sciences Coulter Counter Z2.

Table 4.1. Table showing different culturing vehicles used in the project, with their growth area and the used amounts of culturing medium, phosphate-buffered saline solution (PBS) for washing and trypsin-EDTA for sub-culturing/harvest.

	Growth area:	Medium, ml:	PBS, ml:	Trypsin, ml:
T-175 culture flask	175cm^2	25	20	3
T-75 culture flask	75cm^2	12	10	2
T-25 culture flask	25cm^2	6	6	1
6cm petri dish	28.27cm^2	3	2	1
35mm petri dish	9.62cm^2	2	2	1

4.1.1 Cell lines

For this project, experiments were conducted in U2OS, A549 and H1975 human cancer cell lines. The U2OS human osteosarcoma adherent cell line was isolated from the tibia (shinbone) of a 15 years old Caucasian female in 1964, under the name of 2T cells. The U2OS cells are characterised as hypertriploid, and wildtype for *TP53* (*www.lgcstandards-atcc.org*) [164]. The A549 human carcinomatous lung cell line was isolated from the lungs of a 58 years old Caucasian male in 1972. A549 may be cultured both adherently and in suspension. The A549 cells are hypotriploid, and are *CDKN2A* (Cyclin-dependent kinase inhibitor 2A) and

KRAS mutated (*www.lgcstandards-atcc.org*)[164]. The H1975 human adenocarinomatous non-small-cell lung cancer (NSCLC) adherent cell line was isolated from a female non-smoker in 1988 (*www.lgcstandards-atcc.org*). The H1975 cells are *CDKN2A* and *TP53* mutated [164].

U2OS and A549 cells were grown in Dulbecco's modified Eagle's medium (DMEM) supplemented with 10% foetal bovine serum (FBS) and 1% antibiotics solution of 50 *IU*/ml penicillin and streptomycin (pen-strep). H1975 cells were grown in Roswell Park Memorial Institute 1640 (RPMI 1640) medium supplemented with 10% FBS and 1% pen-strep 50 *IU*/ml. The cultured cells were visually checked for infection and growth abnormalities on a daily basis, and split upon reaching approximately 90-100% confluency (1:10 every second day (1:15 over week-ends) for U2OS and A549, and 1:6 every second-to-third day (1:8 over week-ends) for H1975). Prior to project start-up, the cell lines were tested for *Mycoplasma* infection. The cell line authenticities were verified by short tandem repeat (STR) DNA profiling.

4.2 Generation of GFP-HMGB1 fusion protein expressing cells

Transfection is a molecular biology technique in which the result is a cell line expressing one or several desired genes. Bacteria-based transfection is executed by incorporating the desired genes into a plasmid vector, for then to incubate the vector solution together with bacteria. The bacteria will acquire the plasmids in a process called transformation. The plasmids are then amplified inside the bacteria through replication of both chromosomal and extrachromosomal DNA, which gives a large-scale amplification of the plasmid vector. The plasmid vector can thereafter be isolated and added to a human cell line of choice, where the genes of the plasmid can be either transiently expressed or stably incorporated into the cells' genomic DNA.

In this project, transfection was conducted with the plasmid vector pCMV3-N-GFPSpark with *gfp*-tagged *HMGB1*. The plasmid contains a gene encoding kanamycin resistance for bacterial selection and a gene encoding hygromycin resistance for eukaryotic selection (figure 4.1).

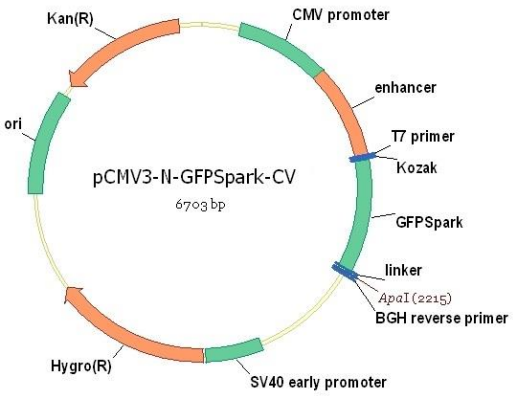

Figure 4.1. Plasmid map showing the sequence content of the pCMV3-N-GFPSpark vector as given by the manufacturer Sino Biological.

4.2.1 Protocol for large-scale amplification of the plasmid vector

The widely used laboratory strain *E. coli* TOP10 cells were thawed on ice, before 50µl of this bacteria solution was transferred to a sterile Eppendorf tube. The bacteria were then given 5µl of plasmid solution. The plasmid solution was generated by dissolving lyophilised pCMV3-N-GFPSpark vector, containing a GFP tagged HMGB1 protein gene, according to manufacturer's protocol. The resulting solution of plasmids and bacteria was incubated on ice for 30 minutes. Following the incubation, the solution was heat-shocked at 42°C for 35 seconds, for then promptly to be put on ice for 2 minutes. The heat-shocking produces small, non-lethal ruptures in the plasma membrane of the bacteria, through which the plasmid vectors can pass. Placing the heat-shocked cells on ice gives the cells adequate milieu to recover from the shock.

The solution was thereafter added 220µl (four times the amount of the solution) 37°C Super optimal broth with catabolite repression (SOC medium), and incubated with 225rpm shaking at 37°C for 1 hour.

25µl of the incubated solution were then plated onto a 50µg/ml kanamycin lysogeny broth (LB) agar plate. The addition of kanamycin to the LB agar plate enables selection of bacteria in possession of the plasmid of interest, as these are the only bacteria resistant towards kanamycin. The residual solution was centrifuged at 4000 x *g* for 5 minutes, before the resulting pellet was resuspended in 100µl of its constituent supernatant and plated onto a 50µg/ml kanamycin LB-agar plate. Plating the bacteria in two concentrations enables the

selection of formed, separate colonies from a plate with satisfying growth. The two plates were incubated at 37°C over-night, and inspected and stored at 4°C the following morning. In the afternoon, three isolate colonies from the non-concentrated sample were transferred to individual 15ml tubes containing 3ml LB with 50µg/ml kanamycin. The tubes were incubated in a 225rpm rotating 37°C water bath over-night.

The subsequent day, 10µl of the highest-density tube sample were added to 100ml LB medium with 50µg/ml kanamycin, and incubated in a 225rpm rotating 37°C water bath over-night. The remaining samples were stored at 4°C.

The selected sample was then distributed to two 50ml tubes, and centrifuged at 4800 x *g* for 10 minutes. The supernatants were discarded, and the two pellets were combined. The plasmids were isolated from the bacteria by use of a Qiagen HiSpeed maxiprep kit. Maxiprep is a plasmid isolation procedure in which plasmids from lysed bacteria are purified and eluted in different steps of buffer addition and centrifugal filtration. Plasmid concentration were thereafter analysed with Thermo Scientific NanoDrop 2000, and the sample was aliquoted and stored at -80°C. The NanoDrop performs a spectrophotometrical analysis of the purity of any nucleic acid solution by comparing the solution's absorbance at 260 and 280nm. Nucleic acids have absorbance maxima (A_{max}) at 260nm, whereas prevailing compound impurities have A_{max} around 280nm. Thereby, the ratio of A_{260}/A_{280} reflects purity. A DNA solution with a ratio of approx. 1.8 is generally considered pure.

4.2.2 Transfection procedure

The transfection of U2OS and H1975 cells was conducted by adding 2µg DNA (6.36µl plasmid solution) to 100µl room tempered Opti-MEM I Reduced Serum Medium in an Eppendorf tube. The solution was gently tapped, before 3µl of hand warmed Promega FuGENE HD transfection mix was added. The ratio of transfection mix to DNA was determined by optimisation experiments (see section 5.3.1). The FuGENE-mediated transfection is based upon the formation of a transporting, non-liposomal complex with DNA, which enables the DNA to enter through the cell membrane and the nuclear envelope. Once inside the cell, the delivered DNA may incorporate into the chromosomal DNA of the host cell, producing transient or stable expression of the introduced DNA. After the addition of the FuGENE

transfection mix, the tube was tapped and briefly vortexed, and incubated at room temperature for 15 minutes. From there, the transfection solution was added drop-wise to a ready-grown plate of cells.

For selection of stably transfected cells, the sample was supplied with medium containing 1:250 50mg/ml hygromycin B. The sample was selected for two weeks prior to usage, until all cells of a non-transfected control sample grown in presence of the selection agent at equal concentration had died. Transiently transfected samples were not selected with hygromycin, and exclusively used within 48 hours after transfection.

4.3 Irradiation

Irradiation of cell samples was conducted by use of a 160kV Faxitron Corporation CP-160 X-ray irradiation cabinet. For radiation doses ≤10Gy, samples were irradiated at a distance to the X-ray tube corresponding to 1Gy/minute until achieved radiation dose. For irradiation doses >10Gy, samples were irradiated at a distance yielding 3.64Gy/minute until achieved radiation dose.

The samples were placed on a rotating plate during the irradiation, and always centred as close as possible to the centre of the radiation field.

4.4 Flow cytometry

4.4.1 General principle

Flow cytometry is a widely used and well-established technique in biological research. Flow cytometry can be used for single-cell analysis, and utilises light properties and deflection for the detection of specific factors in the cell sample.

The fluidics of the flow cytometry technique is based on the Coulter principle. When injected into the cytometer, an air pressure moves the cell suspension of a sample into a flow cell chamber, where the sample is surrounded by a sheath fluid of water or saline buffer to make a laminar flow [165](reviewed in [166]). By adjusting the flow of the tubular sheath fluid and the cell sample core fluid, the core flow can be hydrodynamically focused down to a

diameter of about 10µm. Hence, the core flow may align the cell sample to a single-cell level [165].

Light, most commonly laser light, is then used for the analysis of the single cells. Flow cytometers usually have several different lasers, and the combination of lasers can be customised. The laser lights used for analysis are shaped and focused through series of lenses, eventually leading the light towards the flow cell. As the cells of the sample cross the path of the laser light, the light will deflect proportionally with the properties of the passing cells, and deflections are then collected by photodetectors arranged at appropriate angles to the laser beam (reviewed in [166]).

The fundamental light deflections of flow cytometry are forward scattering, in which the light is diffracted along the laser beam axis, and side scattering, in which light is refracted at an angle of approximately 90° on the axis of the laser beam. The forward scatter is thereby proportional to the surface area – or the size – of the cell, whereas the side scatter is proportional to the intracellular granularity and complexity of the cells. The side scatter is also susceptible to fluorescent light (*e.g.* from dyes or fluorophore-conjugated antibodies) emitted at this angle (reviewed in [166]).

The detection of light will, after different amplifications, be converted to an electrical voltage. Cells passing the laser beam will affect the light detection, and a passing cell thereby leads to an elevation from the threshold baseline of the voltage signal. In this way, the height, width and area/integral of the elevated voltage peak may be used when analysing the flow cytometry results. Voltage pulses will thereafter be converted into electrical currents that eventually end up in a computer (reviewed in [167]). Here, the signals from the cytometer will be digitalised and presented after the investigator's preference [166].

4.4.2 Use of fluorophores

It is common to use flow cytometry for detection of fluorophores or fluorescent dyes binding to specific components of the cells in the sample, *e.g.* DNA staining dyes or antibody-facilitated binding of fluorophores to proteins. When the content-specific fluorophores are hit with light of appropriate wavelength, this yields a particular excitation of electrons in the compound. As the electrons fall back to their lower-energy ground states in radiative

transitions, excess energy is emitted as light [165]. The light emissions of fluorophores are known, and thereby detection of this light reflects the fluorophore-binding cellular compound.

The wavelength difference between the maximal absorbed light (the excitation light) and the emitted light after the excitation of electrons in the fluorophore, is called the Stoke's shift. Emitted light after an excitation is always of lower energy than the initial excitation energy, as some of the energy will be lost in non-radiative transitions along the path down to the ground state. For optimal detection of emitted light, it is important to achieve as distinct absorption and emission peaks as possible. In other words, the higher the Stoke's shift, the better the detection [165]. Equally as important is to avoid usage of different fluorophores that overlap in excitation and emission energy, as this will lead to unspecific signals [168].

For the selective detection of preferred emitted light, *i.e.* the wavelength at maximum emission for a particular fluorophore, dichroid mirrors and filters can exclude unwanted wavelengths before the light reaches the detectors [165, 166]. The filters can be of band pass, short pass or long pass type. Band pass filters exclude all wavelengths but a narrow range at the preferred emission peak, whilst short pass filters only let light of exact or shorter wavelengths through and long pass filters on the other hand only let exact or longer wavelengths through (reviewed in [166]).

4.4.3 Barcoding – general principle

To expose different samples to the very same environments and antibody concentrations, and thereby exclude potential differences and errors, different samples can be combined into one sample after being barcoded. The barcoding is a staining technique, in which different samples are stained with different concentrations of an initial stain. This stain will only be used for later separation of the samples in the same cytogram, and should therefore stain a common feature that is not under investigation. As the combined sample is run on the flow cytometer, the resulting dotplot cytograms will present separate populations of cell signals, proportional to the different barcoding stain concentrations. In this way, the cytogram will depict the different samples of the combined run somewhat similar to a barcode [169].

4.4.4 Cell harvesting procedure for flow cytometry

To harvest cell samples, the medium was transferred from the samples into 15ml tubes, and the cells were washed with 1X PBS. The PBS was transferred to the 15ml tubes, and the cells were detached from the plates with trypsin or TrypLE Express for 2-3 minutes. The trypsin or TrypLE Express was then inactivated by addition of medium. Finally, the plates were flushed six times with the medium and the subsequent suspensions were added to their respective tubes.

As one of the aims of this project was to optimise experimental protocols for measurements of ecto-CRT presentation and HMGB1 exodus, the detailed protocols for flow cytometry are placed in the Results section (section 5). The flow cytometry experiments were run on a BD LSRII flow cytometer coupled to the software BD FACSDIVA 6.1.3 or 8.0.2. Flow cytometric analysis was conducted by use of the software FlowJo version 10. The barcoded samples were separated in the software as described above (see section 4.4.3 Barcoding).

4.5 Immunofluorescence analysis

For immunofluorescence analysis, cells were grown onto glass coverslips. This was done by plating the cells into petri dishes lined with coverslips. For sample harvest, the medium was removed and the samples were washed with 1X PBS. Thereafter, the samples were fixated with 1ml -20°C 99% methanol (MeOH) for 10-15 minutes. The methanol was removed, and the samples were washed twice with 1X PBS. 1X PBS was then added to the coverslips, before storage at 4°C.

(For pre-fixation staining, the coverslips were washed with 1X PBS and transferred to a dry surface. 100µl primary antibody diluted in medium containing 10% FBS and 1% pen-strep were then added to the cells. The coverslips were incubated at room temperature for 1 hour, before washing with PBS and MeOH fixation).

After fixation, the cell samples were permeabilised with 1ml 1X PBS/0.2% Triton X-100 for 5 minutes, before they were washed in 1X PBS. The coverslips were then transferred to a new, dry surface and 100µl primary antibody diluted in medium were added to each of them

(table 4.2). They were then incubated under lid at room temperature for 1 hour, and thereafter washed three times in 1X PBS.

For secondary antibody staining, the coverslips were transferred to a new, dry surface, before 100µl secondary antibody diluted in medium were added (table 4.2). They were subsequently incubated in the dark at room temperature for 30 minutes, before they were washed in 1X PBS.

Following the antibody staining, the coverslips were transferred to a new, dry surface. 100µl of Hoechst 33342 0.6µg/ml (in PBS) were added for nuclear staining, and the coverslips were incubated in the dark for 5 minutes. The coverslips were then washed once in 1X PBS, before they were dipped three times in mQ dH_2O and mounted onto object glass with 3µl mowiol solution. The mounted samples were hardened in the dark over-night, and thereafter stored in the dark at 4°C.

Stained coverslips were analysed by use of a Zeiss Imager.Z1 fluorescence microscopy fitted with Zeiss ApoTome and AxioCam MRm. The microscope was coupled to the software AxioVision Rel 4.8. Samples were observed at 40X magnification.

Table 4.2. The table enlists the different primary and secondary antibodies and their employed dilutions used in the immunofluorescence analyses of the project.

Primary antibody:	Dilution:	Secondary antibody:	Dilution:
α-calreticulin (rabbit)	1:100, 1:250	Alexa Fluor 488 α-rabbit	1:1000
α-cyclin B (mouse)	1:250, 1:200	Alexa Fluor 568 α-mouse	1:1000
α-GFP (mouse)	1:250		

4.6 Western blot

Western blotting is a widely used technique for quantitative protein analysis. To perform a Western blot, cell samples are lysed, and proteins in the resulting cell lysates are separated by size in a sodium dodecyl sulphate (SDS) polyacrylamide gel electrophoresis (SDS-PAGE). The separated proteins are then transferred (blotted) onto a membrane of either nitrocellulose or polyvinylidene difluoride (PVDF). Specific proteins on the Western membrane may thereafter be detected by antibody staining.

4.6.1 Procedure for cell lysis

Cell samples were washed with 1X PBS, before the PBS was removed, and the sample dishes were stored at -80°C for at least two hours. The lysis buffer was made as an immunoprecipitation buffer:

Table 4.3. Table showing the different contents of the lysis buffer, with their amounts and function.

Reagent:	Amount:	Function:
NaCl, 1M	200µl	Salting-in of chromatin proteins
$MgCl_2$, 0.5M	40µl	Salting-in of chromatin proteins
Tris-HCl, 1M, pH 7.5	500µl	pH buffer
Triton X-100	50µl	Non-ionic surfactant/detergent
'Complete Mini' tablet	1	Protease inhibition
'PhosSTOP' tablet	1	Phosphatase inhibition
mQ dH_2O	to 10ml	

To appropriate volume of lysis buffer, 4µl benzonase 25 *IU*/µl and 1µl sodium orthovanadate (Na_3VO_4) 0.1M was added per ml. Benzonase is a nuclease that degrades DNA and RNA in the samples, whilst sodium orthovanadate is a phosphatase inhibitor.

The samples were then, two at a time, slowly thawed on ice and lysis buffer (75µl for 35mm dishes, 150µl for 6cm dishes) was added. The growth surfaces were then scraped with a cell scraper, and the lysates were transferred to Eppendorf tubes placed on ice. Samples were kept cool under the whole procedure to avoid protein degradation (and thereby loss of proteins) and loss of post-translational modifications. The samples were stored at 4°C for at least 1 hour prior to gel loading, and sample remains were stored at -80°C.

4.6.2 Protein concentration measurement

Samples harvested at different time points contain different cell numbers. To ensure even loading of samples onto the SDS-polyacrylamide gel, protein concentrations were spectrophotometrically measured, and sample volumes were relatively corrected.

A protein concentration standard curve was made by serial diluting 500µl bovine serum albumin (BSA) 160µg/ml to final concentration of 80, 40, 20, 10, 5 and 2.5µg/ml. 150µl of the protein standards were loaded onto a clear 96-well plate in triplicates, with 150µl dH_2O as blanks. Next, 2.5µl of the sample lysates were loaded onto the plate in triplicates and diluted

with 150µl dH_2O. 2.5µl lysis buffer diluted with 150µl dH_2O were loaded as blanks. (Note that the plate was kept on ice during loading of sample lysates). MicroBCA solution (from Thermo Scientific *MicroBCA Protein Assay* kit) was made according to the manufacturer's protocol, and 150µl final microBCA solution were added to each samples on the plate. The MicroBCA kit is a colourimetric assay in which alkaline proteins reduce Cu^{2+} to Cu^{+}, which is detected by the formation of a 2:1 coloured complex of bicinchoninic acid (BCA) and Cu^{+}. In this way, the intensity of the produced colour correlates with the amount of proteins in the samples. The plate was incubated for 2 hours at 37°C, before spectrophotometric analysis at 562nm.

Based on the samples' protein concentrations, the sample volumes were calculated to yield 50µg proteins in a total volume of 18µl.

4.6.3 SDS-PAGE

Gel electrophoresis is a separation technique for biological macromolecules such as DNA and proteins. Gel electrophoresis is based on the travelling distance of charged molecules through a gel with fixed-size pores. The bigger the molecule, the shorter it will travel relative to time.

In SDS-PAGE, which is used for proteins, the proteins in the sample are denatured and negatively charged by use of SDS. SDS disrupts non-covalent bonds (hydrogen and disulphide bonds), and binds the proteins by hydrophobic interaction. Excessive concentrations of SDS to proteins makes all proteins end up with the same charge, thereby providing the gel separation to be solely dependent on protein size. As the samples are loaded onto the gel, and an electrical current is placed over it, the now negative proteins will travel through the gel towards the positive pole (anode), as shown in figure 4.2.

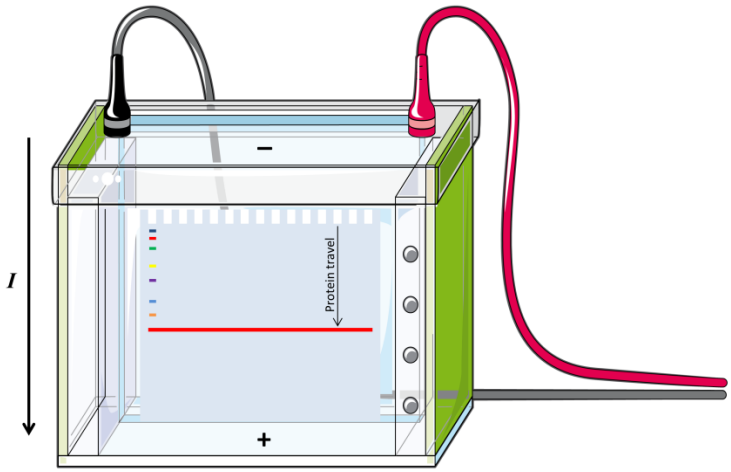

Figure 4.2. Figure showing sodium dodecyl sulphate polyacrylamide gel electrophoresis (SDS-PAGE), and how negatively charged proteins wander through the gel with the direction of the electrical current (*I*, direction indicated with arrow), towards the anode (+).

SDS-PAGE is often run with gradient gels, consisting of two or more gels of different polyacrylamide concentrations. Polyacrylamide is the gelling agent of the gel, and the ratio of *bis*-acrylamide to acrylamide is responsible for the gel pores. Hence, higher *bis*-acrylamide concentrations give rise to smaller pore sizes. Often, such gradient gels consist of two gel densities, whereof the upper gel is a concentrating gel, making all the proteins arrive at the same time for the entry into the lower, separating gel.

In the experimental protocol used, 5X loading buffer (Loading Sample Buffer, LSB) was diluted in the calculated sample volumes, and the samples were boiled at 95°C for 10 minutes. The loading buffer provided the lysates with SDS, the reducing agent dithiothreitol and glycerol for weight. 10µl of each sample were thereafter loaded onto a 4-15% gradient SDS polyacrylamide gel, next to 5µl full-range Rainbow protein size marker. SDS-PAGE was run at 200V, 400mA for 30 minutes, before the gel was washed in mQ dH_2O.

4.6.4 Western blotting

Western blotting is the process in which separated proteins in the SDS polyacrylamide gel is transferred onto a membrane by use of electrical charge (figure 4.3.). For the Western blotting, the gel was ‘sandwich’ stacked together with transfer buffer-soaked nitrocellulose

membrane and filter stacks. The sandwich stack was placed into a BioRad Trans-Blot Turbo chamber, and run at 1.3A and 25V for 7 minutes.

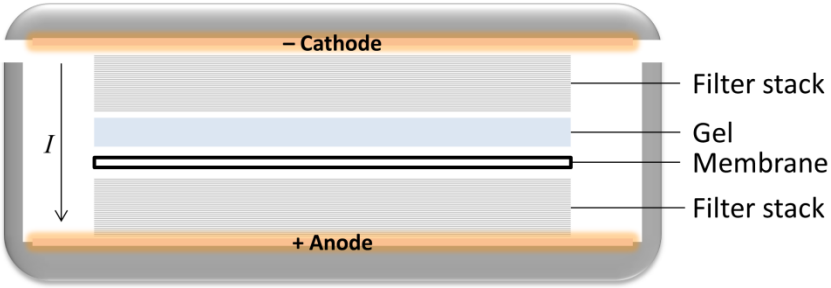

Figure 4.3. The figure shows a Western blot chamber with a sandwich stack of buffer-soaked filter stacks, SDS-polyacrylamide gel and a buffer-soaked nitrocellulose membrane. The arrow symbolise the direction of the electrical current (*I*) from the cathode to the anode.

After the blotting procedure, the nitrocellulose membrane was soaked in 0.1% (w/v) Ponceau S red stain for protein colouration, and thereafter washed in 1X PBS/1% Tween 20 (PBST). The membrane was then cut to appropriate-sized strips according to the protein size marker, and the strips were blocked in PBST/5% (w/v) fat-free skimmed milk powder on a shaker for a minimum of 30 minutes. Blocking is a procedure in which proteins (*e.g.* milk proteins) are added to minimise unspecific antibody binding to the membrane. The strips were thereafter laid onto a parafilm-covered glass plate, thoroughly dried with tissue paper and added respective primary antibodies at appropriate concentration in PBST/5% (w/v) fat-free skimmed milk powder (table 4.4). The strips were then incubated over night at 4°C.

Table 4.4. Table showing the different antibodies, the employed dilutions of the antibodies and the enhanced chemiluminescence (ECL) solution strength used for the Western blotting.

Antibody target:	Dilution:	ECL solution:
Calreticulin (rabbit)	1:1000	Dura
CDK1 (mouse)	1:400	Pico
H4 pan (rabbit)	1:5000	Dura
HMGB1 (mouse)	1:1000	Dura/Femto
pCHK2 (rabbit)	1:400	Dura
pDNA-PK (rabbit)	1:400	Dura
PNUTS (mouse)	1:1000	Dura
pSTAT1 (rabbit)	1:1000	Dura
STAT1 (total) (mouse)	1:200	Dura
γH2AX (mouse)	1:200	Pico

The subsequent day, the strips were washed with PBST, and incubated in PBST on a shaker for 5 minutes. They were thereafter returned to the parafilm plate, dried as before and added horseradish peroxidase (HRP)-conjugated secondary antibodies (α-mouse or α-rabbit) diluted 1:10 000 in PBST/5% (w/v) fat-free skimmed milk powder. The strips were then incubated for a minimum of 30 minutes at room temperature.

After the secondary antibody incubation, the strips were washed as before, and returned to the parafilm plate. The strips were dried, and added appropriate enhanced chemiluminescence (ECL) solution for 3 minutes (table 4.4). They were thereafter transferred to a transparent sheet, and analysed by use of a BioRad ChemiDoc MP.

For restaining of membranes, the membrane strips were washed in PBST, and soaked in Re-Blot Plus Mild Solution 10X strip buffer diluted 1:10 in mQ dH_2O. Following the stripping, the membranes were blocked and antibody stained as described above.

4.7 *CellTiter-Glo* assay

CellTiter-Glo Luminescent Cell Viability Assay is an assay kit intentionally used for detection of cell viability, although in this project, it was used solely for detection of secreted (extracellular) ATP. The kit is designed to quantitatively detect ATP in lysed cell samples by use of the luciferase reaction, thereby monitoring viability by relative luminescence. The *CellTiter-Glo* solution contains the protein *D*-luciferin and a luciferase enzyme. In presence of ATP, oxygen (O_2) and magnesium ion (Mg^{2+}), the luciferin will be oxidised to form oxyluciferin. This reaction will also lead to cleavage of ATP to adenosine 5'-monophosphate (AMP) and pyrophosphate (PP_i), formation of carbon monoxide (CO_2) and light emission, as shown in figure 4.4.

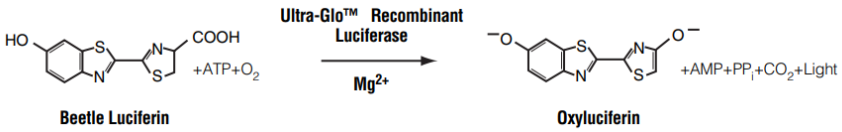

Figure 4.4. The figure shows the luciferase reaction, in which addition of luciferase and magnesium ion to luciferin in presence of ATP and molecular oxygen leads to the production of oxyluciferin, hydrolysed ATP (yielding AMP and PP_i), CO_2 and light. Figure adopted from the manufacturer's protocol (Promega Technical Bulletin for *CellTiter-Glo® Luminescent Cell Viability Assay*).

To perform the assay, 50µl of the supernatant samples were transferred onto a 96-well white clear-bottomed plate, and 50µl of the *CellTiter-Glo* solution was added. The plate was then rotated at 400rpm for 2 minutes, before the plate was incubated at room temperature for 10 minutes to let the reaction stabilise. Following the incubation, the plate was inserted into a Tecan Spark 10M microplate reader coupled to the software Spark Control Magellan 1.2 and analysed. Optimisations needed for the use of the assay to detect extracellular ATP is described in section 5.2.

5 Results

5.1 Optimisation of the calreticulin assay

To detect surface presented calreticulin – one of the hallmark biomarkers for ICD – we planned to use a flow cytometry strategy, a technique previously employed by other groups [123, 128, 129, 133, 137, 170, 171]. Flow cytometry is normally based upon staining of harvested cell samples with primary and secondary antibodies, before the samples are loaded into a cytometer, as described in section 4.4. However, measuring of cell surface proteins may not be as straight forward as with intracellular components, and several considerations and optimisations were therefore necessary for the assay to reliably detect ecto-CRT.

5.1.1 Selection of antibody and its concentration

For the selection of primary antibody targeting CRT, an immunofluorescence analysis was conducted on methanol fixated U2OS cells. As calreticulin is very redundant in the endoplasmic reticulum (ER), this was expected to yield clear staining results in the fixated cells. Two antibodies were tested, namely ab92516 and ab2907 from Abcam, of which both were tested in 1:100 dilution, and the latter additionally was tested in 1:250 dilution. The ab2907 antibody has previously been used for detection of ecto-CRT by other groups [170-172]. The result of the antibody evaluation is presented in figure 5.1.

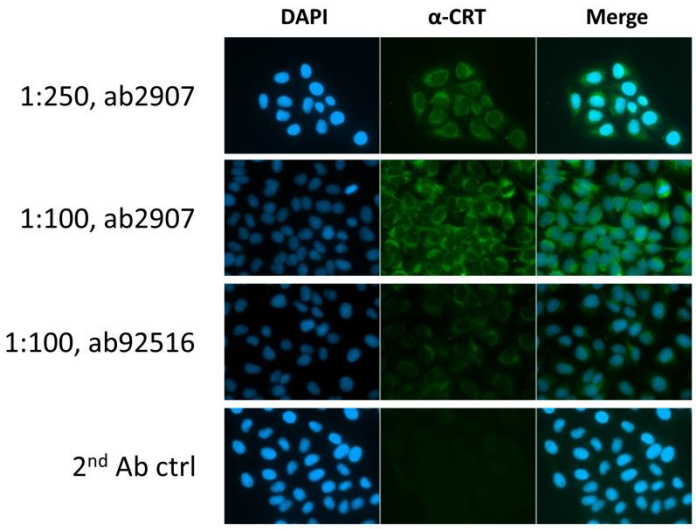

Figure 5.1. Immunofluorescence analysis of anti-calreticulin antibodies in fixated U2OS cells. The analysis was conducted with the two antibodies ab2907 and ab92516, diluted as indicated. The bottommost micrograph series shows a secondary antibody control. DAPI: nuclear stain, α-CRT: calreticulin signal, Merge: overlap of DAPI and α-CRT images.

As seen in figure 5.1, antibody ab2907 stained the total CRT of the cells far better than antibody ab92616 when applied at equal dilutions (1:100). The staining pattern of CRT in the cytoplasm close to the nucleus is consistent with its localisation in the ER. From the uppermost micrograph series, it is read that ab2907 applied in dilution 1:250 sufficiently stains the CRT signals, to almost similar degree as dilution 1:100. As dilution 1:250 is way more saving, without radically affecting the antibody signal, it was concluded that ecto-CRT was to be stained with antibody ab2907 diluted 1:250 in the following experiments.

5.1.2 Use of live cells in the assay

Performing the flow cytometric assay on live cells is more cumbersome than on fixated cells, as live cells impose time and milieu restrictions to the assay. At the same time, the CRT assay should detect calreticulin signalling presented only on the surface of the cells. Therefore, it is crucial for the assay to be executed on cells having intact plasma membranes (live cells), as perforated membranes would enable the anti-CRT antibody to diffuse into the cell and stain CRT in its ER reservoir. To verify the need for staining live cells only, a test experiment was performed for comparison of CRT staining in viable *versus* non-viable cells by flow cytometry. The use of a dye that only diffuses through perforated membranes allows for

such distinction of live and dead cells. In this case, uptake of propidium iodide (PI) was used to distinguish viable from non-viable cells. The result showed higher CRT signals in the PI positive (dead) population than in the PI negative (live) population (figure 5.2a). In addition, CRT signals from live cells were compared with the signals from fixated cells (figure 5.2b), in which the results showed exceedingly higher CRT signals for the fixated cells. It was therefore concluded that staining of live cells was needed, as the signals would otherwise be at false-positive heights, due to the combined surface and intracellular signalling. All further experiments were therefore conducted exclusively on live cells.

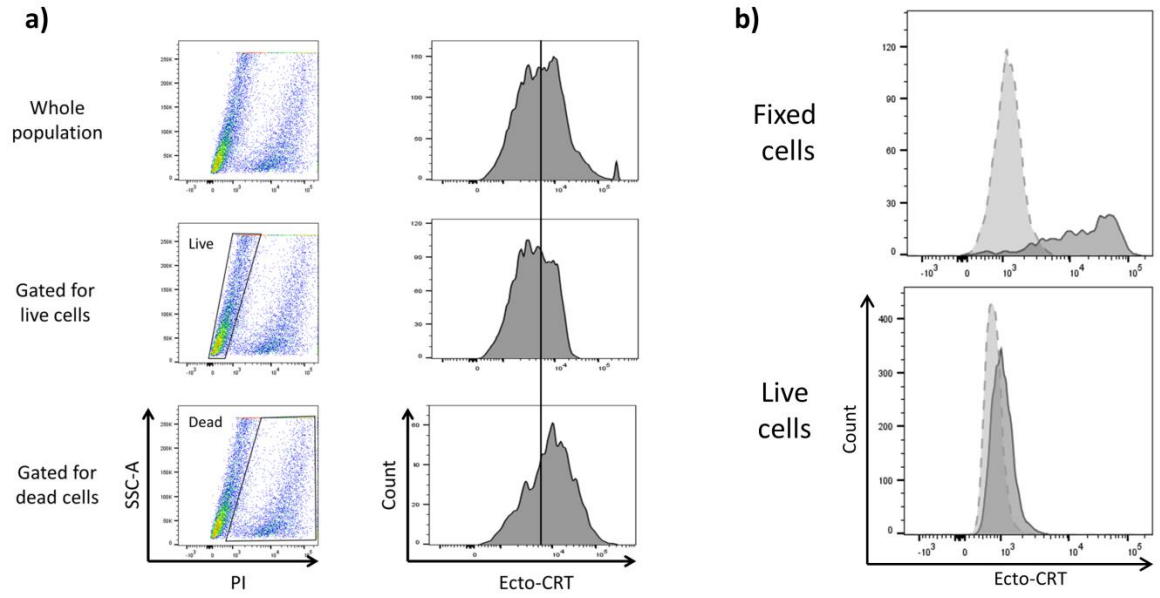

Figure 5.2. Results from experiment testing CRT staining of live, dead and fixated cells. **a)** The figure shows how the higher CRT signals of dead cells (due to intracellular and surface staining of CRT) contribute to shift the total CRT signal to a higher value than the ecto-CRT signals of live cells. Propidium iodide (PI) was used as a live/dead stain to separate live from dead cells in the sample. **b)** The CRT signal is very high for fixated cells compared to the ecto-CRT signal from live cells, as fixation perforates the cell membranes, hence leading to intracellular staining of CRT. Pale, dashed peaks represent secondary antibody controls (background), whereas solid-lined, dark peaks represent CRT staining signal.

5.1.3 Assay strategy and calculation of relative signals

With the necessity of live cells for the assay settled, live/dead staining was included to the assay. The strategy for the CRT measurements is illustrated in figure 5.3. As shown, each sample was divided to yield a secondary antibody control, before the samples were stained with either primary and secondary antibodies, or secondary antibody alone. After the

antibody staining, the samples were stained with non-permeable Hoechst 32258 or propidium iodide (PI), in order to separate live and dead cells.

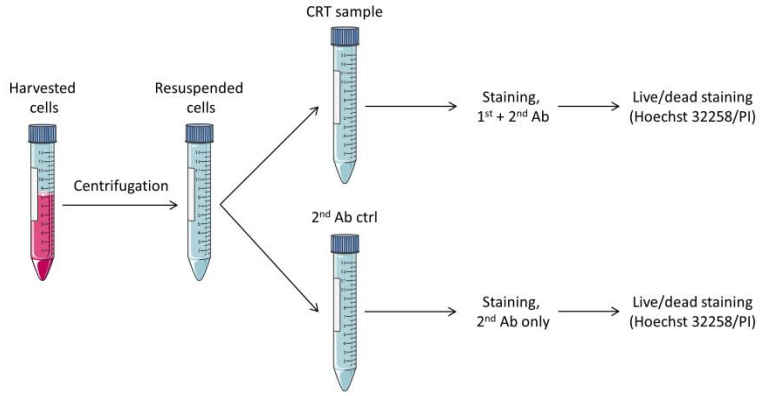

Figure 5.3. Strategy for the CRT measurements, in which each sample is divided to a sample that is stained for ecto-CRT (CRT sample) and a secondary antibody control sample (2^{nd} Ab ctrl). After staining, the two constituent samples are stained with non-permeable Hoechst 32258 or propidium iodide (PI) as a live/dead discriminating stain.

For further investigation by use of flow cytometry, the following gating strategy was used: First, single cells were selected for by gating for the neatly diagonal signals in SSC width *vs*. area (SSC-W *vs.* SSC-A) dot plots, leaving the lower blob of debris behind. As SSC detects internal complexity of cells, signals to the right of the diagonal were excluded, as these would have higher width to area ratio, indicating doublets or muliplets. With multiplets gated out, the next gating was for live cells. This was achieved by plotting Hoechst-A to either SSC-A or Alexa Fluor 488-A, followed by gating of the low-Hoechst population. From this gate, the median value of Alexa Fluor 488-A (representing ecto-CRT) could be read. An example of the gating strategy is shown in figure 5.4.

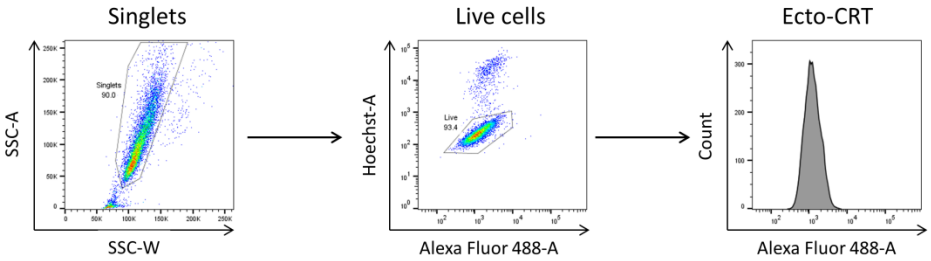

Figure 5.4. Figure showing the flow cytometry gating strategy. The strategy starts by gating of single cells (singlets) from a SSC width *vs.* area dot plot, for then to gate for live cells from an Alexa Fluor

488-A *vs.* Hoechst-A dot plot. From here, the median value for Alexa Fluor 488 (*i.e.* ecto-CRT) of the live cells could be read out.

To analyse the ecto-CRT signalling after treatment with radiation and/or drugs, the median value of a treated sample secondary antibody control was subtracted from the median value of the corresponding treated sample stained with primary antibody. This value was thereafter divided to the median value of a mock (non-treated) sample with its corresponding secondary antibody control subtracted. This yields ecto-CRT signals relative to the mock sample. The calculation is given in formula 5.1.

$$\frac{(Signal_{treated} - background_{treated})}{(Signal_{mock} - background_{mock})}$$

Formula 5.1. The formula shows how the signal from a treated sample, with its secondary antibody control background value subtracted, was divided to the signal of a mock sample with the secondary antibody background signal subtracted to yield relative ecto-CRT signals.

5.1.4 Finding a positive control for the translocation of calreticulin

The next step in the optimisation was to find a positive control for translocation of calreticulin. Several compounds have previously been used as ICD inducers, including anthracyclins, platins and etoposide (reviewed in [129]). Initially, the topoisomerase-II inhibitor etoposide (100µM) was tested in U2OS cells, as this drug already was available in the laboratory. However, the results showed no increased ecto-CRT after etoposide treatment (data not shown). Furthermore, it later came to our attention that etoposide (and also cisplatin) neither induced CRT translocation nor other ICD markers in two other studies [137, 173]. On these grounds, we concluded that etoposide was non-suitable as positive control for CRT translocation. The anthracyclin mitoxantrone (MTX) was thereafter tested as positive control in 1µM concentration, as previously employed by other groups [130, 137, 170, 172]. As mentioned in section 1.6.1, CRT translocation is thought to occur as a response to ER stress. MTX is known as a type I ICD inducer, *i.e.* a compound inducing secondary (or collateral) ER stress, as it mostly induces apoptosis from a nuclear localisation and not from the ER [121]. Results from the MTX tests are presented in figure 5.5a. The results showed increased ecto-CRT levels after MTX treatment of A549 and H1975, and partly in U2OS cells. The highest and most consistent increase was found in H1975 cells. Moreover, the ecto-CRT signals relative to the background signal (secondary antibody control) was by far highest in

H1975 cells (figure 5.5b). Based on these results of the MTX test, the H1975 cell line was selected for further investigation of ecto-CRT signalling.

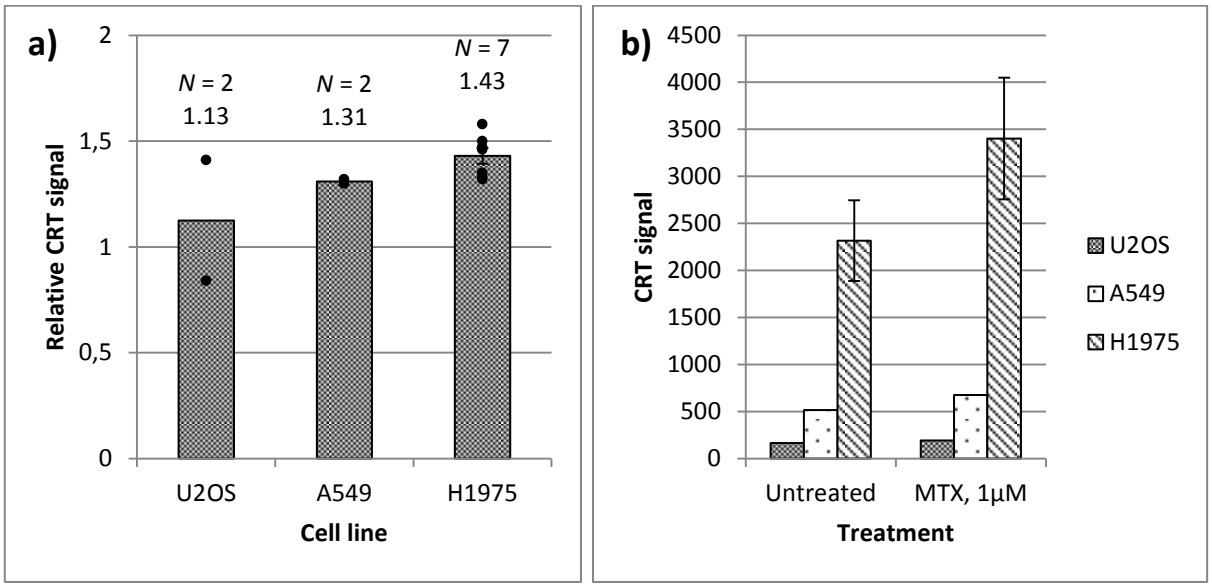

Figure 5.5. Results from experiments testing mitoxantrone (MTX) 1µM for 24 hours as positive control for CRT translocation. **a)** Ecto-CRT signals in U2OS, A549 and H1975 cells after the MTX treatment, relative to mock samples (=1). Dots represent results from individual experiments, whereas error bar indicate SEM. **b)** Signals from untreated and MTX treated U2OS, A549 and H1975 cells with the secondary antibody background signal subtracted. The signals are not relative to mock. The figure shows the overall higher raw signals in H1975 cells compared to U2OS and A549. The results are from the same experiments as the ones used in figure a. Error bars indicate SEM.

5.1.5 Harvesting method and staining temperature

When staining live cells, there are several aspects to regard, including temperature during the staining procedure. Initially, the staining procedure was performed at room temperature, in order to keep the cells at more or less decent temperatures. At the same time, the kinetics of the plasma membrane will be relatively active at this temperature. As surface-bound CRT was to be stained, this would potentially enable ecto-CRT to be internalised into the cells before and during its staining, thereby producing false-low results in the successive flow cytometry analysis. Keeping the cells on ice after harvest would impact the membrane kinetics to such extent that internalisation could be ruled out. Of note is that the samples could be kept at room temperature again after finalisation of the secondary antibody staining, as flow cytometry easily would detect internalised fully stained complexes of CRT and antibodies. The result from the temperature test showed no or minor differences

in ecto-CRT levels for cells stained at room temperature, compared to cells stained on ice (figure 5.6).

To begin with, the samples were harvested by use of conventional trypsin, as described in section 4.1. Trypsin is generally considered a harsh way of harvest from a surface marker's point of view. Therefore, harvest by use of the reagent TrypLE Express, which is developed to be less damaging to surface markers, was tested. TrypLE Express is supposed to retain surface marker signalling even after 20 minutes of exposure (*ThermoFisher Scientific*). The result from the test is presented in figure 5.6, and shows slightly higher ecto-CRT signal for cells harvested with TrypLE Express.

Although only small differences were observed between the samples, we decided to harvest the samples with TrypLE Express and stain the samples on ice, as this would reduce the risk of loss of ecto-CRT signalling.

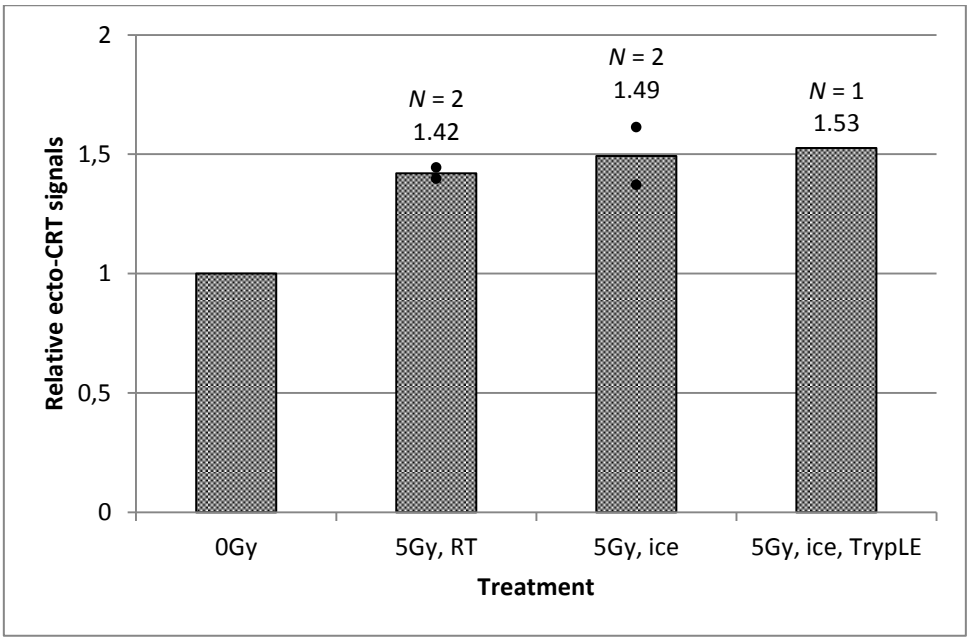

Figure 5.6. Ecto-CRT signals from irradiated H1975 samples stained at room temperature (RT) and on ice relative to a mock sample, and the relative signal from an irradiated sample harvested with TrypLE Express (stained on ice). Dots represent results from individual experiments.

5.1.6 Barcoding of mock and treated samples for more reliable results

To more accurately determine ecto-CRT signals after different treatments, we next wanted to include barcoding. If the samples that are going to be compared (in this project, treated

samples to mock samples) are analysed as individual samples, the fact that the samples are exposed to slightly different milieus during antibody staining is unavoidable. This may for instance be variations in applied volumes, cell numbers or concentrations of antibodies or stains. Hence, the reliability of the results would be reduced. To prevent such occurrences, the samples can be barcoded and combined in a single tube before the antibody staining, as described in section 4.4.3. Upon recommendation (T. Stokke), barcoding with permeable Hoechst 33342 was tested. The mock sample was initially stained with the Hoechst, before it was divided and added in portions to the different treated samples (figure 5.7). Because Hoechst stain now was used for barcoding, propidium iodide (PI) was used as live/dead stain, as PI only enters cells lacking plasma membrane integrity. The gating strategy for the barcoding is presented in figure 5.8, which shows how the live gating was conducted from PI staining, and how the two different samples could be separated by gating on the Hoechst signal. The read-out ecto-CRT signals were calculated as before (formula 5.1).

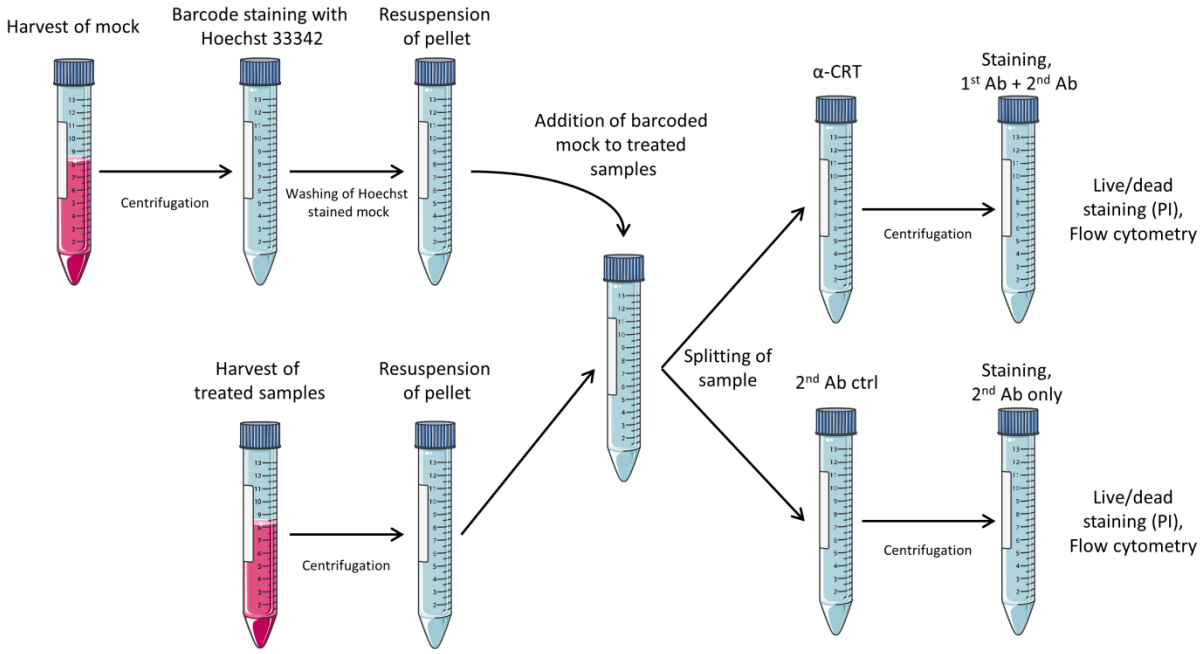

Figure 5.7. Figure depicting the work flow of the CRT assay barcoding strategy. A non-treated mock sample was initially harvested and stained with permeable Hoechst 33342, before it was divided on the remaining, treated samples. Each barcoded sample was then split in two, to produce one sample for CRT staining (α-CRT) and a secondary antibody control sample (2^{nd} Ab ctrl). These two samples for each treatment were thereafter stained with primary and secondary antibody, or only secondary antibody, respectively. Subsequently, the samples were added propidium iodide (PI) as a live/dead stain just prior to flow cytometric analysis.

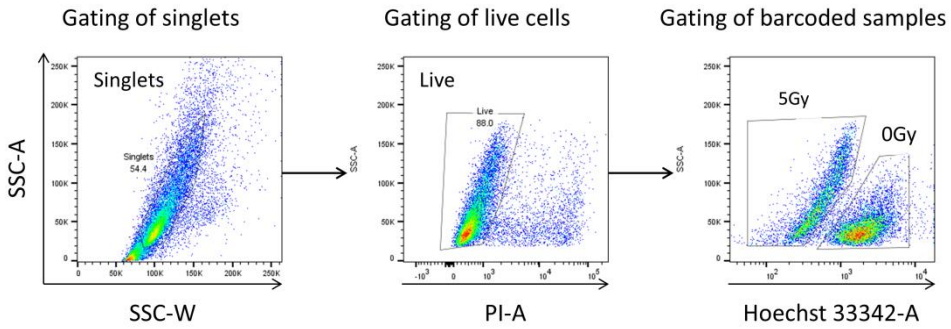

Figure 5.8. Figure showing the barcoding of mock and treated cell samples by use of Hoechst 33342. After initial gating of single cells (to the left), staining with propidium iodide (PI) was used for the gating of live cells (middle). From here, the parameter Hoechst-A divided the signals into a low-Hoechst and a high-Hoechst population, representing the unstained treated sample (named 5Gy) and the stained mock sample (named 0Gy), respectively (to the right).

To ensure that the barcoding procedure had no impact on the ecto-CRT reading, an initial experiment of two barcoded samples was conducted. In the first sample, a 0Gy sample was Hoechst stained, and combined with a 5Gy unstained sample. In the other sample, a 5Gy sample was Hoechst stained and combined with a 0Gy unstained sample. The experiment showed no shift in ecto-CRT signal exerted by the procedure (data not shown).

Hoechst stain binds the minor groove of DNA in a non-covalent fashion, and the barcoding is therefore reliable on the equilibrium state of the Hoechst stain. With time, and with Hoechst 33342 being permeable, the Hoechst stain in the mock sample will diffuse down its concentration gradient out from the cells in the mock sample and into the solvent. From there, once again because Hoechst 33342 is permeable, the Hoechst molecules may enter the cells of the initially unstained treated sample. This would lead to the formation of one equally stained population somewhere between the Hoechst values of the two samples, and it would be impossible to discriminate the samples from one another. But, as the staining procedure and the succession to the flow cytometry was fairly rapid (that is, under three hours from start of harvest until completion of flow cytometry), hastened by the use of live cells, the low extent of the Hoechst equilibration allowed for the strategy to function.

5.1.7 Optimised protocol for the detection of ecto-CRT

1) Harvest the untreated control sample: Transfer the medium to a 15ml tube, and wash the dish with 1X PBS. Transfer the PBS to the tube, and add TrypLE Express to the dish. Incubate at 37°C until cells spherify and detach from the dish. Add medium to the dish, and flush the dish six times. Transfer the cell suspension to the tube, and centrifuge at 1500rpm for 5 minutes.
2) Aspirate the supernatant, and resuspend the cell pellet in 100µl medium with 1µg/ml Hoechst 33342 for barcoding. Incubate in dark for 30 minutes, at room temperature.
3) In the meanwhile, harvest the remaining treated samples as described in step 1. Resuspend the cell pellets in 3ml 1X PBS with 1% FBS (1X PBS/1% FBS).
4) Add 3ml 1X PBS/1% FBS to the Hoechst stained sample, and centrifuge at 1500rpm for 5 minutes. Resuspend the pellet in an appropriate volume 1X PBS/1% FBS, and add equal portions of the barcoded mock sample to each of the other treated samples.
5) Split each sample to a secondary antibody control, and centrifuge all the samples at 1500rpm for 5 minutes. Put on ice.
6) Aspirate the supernatants, and resuspend the pellets of the CRT samples in 100µl medium with primary anti-CRT antibody (ab2907 Rb, 1:250). Resuspend the pellets of the secondary antibody controls in 100µl medium. Incubate in dark for 30 minutes, on ice.
7) Add 3ml 1X PBS/1% FBS to each sample, and centrifuge at 1500rpm for 5 minutes. Aspirate the supernatants, and resuspend the pellets in 100µl medium with secondary antibody (Alexa Fluor 488 anti-Rb, 1:500). Incubate in dark for 30 minutes, on ice.
8) Add 3ml 1X PBS/1% FBS to each sample, and centrifuge at 1500rpm for 5 minutes. Aspirate the supernatant, and resuspend the pellets in 500µl 1X PBS. Transfer to flow cytometry tubes, and store at 4°C until flow cytometric analysis.
9) Two minutes prior to flow cytometric analysis, add 1µl propidium iodine (PI) 1.667mg/ml to the samples, for live/dead staining.
10) Perform gating and analysis of the reads as described in figure 5.9.

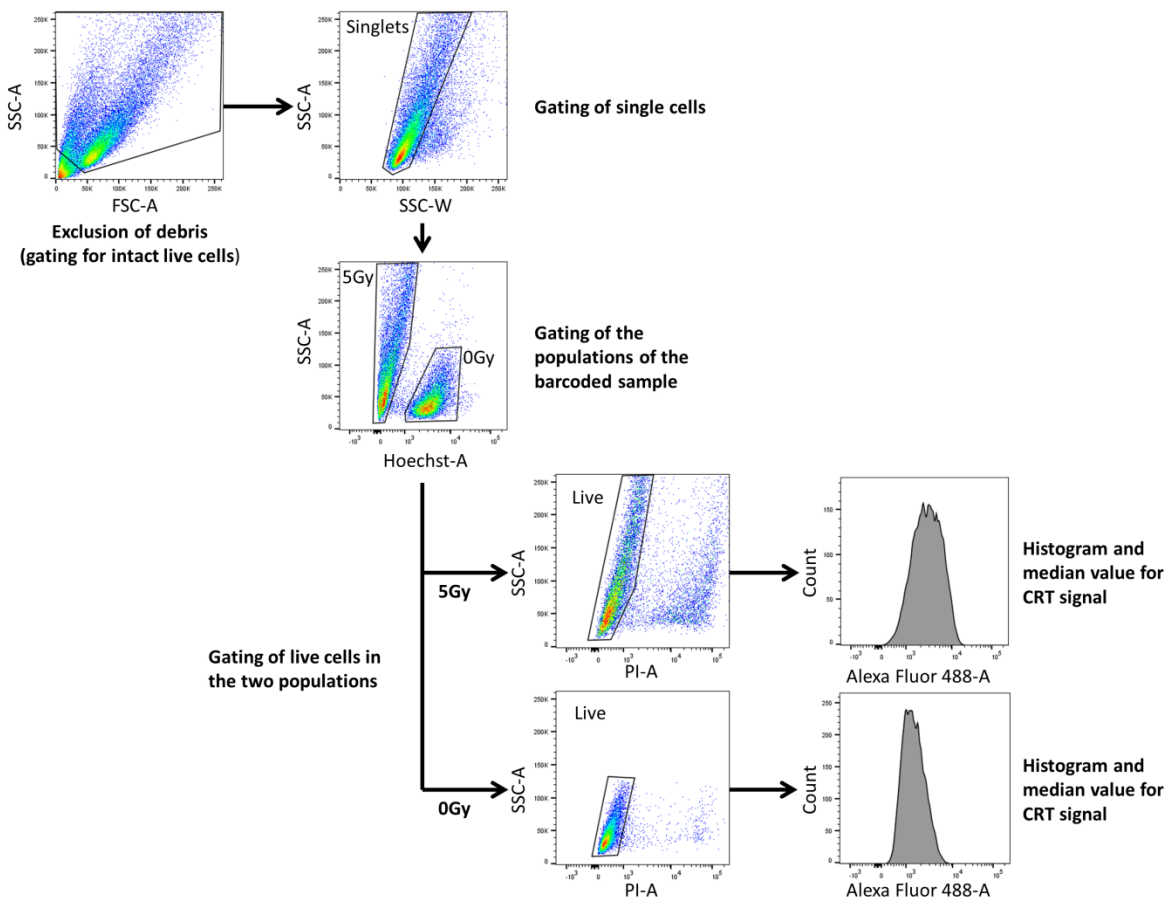

Figure 5.9. Figure showing the gating strategy of the barcoded CRT assay samples. First, cell debris was excluded from the samples by removing the lower left corner population in a FSC-A *vs.* SSC-A dot plot. Thereafter, it was gated for single cells from a SSC-W *vs.* SSC-A dot plot, before the two barcoded samples could be separated in a Hoechst-A *vs.* SSC-A dot plot. From there, the live cells were gated for the two populations by use of a PI-A *vs.* SSC-A dot plot, before histograms of the CRT signals (by Alexa Fluor 488) could be shown, and the median values of the histograms could be read.

5.2 Optimisation of the ATP assay

We set up to perform the ATP assay by luciferase-based spectrophotometrical detection of ATP in the growth medium of cells, as described in earlier literature [129, 130, 170, 174-176]. To perform the actual ATP detection, the protocol for *CellTiter-Glo® Luminescent Cell Viability Assay* kit was used, as described in section 4.7.

5.2.1 Testing MTX as positive control

As use of MTX was already settled as positive control for CRT translocation in the calreticulin assay, this anthracyclin was also tested as positive control for secretion of ATP. Initially, the

ATP assay was conducted in U2OS cells, and the results from experiments testing MTX as positive control in this cell line is given in figure 5.10. As seen, no clear elevation of signals was seen in samples treated with MTX 1µM, neither at 24 hours after treatment nor at six or four hours. MTX did therefore not appear as a good positive control for this assay.

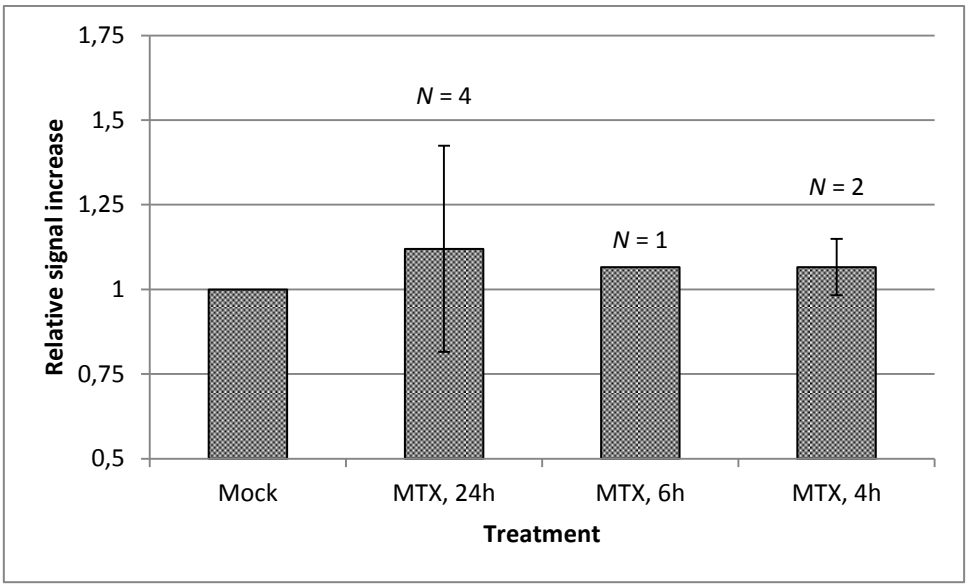

Figure 5.10. Results from experiments testing MTX (1µM) as positive control for ATP secretion in U2OS cells. The figure shows the increase in relative luminescence from MTX treated samples at 24, 6 and 4 hours, relative to a mock sample. Error bars indicate SEM.

5.2.2 Selection of cell line for the ATP assay

With the H1975 cell line chosen for further investigation in the calreticulin assay, this cell line was established as the cell line of choice in the ATP assay as well. All further investigations were therefore conducted on H1975 cells.

5.2.3 Filtration and centrifugation as means of cell exclusion

In the ATP assay, we wanted to detect secreted ATP in the growth media of treated cells by use of the *CellTiter-Glo* reagent. This reagent is a lysing agent, as the *CellTiter-Glo* kit is intended to measure viability in cell samples. Therefore, it became crucial for the ATP assay to avoid any floating or dead cells in the growth media at the time of measurement, as this would lead to unspecific detection of ATP. To begin with, the samples were centrifuged in a table centrifuge for removal of debris. In addition, filtration of the media with centrifuge filters of 0.22µm, 0.65µm and 100kDa size was tested out (data not shown). Eventually, a

two-step centrifugation was considered the cheapest and most reliable way of removing cell debris from the media, as shown in figure 5.11.

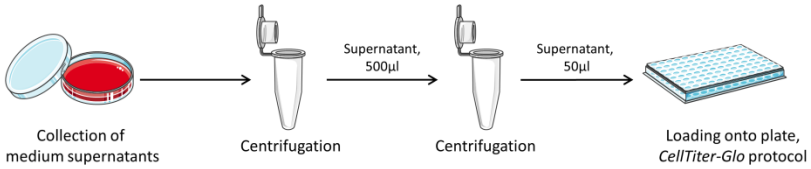

Figure 5.11. Figure depicting the work flow of the purification of medium supernatants by a two-step centrifugation. This removed all cell debris from the medium, leaving secreted ATP in suspension.

5.2.4 Heat shock as positive control for ATP secretion

Next, heat shocking of cells was tested as positive control for ATP secretion. Use of heat shock above 42°C was recently published as an inducer of ICD in several cancer cell lines (including A549), in contrast to lower-temperature heat shocks [175]. In the published paper, heat shock for secretion of ATP was conducted by placing a cell sample at 47°C for 1 hour, followed by incubation at 37°C for additional 1 hour. We therefore performed the heat shock experiment as this, in H1975 cells. As a control for the ATP secretion, H1975 cells were incubated at 37°C for 2 hours. One million H1975 cells were seeded in Eppendorf tubes for each of the samples, and the heat shock sample was thereafter placed onto a 300rpm rotating heat block at 47°C. After 2 hours, whereof both samples had been incubated at 37°C the last hour, the samples were centrifuged as described in section 5.2.3. Both the growth medium supernatant and a control of resuspended cell pellets were analysed by the *CellTiter-Glo* method. The results are presented in figure 5.12.

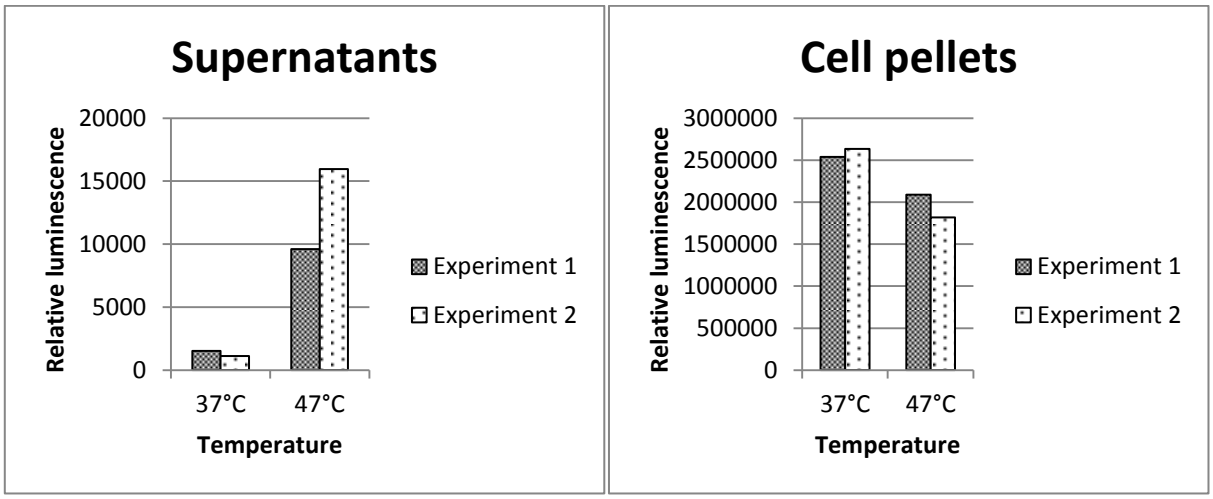

Figure 5.12. The effect of 47°C heat shock on the secretion of ATP. To the left is a plot showing the increased relative luminescence signal in the centrifuged growth medium supernatant of the heat shock samples of two experiments, whereas the plot to the right shows the relative luminescence of the corresponding cell pellets.

As shown in figure 5.12, the heat shock gave rise to a dramatic increase in secreted ATP, represented by the relative luminescence. Severe heat shock over a long time span can make cells burst. If so, all internal ATP would leak out into the medium, giving a false-positive increase in signalling of secreted ATP. Therefore, it was explored if the cells were intact before the ATP measurement. This was done by staining a small amount of the heat shocked sample with trypan blue and adding it onto a haemocytometer for observation by microscopy. Trypan blue stains perforated and dead cells. No cells were found to be stained by the trypan, and the heat shock was therefore considered a reliable and suitable positive control for the secretion of ATP.

5.2.5 The presence of serum may affect the ATP measurements

Serum may contain ATP-decaying enzymes, and as the assay should detect relatively small amounts of ATP secreted out of the cells, a serum effect as such could be devastating to the assay. At the same time, serum is a necessity for the cells, as the lack of serum disables the attachment of the cells to the growth surface, thereby leading to anoikis. On these grounds, an experiment testing the positive control with and without the presence of serum in the medium was performed. As seen in figure 5.13, the addition of serum had massive effect on the relatively low-value supernatant sample of the test experiment. Of note is that a second experiment that was conducted for validation of the result gave unclear results (most likely

due to an experimental error), and the big serum effect therefore needs further validation through additional experiments. Nonetheless – to be on the safe side – it was determined that the serum had to be removed for some time before the ATP measurements.

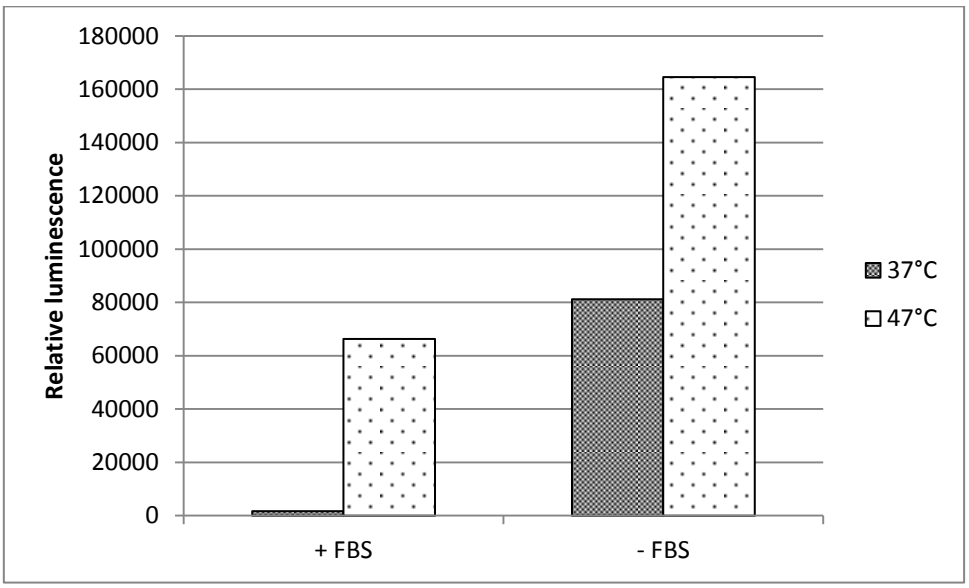

Figure 5.13. Results from an experiment monitoring ATP signals in the presence and absence of serum. The results show the effect of serum in a 47°C heat shocked sample, compared to a mock sample incubated at 37°C. As seen, the samples with presence of serum (+FBS) produced far less ATP signals than the samples without serum added to the medium (-FBS).

5.2.6 Production of values in the sensitive range of the ATP detection kit

To explore the linear range of the *CellTiter-Glo* assay, a standard curve was generated by dissolving disodium-ATP in serum-free medium to desired concentrations. Figure 5.14 shows the ATP standard curves made for eight ATP assays.

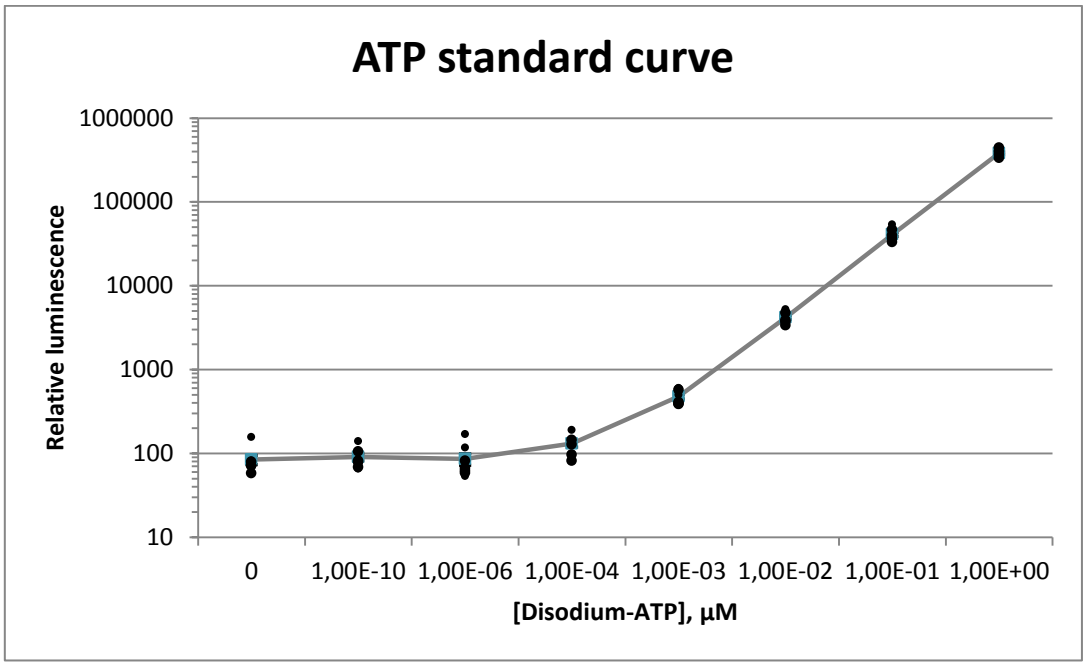

Figure 5.14. The figure shows an average ATP standard curve used for the evaluation of the obtained values in the ATP assay. Dots represent individual ATP assays, and error bars indicate SEM. *n* = 8.

In our first attempts to perform the ATP assay on adherent H1975 cells treated with IR and ATRi, the signals were relatively low, with values located below or around 1000 relative luminescence units (RLU) (data not shown). As seen in figure 5.14, the standard curve has its linear range only for values above 1000RLU. In fear of having values in a non-sensitive range of ATP detection, it was therefore desirable to elevate the signals further out along the standard curve. This was achieved in two steps. First, the amount of medium added to the sample dishes was reduced, in order to heighten the cell – and thereby the ATP – concentration. Secondly, the number of cells plated for the ATP assay was increased, so that the samples were near confluent at the time of harvest. These optimisation steps led to the plating of one million cells in 3ml medium in 6cm dishes, with the medium being replaced with 1ml serum-free medium six hours prior to harvest. Consequently, values satisfactory within the linear range were achieved, being distributed between 4000-100,000RLU.

5.2.7 Optimised protocol for detection of secreted ATP

1) Plate out $1 \cdot 10^6$ cells in 3ml growth medium in a 6cm dish for each sample. Incubate the samples at 37°C for 2-3 hours, to let the cells attach.
2) Expose the samples for the desired treatment. In this study, the samples were irradiated with 5Gy with or without ATR inhibitors (VE822 250nM; AZD6738 250nM) added to the medium. If plating cells in triplicates, make a common solution of medium with inhibitors for all triplicate samples, and replace the growth medium with the new medium.
3) After treatment, incubate the samples at 37°C for 18 or 42 hours (for detection at 24 or 48 hours after treatment, respectively).
4) 6 hours prior to medium harvest, replace the growth medium with 1ml serum-free medium (containing ATR inhibitors at appropriate concentrations, if used). Wash the dishes with 2ml 1X PBS before the addition of serum-free medium. Incubate the samples at 37°C for the remaining 6 hours (see figure 5.15).
5) At desired time point, harvest the medium supernatants by transferring the media to respective Eppendorf tubes.
6) Centrifuge the medium samples at 13400rpm for 5 minutes. Then transfer 500µl from the supernatant of each medium sample to new respective Eppendorf tubes. Make sure to pipet the medium from the centre of the tube. Centrifuge the new Eppendorf tubes again at 13400rpm for 5 minutes.
7) Transfer 50µl of the supernatants to a clear-bottomed 96-well plate, together with three serum-free medium controls, and ATP standards if wanted. Add 50µl of final *CellTiter-Glo* reagent to each sample.
8) Perform the *CellTiter-Glo* method: Rotate the plate at a shaker for 2 minutes at approx. 400rpm, and leave the plate on the bench for 10 minutes. Then analyse the plate with a plate reader (luminometer).

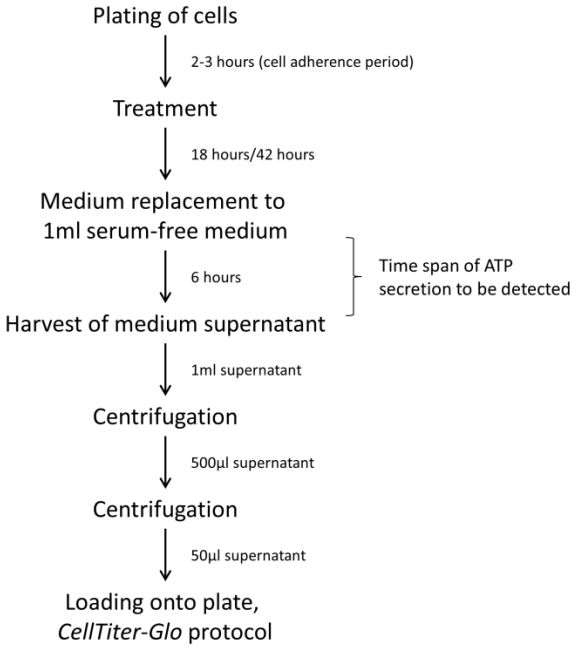

Figure 5.15. Flow chart showing the replacement of the growth medium with 1ml serum-free medium six hours before the medium was harvested for measurements. It is the ATP secreted during these six hours that is measured in the final *CellTiter-Glo* measurement.

5.3 Optimisation of the HMGB1 assay

For the HMGB1 assay, several strategies for detection were considered, including flow cytometry, microscopy and enzyme-linked immunosorbent assay (ELISA) detection. In previous literature, the ELISA approach has been widely used for detection of HMGB1 in cell supernatants, which traditionally is a necrosis assay [129, 170, 177, 178]. In addition, the generation of cells expressing *HMGB1* fused with fluorescent proteins has been used for microscopy and spectrophotometry assays [122, 178]. With the presence of a flow cytometry core facility at our department, and the relatively high expense of ELISA kits, we decided to optimise a flow cytometric assay for the initial detections of HMGB1 exodus. To detect loss of intracellular HMGB1 (*i.e.* residual intracellular HMGB1 after exodus), we transfected cells with a *GFP-HMGB1* fusion protein gene.

5.3.1 Transfection of cells with the *GFP-HMGB1* fusion gene.

The first step in the optimisation of the HMGB1 assay was to transfect cell lines with a plasmid vector containing the fusion gene *GFP-HMGB1*. This would lead to over-expressed

HMGB1 transcripts, and the additionally expressed HMGB1 proteins would now be tagged with GFP as a reporter. Table 5.2 shows the outcome of the bacterial transformation and amplification of the plasmid vector.

Table 5.2. Outcome of the amplification and purification of the plasmid vector containing the *GFP-HMGB1* fusion gene. From left: Concentration, absorbance at 260nm (A_{260}), absorbance at 280nm (A_{280}) and the ratio of the absorbance at 260nm to the absorbance at 280nm (260/280).

	Outcome:	**A_{260}**	**A_{280}**	**260/280**
Final plasmid solution	314.3ng/µl	6.287	3.302	1.90

As seen in table 5.2, the outcome of the plasmid isolation was 314.3ng/µl, which is considered good. To check the purity of the isolated DNA solution, one can measure the ratio of the absorbance at 260nm to 280nm. This is based on the absorbance maximum of nucleic acids at wavelengths of 260nm, whereas contaminants as reagents used in the purification protocol tend to absorb light of ≥280nm. It is generally assumed that a 260/280 ratio of approx. 1.80 reflects a pure DNA sample [179]. On these grounds, the produced plasmid concentration, with a 260/280 ratio of 1.90, was considered pure.

Initially, we planned to make stable transfectants with the plasmid vector, but the transfected cells lost their GFP signal after two to three weeks of culturing (data not shown). We therefore decided to use transient transfections, in which the *GFP-HMGB1* fusion gene was not incorporated into the host cells' chromosomal DNA. As the gene was only transiently expressed, all the experiments for this assay were conducted within 48 hours after transfection. Figure 5.16 presents the results from a transfection ratio optimisation experiment conducted in H1975 cells. For the selection of the optimal ratio, the GFP signal was considered together with the toxicity of the procedure. The two parameters were monitored by flow cytometric analysis. As seen in the figure, a ratio of 3:2 (3µl FuGENE HD reagent to 2µg DNA) produced a high GFP signal without affecting the cell cycle profile, compared to an untransfected control sample. The more ruffled DNA histograms of the other samples indicate higher death rate following the transfection procedure. On these grounds, a ratio of 3:2 was selected as the optimal transfection ratio.

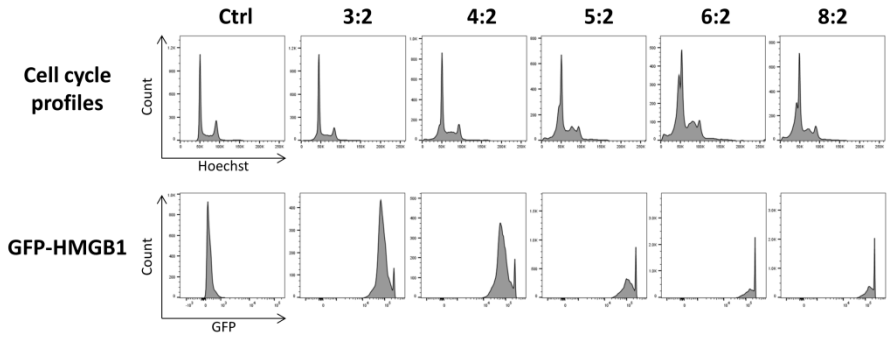

Figure 5.16. DNA and GFP histograms of H1975 cells in an untransfected control sample (Ctrl), and in samples transfected with different ratios of FuGENE HD reagent to plasmids. More ruffling of the DNA profiles indicates more death in the samples, as a result of the transfection toxicity. All the transfected samples show considerably higher GFP signals than the control sample.

5.3.2 Strategy for the HMGB1 assay

To make sure that every compared sample in the HMGB1 assay was transfected under the same conditions, one transfected cell sample was divided into samples for all the different treatments and a mock. It was also plated a non-transfected control sample for evaluation of transfection efficiency. As the assay was going to compare loss of GFP signalling (representing HMGB1) in treated samples compared to a mock sample, we found it propitious to barcode the treated samples and the comparative mock for accurate comparison. Consequently, the mock sample was barcoded with Pacific blue dye and divided to the different treated samples. A flow chart of the HMGB1 assay strategy is given in figure 5.17.

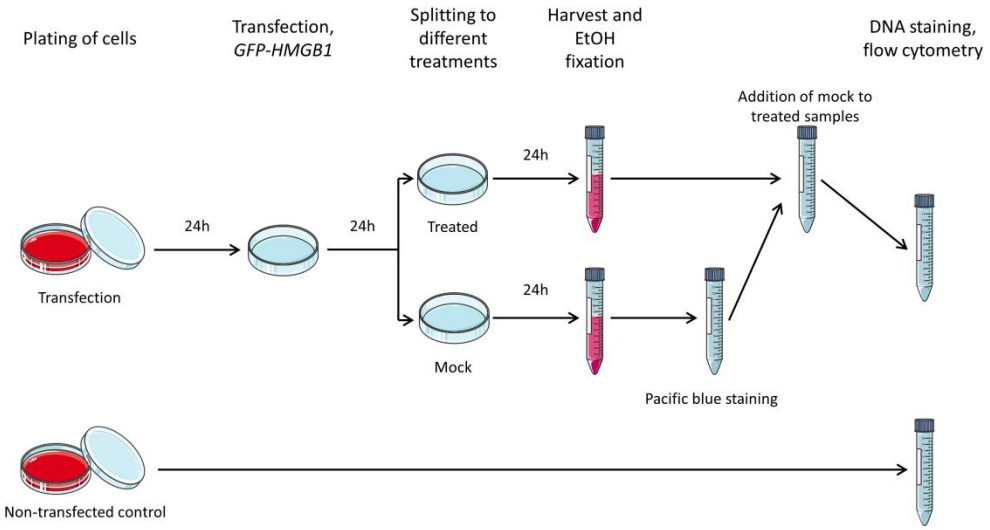

Figure 5.17. Work flow strategy for the HMGB1 assay. To begin with, two samples were plated; one for transfection and one as a transfection control. After 24 hours, the transfection sample was transfected with the plasmid vector containing *GFP-HMGB1*, and incubated for 24 hours. The sample was thereafter divided to different treatments. After 24 hours, the mock sample was barcoded with Pacific blue, and added to the treated samples, before DNA staining and flow cytometry.

5.3.3 Mitoxantrone as positive control for HMGB1 exodus

As MTX was found to be a suitable positive control for CRT translocation, this drug was also tested as a positive control in the HMGB1 assay. The results, depicted in figure 5.18, show that MTX gave a loss in intracellular GFP signal in both H1975 and U2OS cell lines, representing release of HMGB1 from the cells. MTX was therefore added as a positive control in the following assays.

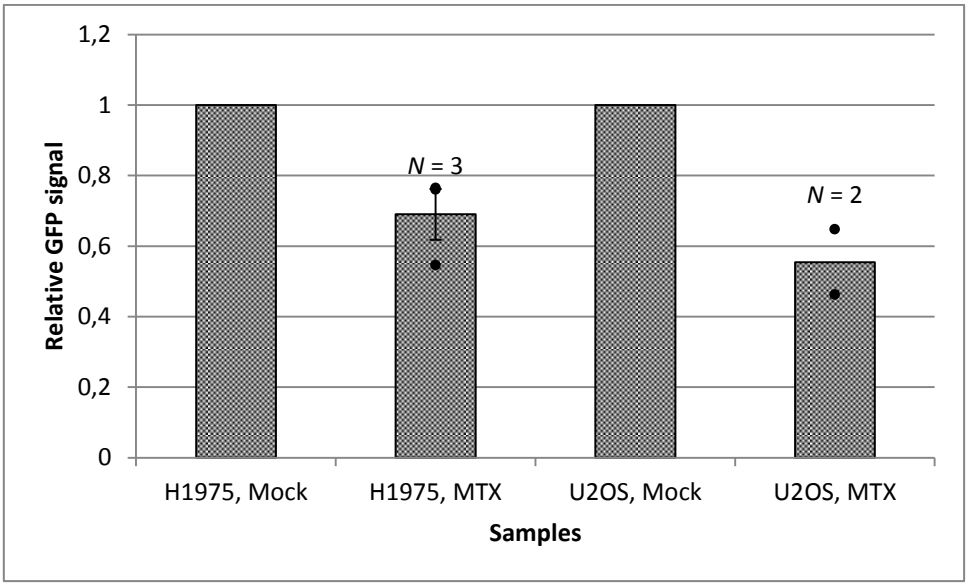

Figure 5.18. Results from experiments testing MTX (1µM, 24h) as a positive control for HMGB1 exodus. As seen, MTX gave loss of intracellular GFP signal (representing HMGB1) in both H1975 and U2OS cells, compared to mock. Dots represent the results from individual experiments. Error bar indicate SEM.

5.3.4 Optimised protocol for flow cytometry-based HMGB1 assay

1) Plate out two 6cm petri dishes with $5 \cdot 10^5$ cells in 3ml medium, one for transfection and one as control. Incubate the cells at 37°C for 24 hours.
2) Mix 2µg plasmids in 100µl pre-warmed OptiMEM in an Eppendorf tube, and add 3µl hand-warmed FuGENE HD transfection reagent. Make sure not to touch the plastic walls of the tube, in order to avoid disruption of the reagent. Tap the tube to mix the content, and leave at room temperature for 15 minutes.
3) Add the transfection mix to the transfection sample in a drop-wise manner. Shake the dish in two dimensions to distribute the transfection mix, and incubate the samples at 37°C for 24 hours.
4) Harvest the transfected sample, and split it to 35mm dishes according to preferred treatments, including a non-treated transfected mock sample. Split the non-transfected control sample at the same ratio, and transfer to a 35mm dish. Incubate the samples at 37°C for 24 hours.
5) Harvest all the samples, and fixate the cell pellets with -20°C 70% EtOH. Store the samples at -20°C for at least 1 hour.
6) Centrifuge the mock sample at 1500rpm for 5 minutes, and wash the pellet with 1X PBS. Centrifuge again, and resuspend the pellet in 200µl 1X PBS. Transfer 195µl of the suspension to a tube containing 5µl Pacific blue 1.25ng/µl in DMSO, and mix. Incubate in the dark for 30 minutes at room temperature. Add 5ml 1X PBS/1% FBS, and centrifuge at 1500rpm for 5 minutes. Resuspend in an appropriate volume of 1x PBS/1% FBS.
7) Centrifuge the remaining samples, and resuspend in 5ml 1X PBS/1% FBS. Divide the Pacific blue stained sample on the treated samples, and centrifuge at 1500rpm for 5 minutes. Resuspend the pellets in 500µl 1X PBS with 0.5µl FxCycle Far Red DNA stain and 5µl ribonuclease A (RNase A). Incubate the samples in the dark for 30 minutes at room temperature, and store at 4°C.
8) Analyse the samples by flow cytometry, with gating as shown in figure 5.19.

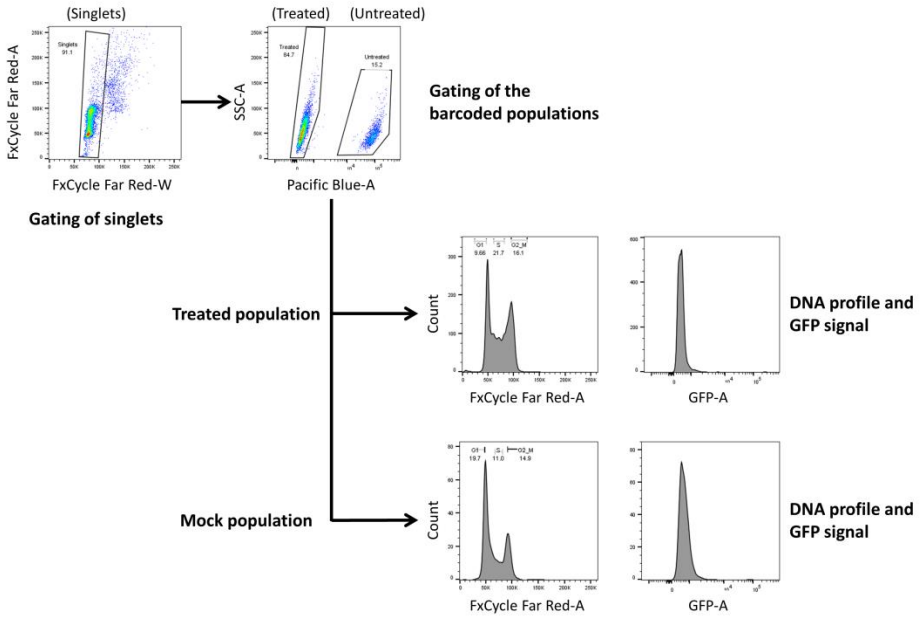

Figure 5.19. Figure showing the gating strategy of the flow cytometry analysis in the software FlowJo. The strategy is exemplified in an MTX treated U2OS sample. First, it was gated for single cells in an FxCycle Far Red-W *vs*. FxCycle Far Red-A dot plot, which enables the gating of cells with the same width signal for the DNA stain (cells to the right have increased width signals, indicating multiplets). Next, the treated and the mock population were gated for in a Pacific blue-A *vs*. SSC-A dot plot, in which the barcoded mock sample forms a population higher on the Pacific blue axis. From there, DNA profiles and GFP signals could be read.

5.4 Results from the calreticulin assay

5.4.1 Selection of ATR inhibitor concentrations

With the optimisation of the assays finalised, the study of IR combined with ATR inhibitors was initiated. An initial experiment was conducted in U2OS cells treated with 6Gy and the ATRi VE822 at concentrations of 25nM and 250nM. By studying the DNA histograms, it was clearly seen that both doses managed to abrogate the IR-induced G_2/M checkpoint arrest during a 24 hours' time span (data not shown). For the CRT assay in H1975 cells, it was determined to employ VE822 in doses of 50nM and 250nM. The ATRi AZD6738 was used in doses of 250nM and 1250nM, as these doses had previously been used in our group. Of note is that previous results from our group have shown that the IC_{50} values, as measured by cell viability at five days after treatment of U2OS cells with the ATR inhibitors alone, were

approx. 100nM and 1µM for VE822 and AZD6738, respectively (Rødland *et al*., unpublished results).

5.4.2 Ecto-CRT signalling at different time points following treatment with IR and ATRi

Previous studies of ecto-CRT signalling have been conducted at a 24 hour time point after treatment [128, 137, 170, 171]. At this time point, the ATR inhibitors would have led to abrogation of the G_2/M checkpoint. However, cell death following IR may initiate after several attempts of cell division, and it was therefore of interest to measure the ecto-CRT signals at later time points as well. Figure 5.20 shows the results of an experiment testing ecto-CRT signalling at 24, 48 and 72 hour time points. As clearly seen, the ecto-CRT signals were higher at both 48 and 72 hours after treatment, compared to 24 hours. It is also seen that the signal increased less in cells treated with IR and ATRi compared to the sample treated with IR alone, for all the time points.

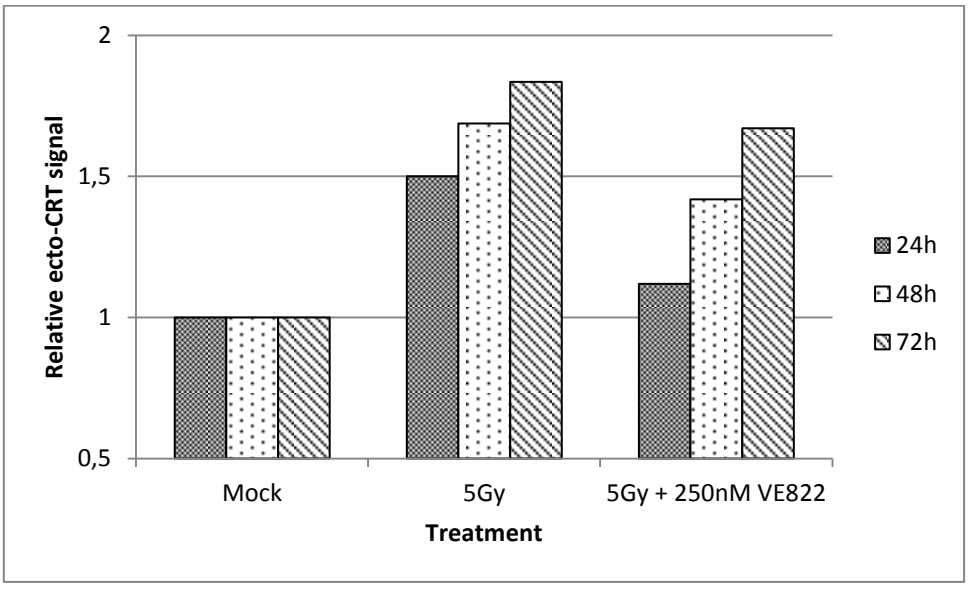

Figure 5.20. Relative ecto-CRT signals at 24, 48 and 72 hour time points for H1975 cells, after treatment with 5Gy and 5Gy combined with 250nM VE822. The values are relative to a mock sample. *n* = 2 for 24 and 48 hours, whilst *n* = 1 for 72 hours.

5.4.3 IR combined with different inhibitors of the G_2 checkpoint (ATR, CHK1, WEE1)

We next performed a set of experiments in H1975 cells at 24 and 72 hours after treatment with 5Gy irradiation combined with both ATR, CHK1 and WEE1 inhibitors. ATR was inhibited by VE822 (50nM and 250nM) and AZD6738 (250nM and 1250nM), WEE1 was inhibited with MK1775 (300nM, as previously used by our group) and CHK1 was inhibited by AZD7762 (100nM, as previously used by our group). The results are summarised in figure 5.21.

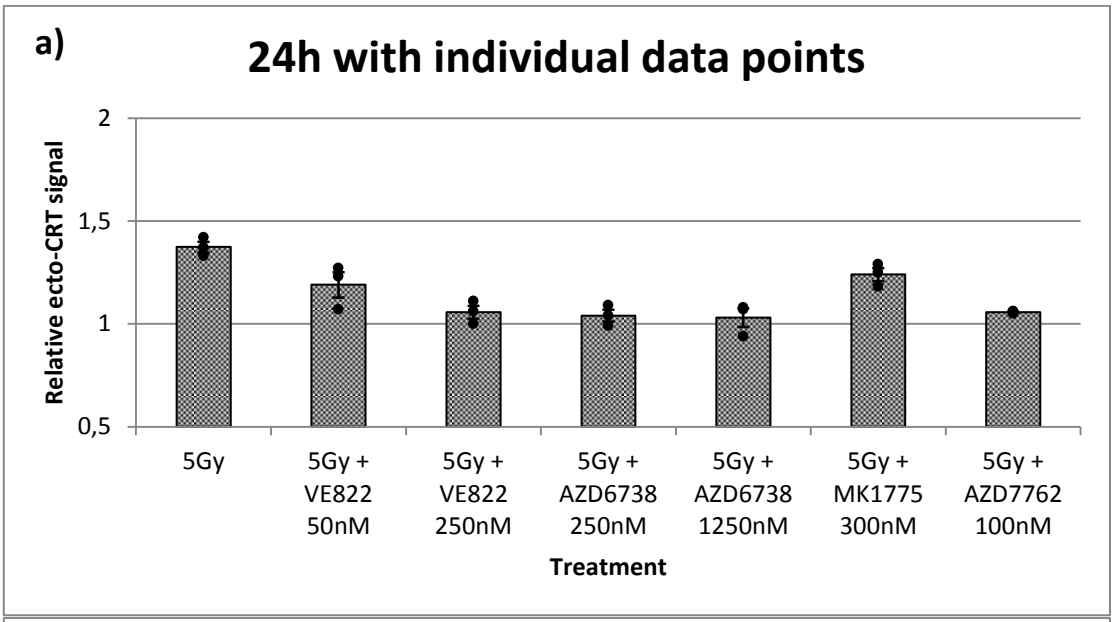
a)
24h with individual data points
Relative ecto-CRT signal
2
1,5
1
0,5
5Gy
5Gy + VE822 50nM
5Gy + VE822 250nM
5Gy + AZD6738 250nM
5Gy + AZD6738 1250nM
5Gy + MK1775 300nM
5Gy + AZD7762 100nM
Treatment

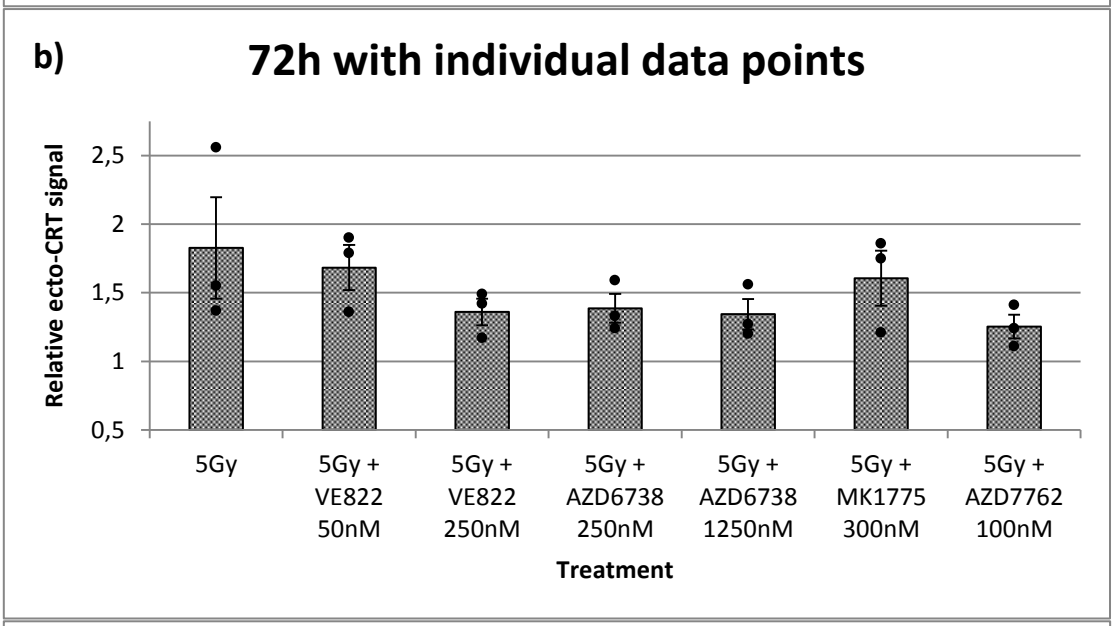
b)
72h with individual data points
Relative ecto-CRT signal
2,5
2
1,5
1
0,5
5Gy
5Gy + VE822 50nM
5Gy + VE822 250nM
5Gy + AZD6738 250nM
5Gy + AZD6738 1250nM
5Gy + MK1775 300nM
5Gy + AZD7762 100nM
Treatment

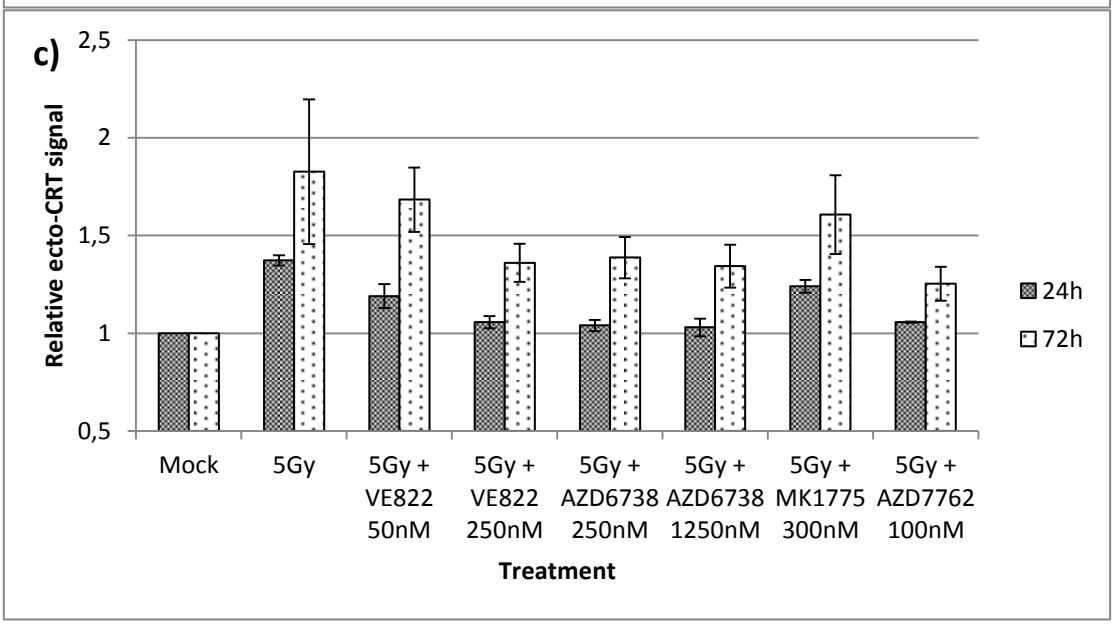
c)
Relative ecto-CRT signal
2,5
2
1,5
1
0,5
Mock
5Gy
5Gy + VE822 50nM
5Gy + VE822 250nM
5Gy + AZD6738 250nM
5Gy + AZD6738 1250nM
5Gy + MK1775 300nM
5Gy + AZD7762 100nM
Treatment
24h
72h

Figure 5.21. Results from experiments measuring ecto-CRT signalling in H1975 cells at 24 and 72 hours following treatment. The samples were treated with 5Gy alone, or in combination with ATR inhibitors (VE822, AZD6738), WEE1 inhibitor (MK1775) or CHK1 inhibitor (AZD7762). **a)** Figure showing the results for the 24 hour time point alone, with individual values for three independent experiments (relative to mock). **b)** Figure showing the results for the 72 hour time point alone, with individual values for three independent experiments (relative to mock). **c)** The figure summarises the mean ecto-CRT signalling values of the different samples at both 24 and 72 hours, relative to a mock sample. Dots indicate relative ecto-CRT values for individual experiments. Error bars indicate SEM. *n* = 3.

As seen in the figure, all the inhibitors decreased the ecto-CRT signalling compared to the sample treated with 5Gy irradiation alone. A similar pattern can be observed for both time points. Based on these experiments, it seems as if inhibition of kinases of the ATR–CHK1 pathway leads to diminished ecto-CRT signalling in H1975 cells.

5.4.4 Cell cycle effects of the CRT translocation

Next we considered whether the ecto-CRT signals may be related to cell cycle effects after radiation treatment, an aspect not seen previously enlightened in the literature. In these experiments, permeable Hoechst 33342 (6µg/ml sample) was used as a DNA stain rather than a barcoding stain. By staining the DNA in the samples, it was possible to gate for cells in the different cell cycle phases in the cell population. Thereby, the median ecto-CRT values for the different cell cycle phases could be read out. Also in these experiments, each sample was divided in a CRT sample and a secondary antibody control, and PI was used as live/dead stain (figure 5.22). Figure 5.23 shows how the gating based on a DNA histogram leads to discriminated cell cycle phases, as one expect a doubling of the genomic content in the cells in G_2 phase after DNA replication in S phase. The gates were placed very strict, in order to prevent inclusion of signals from the other phases. The cell cycle experiments were conducted on live cell samples after treatment with 5Gy and 5Gy with 250nM VE822.

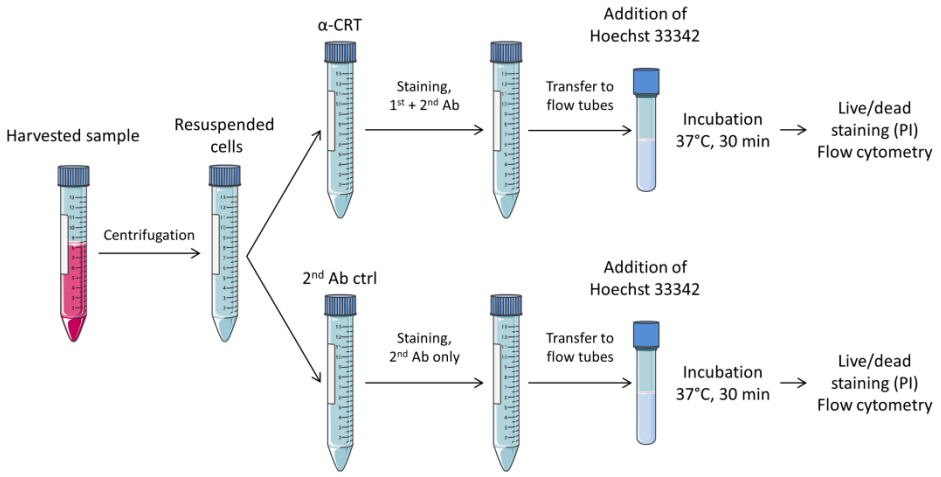

Figure 5.22. Figure depicting the work flow for staining of ecto-CRT in the cell cycle experiments. Each harvested sample was split to yield a sample for ecto-CRT staining (α-CRT) and a secondary antibody control (2^{nd} Ab ctrl). After transfer of stained samples into flow tubes, the samples were added permeable Hoechst 33342 (6µg/ml sample), and incubated at 37°C for 30 minutes. As a live/dead stain, propidium iodide (PI) was added two minutes prior to flow cytometry.

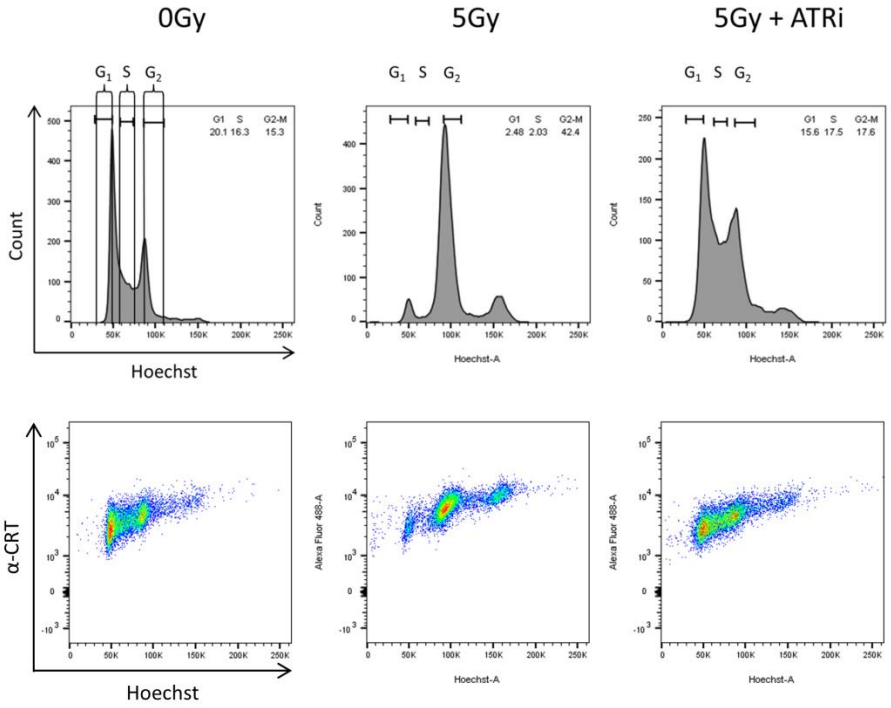

Figure 5.23. Figure showing how to gate for the different cell cycle phases in an untreated H1975 sample (0Gy), a H1975 sample treated with 5Gy (5Gy) and a H1975 sample co-treated with 5Gy and 250nM VE822 (5Gy + ATRi). The figure is a representative example on how the cell cycle phase gating was conducted. Note how cells arrest in G_2/M phase when treated with 5Gy (as the G_2/M checkpoint is activated) and how this checkpoint is abrogated in the sample given ATR inhibitor prior to irradiation. The lower row shows ecto-CRT (Alexa Fluor 488-A) *vs.* Hoechst 33342-A dotplots.

The cell cycle experiments almost exclusively revealed increased ecto-CRT signals in S and further increased signals in G_2 phases, relative to the signal in G_1 phase. In the cell cycle, all the cell components are amplified so that each daughter cell contains the same amount of components as the mother cell had before cell division. Therefore, the volume of a G_2 cell will be the double of that of a G_1 cell. This fact raises the question of whether the increased ecto-CRT signalling in the later phases only reflects increased unspecific antibody binding to the cell surface area as the volume increases. If one presumes that the cells are perfect spheres, the surface area of a G_2 cell with double the volume of a G_1 cell, would be $\sqrt[3]{2^2}$, or approximately 1.59, times bigger than the surface area of the G_1 cell (for calculation, see appendix).

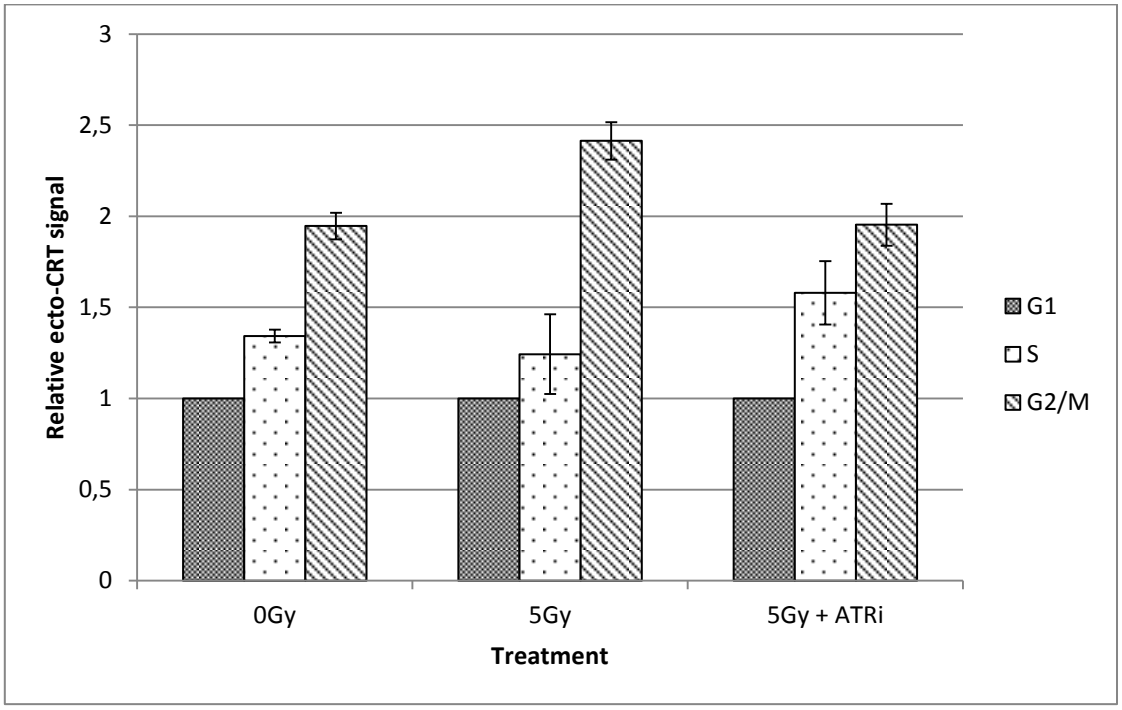

Figure 5.24. Results from the cell cycle experiments, showing increase in ecto-CRT signals for the different cell cycle phases relative to the signals in G_1 phase. H1975 cell samples were treated with 5Gy alone, or 5Gy combined with 250nM VE822 (ATRi), and the ecto-CRT signalling was measured at 24 hours after treatment. Error bars indicate SEM. *n* = 3.

As seen in figure 5.24, depicting the results from cell cycle effect experiments, the ecto-CRT signals for the two treatments were above the level of increase one can expect from a mere increase in cell volume from G_1 to G_2 after 24 hours. This may indicate the presence of a cell cycle effect, in which S and G_2 cells translocate more CRT than the G_1 cells. Interestingly, the

highest signal increase after irradiation is seen in G_2/M phase. This increase was reversed by the ATRi.

5.5 Results from the ATP assay

5.5.1 ATP secretion at 24 hours after treatment

The optimised ATP assay was performed on samples treated with 5Gy irradiation with and without 250nM VE822 or AZD6738. The samples were plated as triplicates. The results, shown in figure 5.25, show a two-fold increase in secreted ATP in samples treated with 5Gy alone, compared to the mock sample. In the VE822 co-treated samples, the ATP signal was reduced by nearly 50 per cent, whereas the sample co-treated with AZD6738 had almost the same relative luminescence as the sample treated with irradiation alone.

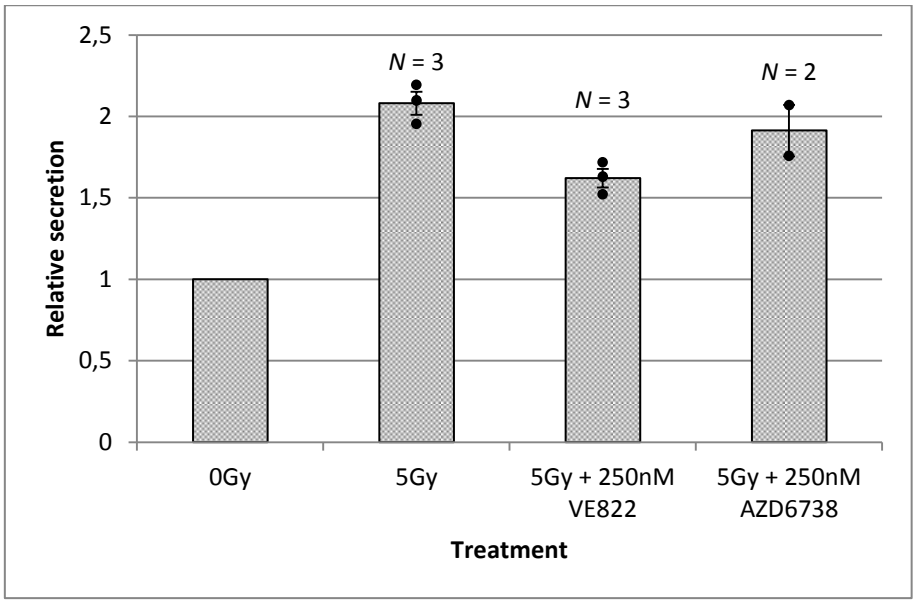

Figure 5.25. Results from the ATP assay at 24 hours after treatment of H1975 cells. The signals are relative to the mock sample (0Gy). As seen in the figure, treatment with 5Gy alone gave approximately a two-fold increase in ATP secretion, based on luminescence detection. When co-treated with the ATR inhibitors VE822 and AZD6738, irradiated samples showed decreased ATP signalling. Each experiment was done in triplicates, with dots representing the average of constituent triplicates. Error bars indicate SEM.

5.5.2 ATP secretion at 48 hours after treatment

With ATR inhibition rendering the samples with a lesser secretion of ATP after 24 hours, the assay was performed after 48 hours to see whether this time point gave altered results. Once again, mock samples and samples treated with 5Gy irradiation with or without ATR inhibitors (VE822 250nM; AZD6738 250nM) were plated in triplicates. The results presented in figure 5.26 show approximately three-fold increase in ATP signalling for the sample treated with irradiation alone compared to the mock, whereas the ATP signalling dramatically increased further for the co-treated samples. The VE822 treated sample shows an eleven-fold increase in ATP secretion, whereas the AZD6738 treated sample shows a six-fold increase.

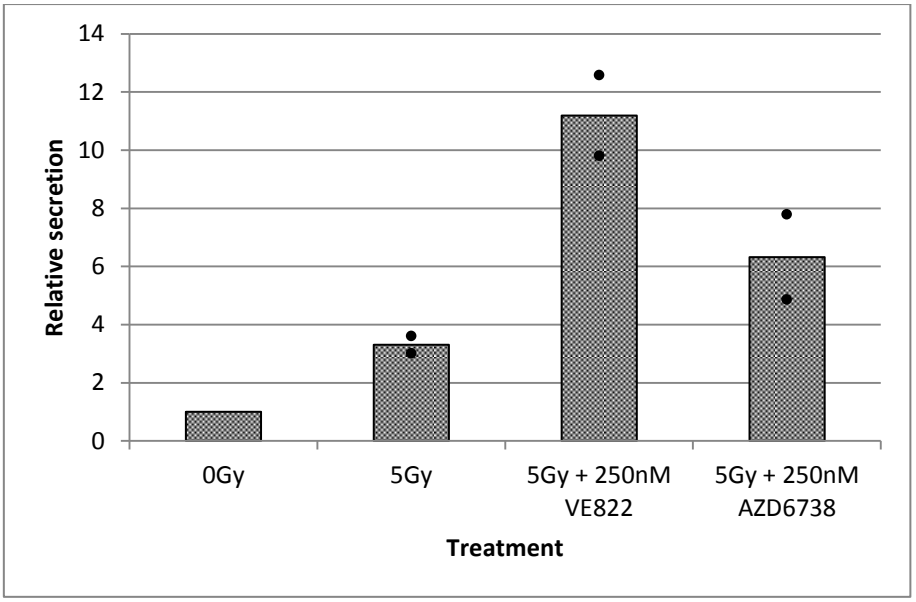

Figure 5.26. Results from the ATP assay measured at 48 hours after treatment of H1975 cells. As seen, the ATP signalling from samples exposed to co-treatment of irradiation with ATR inhibitors (VE822, AZD6738) dramatically increased at this time point, compared both to the sample treated with irradiation alone, and the mock (0Gy). Dots indicate results from individual experiments, each representing the average of constituent triplicates. *n* = 2.

A 48 hours' time point is long enough for the cells to divide to uneven population numbers depending on the different treatments. If the cell population of each sample varies, this may impinge upon the ATP signalling read out of each sample, as the concentrations of cells – and thus secreted ATP – could differ significantly. Therefore, the cell numbers of one dish representing each of the treatments were counted on a Coulter counter. The count showed

variance in cell numbers, but if normalised the assay result would show the same tendency. The results from the cell count are given in table 5.3.

Table 5.3. Table showing the cell count of a representative sample for each of the different treatments after 48 hours, together with their relative luminescence values (RLU) from the *CellTiter-Glo* procedure. In addition, the table shows the RLU values normalised to the cell numbers of each sample. One sample representing each treatment was harvested, and the cell concentration was counted in a Coulter counter in order to assess the total cell number of the sample.

Sample:	Total number of cells:	RLU:	RLU relative to cell numbers (approx.):
0Gy	$3.388 \cdot 10^6$	10696	3157
5Gy	$1.532 \cdot 10^6$	27262	17795
5Gy + 250nM VE822	$1.946 \cdot 10^6$	109130	56079
5Gy + 250nM AZD6738	$2.564 \cdot 10^6$	63218	24656

5.6 Results with the HMGB1 assay after treatment with radiation and ATR inhibitors

To assay HMGB1 exodus after treatment with radiation and the two ATR inhibitors, experiments were performed with U2OS and H1975 cells as outlined in figures 5.17 and 5.19. In both cell lines, the results indicated less HMGB1 secretion at 24 hours after treatment with 5Gy compared to non-irradiated samples. Co-treatment with ATR inhibitors decreased the GFP signal, indicating more HMGB1 exodus than after treatment with 5Gy alone (figure 5.27). In every experiment, samples treated with MTX were included as positive control. Unexpectedly, the results with MTX were negative in these experiments, starkly contrasting the previous experiments shown in figure 5.18. The reason for the sudden change in results for the MTX treated samples remains unclear, and the variable MTX results therefore suggest that additional measurements of HMGB1 exodus will be needed in order to draw solid conclusions for this assay.

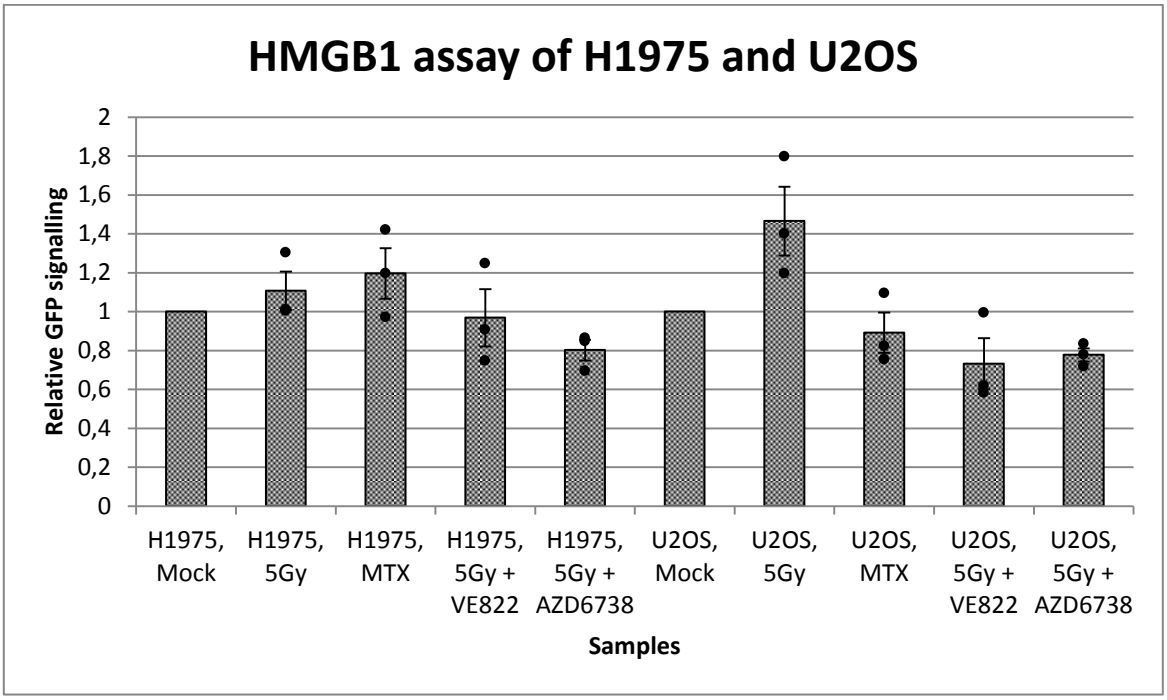

Figure 5.27. Preliminary comparison of the total GFP median values for different samples as means of analysing HMGB1 exodus as response to different treatments. The samples were treated with 5Gy irradiation alone, MTX 1µM or 5Gy irradiation combined with 250nM VE822 or AZD6738. All values are relative to a mock sample. Dots represent results from individual experiments. Error bars indicate SEM. *n* = 3.

5.7 Western blotting of pSTAT1

As two recent landmark publications showed how cells forming micronuclei in the aftermath of irradiation produce innate immune responses through detection of cytosolic dsDNA [162, 163], we started investigating this phenomenon. As described in the articles, phosphorylated STAT1 (pSTAT1) is a good indicator of the interferon response produced by detection of dsDNA in the cytosol. To validate the generation of micronuclei following radiation, an experiment was conducted on U2OS cells. The results from this experiment are shown in figure 5.28, and clearly show how micronuclei are formed three and six days after 20Gy irradiation. Experiments with Western blotting of irradiated samples after three and six days were thereafter conducted in U2OS, and later on also in H1975 cells.

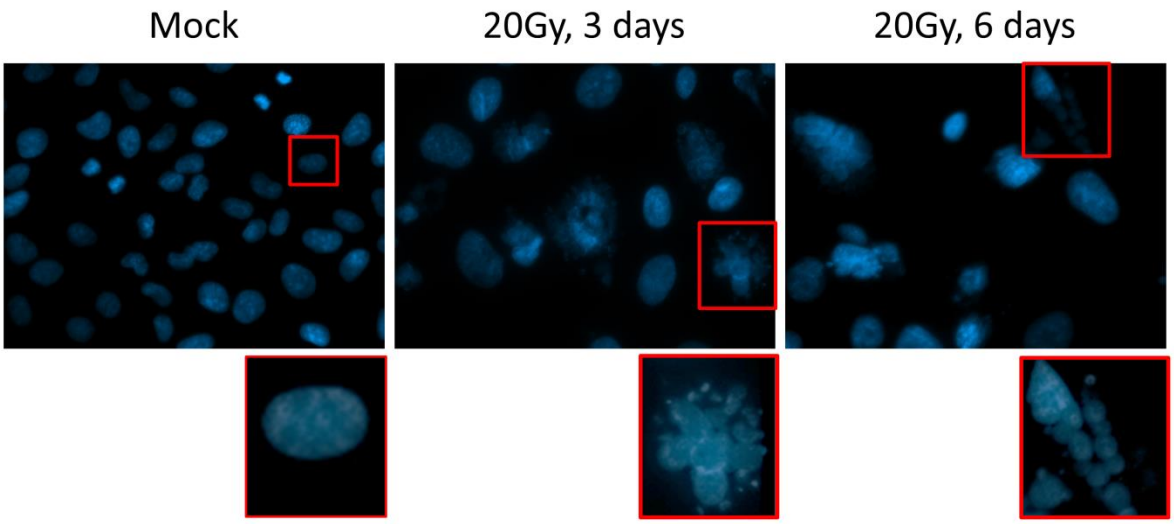

Figure 5.28. Micrographs showing the formation of micronuclei in U2OS cells at three and six days after irradiation with 20Gy, compared to a mock sample. The cell nuclei were stained with Hoechst 33342. Lower micrographs show magnified excerpts from the upper full-scale micrographs. Please note that contrast and brightness have been manipulated in the lower micrographs.

We initially tested two different antibodies against pSTAT1 (*Santa Cruz* sc-464, 1:200; *Cell Signaling* 58D6, 1:1000) for Western blotting. The latter antibody was used by the group behind one of the aforementioned publications [162]. As this antibody gave stronger signals in these tests (data not shown), it was chosen for further investigations.

Different time points for pSTAT1 detection was tested out, and highest response was seen after six days for U2OS and two to three days for H1975, as depicted in figure 5.29 and 5.30. Several Western blot experiments were executed with U2OS and H1975 cells six and three days after treatment, respectively, and a trend of increased pSTAT1 and STAT1 signalling at the chosen time points were observed. U2OS cells treated with 20Gy showed increased pSTAT1 and STAT1 signals after six days, in compliance with the published work [162]. For U2OS, the increase in signalling was observed in three out of four experiments. A representative blot is shown in figure 5.29a, along with its quantification relative to the CDK1 signals given in figure 5.29b. In the deviant fourth experiment, samples were irradiated with 5, 10 and 20Gy and harvested six days after treatment. This experiment showed increased pSTAT1 and STAT1 levels for the sample treated with 5Gy and 10Gy, but not for the one treated with 20Gy (data not shown). Therefore, additional experiments are required for further validation of the pSTAT1 response in the U2OS cell line. Worth mentioning is that

a single, preliminary experiment testing pSTAT1 and STAT1 signalling after 20Gy irradiation combined with 250nM VE822 showed decreased levels of pSTAT1, as seen in figures 5.29c-d.

The H1975 cell line showed increased pSTAT1 and STAT1 signalling two to three days after treatment, as shown in figure 5.30. In this cell line, increased signalling was observed with 5, 10 and 20Gy, with a slight decrease in signalling for pSTAT1 in the 20Gy sample, as given in the quantification shown in figure 5.30d. The time course results for H1975 shown in figure 5.30a-b are representative for three independent experiments.

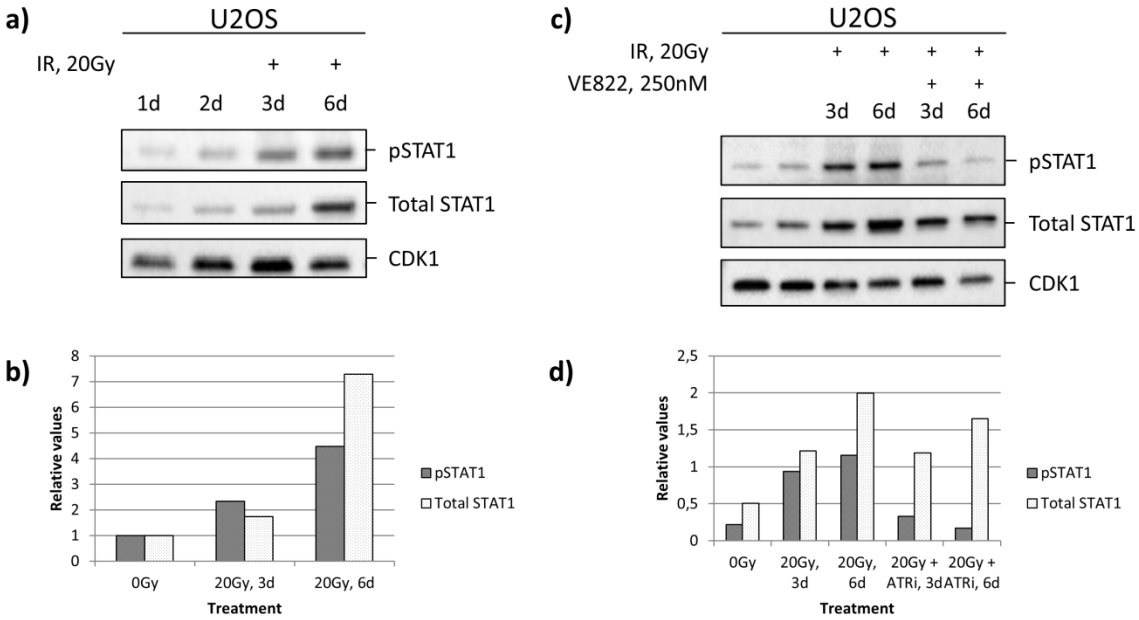

Figure 5.29. Preliminary results from Western blotting of pSTAT1 and STAT1 in U2OS cells, as means to evaluate interferon response following radiation. **a)** Time course response in U2OS cells after treatment with 20Gy, blotted after three and six days (3d, 6d). CDK1 is used as loading control. **b)** Quantification of the Western blot given in figure a. The values are normalised to the CDK1 levels. **c)** Western blot of pSTAT1 and STAT1 in U2OS cells after three and six days (3d, 6d). The cells were treated with 20Gy irradiation alone, or in combination with 250nM VE822. CDK1 is used as loading control. **d)** Quantification of the Western blot given in figure c. The values are normalised to the CDK1 levels.

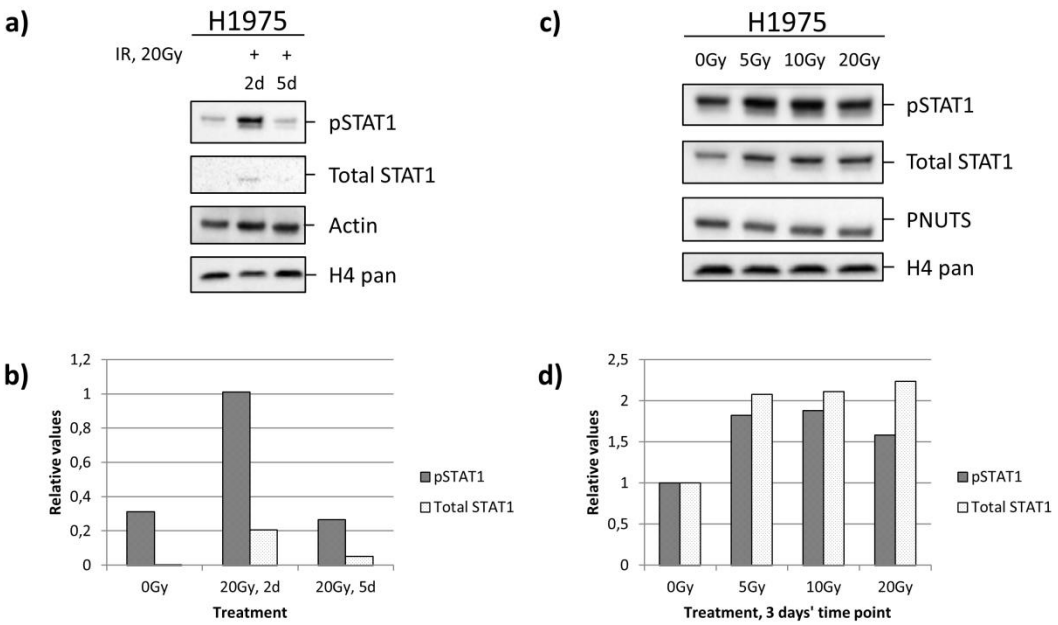

Figure 5.30. Preliminary results from Western blotting of pSTAT1 and STAT1 in H1975 cells, as means to evaluate interferon response following irradiation. **a)** Time course response in H1975 cells treated with 20Gy irradiation, blotted for after two and five days (2d, 5d). Actin and H4 pan are used as loading controls. **b)** Quantification of the Western blot given in figure a. The values are normalised to the actin levels. **c)** Dose response in H1975 cells after three days, with respect to pSTAT1 and STAT1 levels. The cells were treated with doses of 0, 5, 10 and 20Gy. PNUTS and H4 pan are used as loading controls. **d)** Quantification of the Western blot given in figure c. The values were normalised to the H4 pan levels.

6 Discussion

6.1 General discussion

In this Master's thesis, *in vitro* detection methods for three hallmark factors of immunogenic cell death (ICD) were optimised. Subsequently, these methods were used to examine the effects of ATR inhibition in combination with radiation on ICD. In addition, interferon signalling events after radiation were examined by Western blotting of pSTAT1.

6.1.1 Assays for detection of immunogenic cell death

To detect surface presented CRT, we used flow cytometry. Flow cytometry is a very reliable detection technique able to detect parameters at a single-cell level, and an elegant way of detecting surface markers. Detection by the flow cytometry method has previously been used in other studies [123, 129, 133, 137, 170]. However, there is no well-established method for ecto-CRT detection, and we may find some of the previous studies to have issues with uncertain discrimination of live and dead cells. Therefore, we started our study without having a ready-made protocol for measurements. Hence, several control experiments and optimisations were needed for us to make a reliable protocol for measuring ecto-CRT. We included barcoding, which we have not seen in any of the previous publications measuring ecto-CRT. Thus, we find this aspect of our method rather unique, likely enabling more accurate results than seen in the previous studies. Besides inclusion of barcoding, some of the most critical points in our protocol are the use of live cell staining and the selection for viable cells upon detection. Staining of live cells restricts antibody affinity to ecto-CRT alone, as the intact plasma membrane of live cells is a barrier for staining of redundant, intracellular CRT (endo-CRT). Selection for viable cells was conducted by gating for cells that did not take up the stains Hoechst 33258 or propidium iodide. Dying cells will, during the time span of the death modality, get ruptured membranes, and therefore no longer have intact barriers against staining of endo-CRT. Hence, inclusion of dead cells in the assay would lead to false-positive results, as demonstrated in figure 5.2.

In order to measure secreted ATP, we employed the *CellTiter-Glo* ATP detection kit from Promega. This kit is primarily intended for measurement of cell sample viability, as its use of a lysing agent releases ATP from the cells. Measurement of this ATP will therefore correlate with the cell viability in the sample. Due to the fact that the kit lyses cells, we had to include some additional steps in order to make sure that we only measured extracellular ATP. A two-step centrifugation was used to exclude floating cells that could give unspecific ATP signals in the collected growth media (figure 5.11), and use of serum-free medium was considered essential (figure 5.13). Furthermore, a standard curve of ATP was included, in order to confirm that our measurements were within the linear range of detection (figure 5.14). Other ATP detection kits are commercially available, and these might be more sensitive than the kit used in this study. It may therefore be of interest to explore other kits in future experiments.

HMGB1 exodus can be measured either by assessing secreted HMGB1 directly or by measuring residual intracellular HMGB1, for instance by use of ELISA kits or fluorescence microscopy, respectively. Previous studies on HMGB1 exodus have been conducted with both of these approaches [129, 170, 177, 178]. As mentioned in section 5.3, we chose to measure residual intracellular HMGB1 by use of flow cytometry in our prefatory experiments. Our approach is thus similar to the previous studies measuring residual intracellular HMGB1 by fluorescence microscopy, except that we used flow cytometry. In order to detect HMGB1, we chose to transfect cells with a *gfp*-tagged *HMGB1* gene, a strategy used in a previous study [178]. After the transfection was optimised and performed, HMGB1 exodus was calculated from GFP median values after different treatments. In order to get reliable results, we included a positive control for secretion of HMGB1, and barcoding to minimise sample-to-sample variations. MTX, which to begin with was shown useful as a positive control (figure 5.18), was later revealed to be unreliable (figure 5.27), and we therefore lacked a positive control for the evaluation of our results. For the barcoding, an untreated, transfected mock sample was portioned out to the different treated sample (figure 5.17). This sample was plated with the same amount of cells that was seeded for the other samples. It later turned out that this number was not enough for achieving statistically satisfying mock population in the treated samples, as many cells easily are lost during

staining. We should therefore have seeded out more cells for the mock sample in our protocol.

We failed to produce stable transfectants expressing *GFP-HMGB1*, as the transfected cells lost their GFP signals after two to three weeks. In the plasmid vector used for the transfection, the *GFP-HMGB1* gene was under control of the human cytomegalovirus (hCMV) promoter, which previously has been associated with loss of GFP signals. The hCMV promoter has been reported to be subject to methylation in stable transfectants, thereby leading to loss of expression of the transfected genes [180, 181]. In order to achieve stably *GFP-HMGB1* overexpressing cells, it may therefore be of interest to perform transfections with a plasmid vector containing a more sustainable promoter than CMV. This is in opposition to previously published protocols, in which a vector containing pCMV was used for the generation of stable transfectants [178]. The use of stable transfections may produce more even expression between the cells; thereby engender more easily comparative GFP signals. However, ELISA detection is a major possibility for future measurements. The ELISA detection method is highly sensitive and specific, but at the same time relatively expensive, which led us to use the cheaper alternative of flow cytometry for the prefatory experiments. Future experiments may be executed by use of the ELISA method, which enables direct detection of HMGB1 without the need of a GFP reporter.

As mentioned, we performed the CRT and ATP assays on live cells, whereas the HMGB1 assay was conducted on fixated cells. In an *in vivo* scenario, secreted ATP and HMGB1 are present as free molecules in the extracellular fluid, and are therefore not dependent on the cell they are secreted from. In other words, the viability of the cells would likely not impact on the DAMP function of ATP and HMGB1 after release. Anyways, secreted ATP was detected from live cells in this study, as we wanted to detect increased signalling, and thus found it propitious to measure secretion from live cells rather than dead. Yet, this does not undermine the potential of ATP from dead cells as a DAMP. Contrasting the two aforementioned ICD markers, ecto-CRT is bound to the plasma membrane of its cell. Only ecto-CRT, and not free CRT in the extracellular fluid, is regarded a hallmark of ICD [129, 137]. This means that CRT released from dead cells falling apart cannot be detected as an indicator of ICD. It is therefore tempting to speculate that the DAMP function of CRT is in

some way coupled to recognition of the cell on which it is presented, for instance through co-stimulatory reactions or proximity-dependent signalling.

6.1.2 Comparison with measurements of ICD after radiation and MTX treatment *in vitro* in earlier literature

As indicated in figures 5.20 and 5.21, an approximate half-fold increase in ecto-CRT signalling was achieved 24 hour after treatment of cell samples with 5Gy irradiation alone. This increase corresponds with a previously report, showing between 50 and 75 per cent increase [122]. Also for the ATP secretion and HMGB1 exodus, approx. 50-75 per cent increase in signalling has been reported when irradiated with 5Gy [122]. In addition, it has been reported no increase in ATP secretion with 10Gy irradiation, and varying HMGB1 exodus depending on cell lines [123]. As shown in figures 5.25 and 5.26, we obtained one- and 1.5-fold increases in ATP secretion at 24 and 48 hours, respectively. At the same time, irradiation with 5Gy gave no HMGB1 exodus, as presented in figure 5.27. When comparing the results with previous publications, it therefore seems as if our results are located in a reasonably range of expectance.

As mentioned earlier, MTX has been used as an ICD inducer in several earlier publications. Although some publications show higher ecto-CRT signalling with MTX than we achieved [137, 170], others indicate an increase more similar to our findings, with approx. 50 per cent increase in the ecto-CRT signal [130]. MTX has also previously been used as an inducer of ATP secretion and HMGB1 exodus, in which MTX treated samples have shown two to three (and sometimes as much as six) times more secreted ATP and HMGB1 than the control [123, 173, 174, 178]. We did not get any response with MTX in the ATP assay, but the use of MTX initially exerted a small effect on the HMGB1 exodus in both U2OS and H1975 cells (figure 5.18), although not to the degree reported.

6.1.3 Effects of ATR inhibitors and radiation on immunogenic cell death

To assess the role of ATR inhibition, we treated cells *in vitro* with IR in combination with different concentrations of two ATR inhibitors presently being tested in clinical trials. The

study showed that ATR inhibition did not increase the IR-induced translocation of CRT to the cell surface, but that ATP secretion increased at a 48 hours' time point. Moreover, the ATR inhibitors induced HMGB1 exodus after IR. As the contemporaneous presence of all of the three ICD markers are established as a necessity for the induction of an effective ICD response, our results are not conclusive towards a potential clinical effect of co-therapy with ATRi and irradiation at this stage. Nevertheless, ATR inhibition gave positive results for two of the endpoints, which could increase the possibilities of an ICD effect in the greater picture, as our results show that irradiation alone contributes to ecto-CRT signalling. Further experiments in different cancer cell lines and in *in vivo* models may reveal additional basis for increased ICD signalling after the co-treatment.

In addition, we have found increased pSTAT1 signalling in the aftermath of irradiation, as earlier reported by another group [162]. The increased signalling is thought to represent interferon responses induced by DNA in formed micronuclei (see section 1.6.4 and figure 1.11). An increase in interferon signalling may lead to innate immune responses and phagocytic death. Effects of ATR inhibition on these findings remains to be fully investigated, but it is likely that ATR inhibition may impinge on the signalling, as this inhibition may lead to the formation of more micronuclei. We performed a single experiment with ATR inhibition, and preliminary results from the experiment showed less pSTAT signal after the co-treatment with ATRi (figure 5.29c-d).

The two ATR inhibitors used in this project are presently in clinical trials, albeit merely for their roles in inhibition of DNA repair and increased cancer cell death. However, we tested for immune stimulatory effects of ATRi through induction of ICD. Although the effects were only observed in two of the three endpoints, we find that the ATR inhibitors may contribute to increased signalling, as discussed above.

In addition to the hypothesised increase in ICD signalling by cell cycle checkpoint abrogation, it has recently been published that cancer cells upregulate the level of PD-L1 in an ATR pathway dependent manner in occurrence of DSBs [182]. Upregulation of PD-L1 will increase T-cell suppressive signalling through PD-1 receptors on the T-cells. On these grounds, ATR inhibition as co-treatment with radiation may also promote T-cell responses towards tumour cells in general; as such inhibition would prevent the PD-L1 upregulation.

6.1.4 Cell cycle effects on CRT translocation and HMGB1 exodus

To our knowledge, cell cycle effects of ICD marker presentation have never been assessed in previous literature. Because we have studied ICD effects in samples treated with radiation, we considered it desirable to investigate this aspect, as radiation has major impact on population-wise cell cycle phase distribution. We found possible cell cycle effects in the CRT assay (figure 5.24), in which cells in G_2 phase appeared to have increased ecto-CRT signals. 24 hours after radiation, this ecto-CRT signalling for cells in G_2 phase was even higher. As described in section 5.4.4, this heightened signalling was above what to expect with just the extended surface area resulting from a natural increase in volume. How radiation may give rise to more translocation of CRT in G_2 phase remains to be explored. A speculative possibility is that G_2 cells are (for unknown reasons) more susceptible for ER stress, thereby leading to more stress-related signalling, including CRT translocation.

ATR inhibition results in the abrogation of the G_2/M cell cycle checkpoint. Therefore, cells that would normally be arrested after IR continue their cell cycle. On the cell population level, this would result in a phase distribution more similar to that of non-treated cells. Cells treated with irradiation, on the other hand, would be arrested in the aforementioned checkpoint, and the population would pile up in G_2 phase. If the ecto-CRT signalling is expressed in a higher degree in G_2 cells, the ATR inhibition will therefore be restrictive to the signalling, as it results in normal amounts of G_2 cells in the population. In this way, inhibition of ATR may suppress the ecto-CRT signalling of irradiated cells, hence diminishing possible ICD effects.

We also considered the presence of cell cycle effects in the HMGB1 assay. An increased signalling from cells in G_2/M phase was constantly observed in the results, both for the H1975 and the U2OS cell line (data not shown). Further HMGB1 assay experiments, with a functional positive control in place, may give substantial evidence for such a cell cycle effect. If this should occur, future flow cytometric analyses of HMGB1 exodus have to be executed with respect to cell cycle phases. Also in this case, the necessary phase individualisation will then be due to the fact that irradiation shifts the phase distribution in the samples. To avoid such issues in the detection, one might focus on direct measurement of secreted HMGB1

(for instance by ELISA), as this would detect the actual quantity of HMGB1 exodus, rather than the residual intracellular HMGB1.

6.1.5 Effects of radiation on the tumour microenvironment

In this project, co-treatment of ATRi and IR has been used for the study of ICD in cancer cells cultured *in vitro*. The hypothesised goal is that this treatment may lead to a primed T-cell response towards tumour cells, through increased ICD. In addition, there are also other immune stimulatory effects of such treatment. One of the hallmarks of cancers is the avoidance of the immune system (reviewed in [112]). This is partly caused by down-regulation of Major histocompability complexs (MHC), *e.g.* MHC class I, in order to avoid contact with $CD8^+$ T-cells. Radiation will, on the other hand, activate the mTOR signalling pathway in the irradiated cancer cells, leading to increased transcription and antigen presentation (reviewed in [183]).

Yet, radiation therapy in live models may have a drawback side as well as a therapeutic. It has been shown that radiotherapy may promote immune suppressive actions in the tumour microenvironment, thereby appearing as a double-edged sword in cancer treatment. By recruiting regulatory T-cells (T_{reg}) and TGF-β and IL-10 producing myeloid cells to the microenvironment, radiation may contribute to inhibition of $CD8^+$ T-cells. In addition, these cells may produce other compounds and reactive molecule species that deprive T-cell function. Also the function of APCs (*e.g.* dendritic cells) and the action of cross-priming may be distorted by radiation (reviewed in [124]).

Therefore, as there are several immunomodulatory aspects of *in vivo* radiation therapy, radiation experiments *in vitro* do not present a complete picture. The complexity of a complete live model immune system must therefore always be borne in mind when analysing the *in vitro* data.

6.1.6 Future possibilities

In future perspectives, it will be necessary to conduct experiments in various cell lines to look for conserved effects across different cell lines and cancer types. With additional

positive results in future *in vitro* experiments, it may also be required to investigate effects *in vivo* in live mouse models.

To further evaluate possible effects of co-treatment with ATRi and radiation, it may be propitious to assay ICD signalling from some of the lesser established ICD markers as well, for instance the heat shock proteins HSP70 and HSP90. As the HSPs are presented on the cell surface in a similar manner as ecto-CRT, it is assumed that the same protocol can be used for assaying these markers as the one used for the CRT assay.

With the possible effect of ATR inhibition on PD-L1 expression [182], measurements of PD-L1 presentation on co-treated cells may also be of interest in further studies, as well as assaying the other immune checkpoint receptor, CTLA-4. With the optimised protocol for live cell staining, such measurements should be relatively straightforward to perform.

6.1.7 Clinical significance of the results

Our results indicate that ATR inhibition may lead to increased ICD signalling when combined with irradiation *in vitro*, and future studies will further elaborate this effect. If so, this may give a deeper insight to therapeutic possibility of radiotherapy. ATR inhibitors may increase the efficiency of the radiotherapy, as the ICD-induced systemic immune response after local radiation treatment leads to abscopal effects on distal tumours and metastases.

The two ATR inhibitors VE822 and AZD6738 are currently in clinical trials, and might be approved for clinical application in near future. With a deeper understanding of the possibilities of ATR inhibition, as our research may provide, clinical use of the two drugs can be fully profited. In addition, it may contribute to an evaluation of possible immunotherapy with immune checkpoint inhibitors subsequent to co-treatment of IR and ATRi.

6.2 Experimental considerations

6.2.1 Cell culturing

In this *in vitro* project, the experiments have been conducted in human-derived cancer cells grown in standard cell cultures. The use of human cancer cells has made the project more

transmittable to cancer therapy, yet with a minimum of ethical concern. The cell lines used for this project were already available in our research group, and therefore used as candidate cell lines. We chose to begin our experiments in U2OS cells, as this cell line is an easily cultured cell line routinely used by the group. In addition, this cell line has been seen used by other groups investigating ICD [172-174, 178]. Most experiments were conducted in H1975 cells, for reasons discussed in sections 5.1.4 and 5.2.2. H1975 cells are also routinely used by our group.

Even though cultured cells stand as a foundation to most present-day cell biological and medical research, cultured cells do not fully reflect the cells inside a living organism. Firstly, culturing is executed by growing the cells in a monolayer with artificial nourishing and optimised growth environments. With the exception of A549, the used cell lines are unable to grow in three dimensions in culture, which would more closely resemble tumour tissues. Secondly, most cell lines are immortalised for the use in laboratories. The process of immortalisation (in which cells are naturally or artificially mutated to avoid senescence) and the long-term passaging in cultures often leads to genetic alterations and somewhat new phenotypes in the cells. This results in cell lines that to some degree deviate from patient-hosted cancers. Therefore, live model experiments will be necessary for a profound understanding of the subject investigated.

In our study, we used cultured cells for cancer immunology research. Although it is impossible to study full immune responses in cultured cells, the use of *in vitro* experiments allowed us to detect the mere presentations and secretions of signalling molecules. To see the actual immune response to these molecules, we would need *in vivo* models, but as far as only detecting the presentation and secretion of the molecules, *in vitro* experiments are appropriate.

6.2.2 Irradiation of cells

As this project explored ICD signalling after co-treatment of irradiation and ATRi, irradiation of samples have been conducted routinely. Most of the radiation sessions have been estimated to yield a dose of 5Gy, but for the exploration of increased pSTAT1 signalling, doses of 20Gy were used. We used doses of 5Gy to get clear effects after radiation, but at

the same time keep the dose in a clinically significant range. Single doses of 20Gy are rarely applied in the clinics, and were only used in verifying experiments (figures 5.29-30). Irradiated samples were placed on a rotating plate under irradiation, in order to ensure consistent exposure for the different samples. Identical samples to be compared were placed diametrically to the centre of the irradiation field to yield exact radiation doses.

The X-ray cabinet used for the irradiations is pre-set to specific doses per minute at different shelf heights. To assure correct doses per minute, the machine is regularly calibrated by maintenance services.

6.2.3 Flow cytometric measurements

As mentioned in section 4.4.1, flow cytometry is a very reliable and applicable detection technique that can be used for single-cell measurements. In this work, the flow cytometry technique has been used for detecting ecto-CRT of cell surfaces through detection of a fluorophore-conjugated antibody complex, and for detecting loss of HMGB1 proteins by detecting fused GFP. This approach has made it possible to detect large-scale populations with single-cell accuracy. With stopping gate settings of 10,000 single cells for each sample, statistically reliable results were made available in relatively short time. The many gating options based on chosen running parameters enable study of sub-populations of specific traits, *e.g.* cells in different cell cycle phases.

For our experiments, flow cytometry was applied to both fixated and live cells. It is generally regarded preferable to use fixated cell samples, as this is not as time sensitive as live cell measurements. Whereas fixated cells can be stored at -20°C for hours and days, live cells have to be run abruptly before they die. For the CRT assay, we tested fixation with both formalin and the BD Cytofix reagent, but none of these spared the plasma membrane integrity (data not shown), and we therefore had to use live cells. The time sensitivity of the live cell flow cytometry used for the CRT assay is therefore labour intensive, but it has been crucial for a reliable detection of ecto-CRT (described in section 5.1.2).

Flow cytometry relies on fluorochrome-conjugated antibodies, or other fluorescent elements such as stains or fluorescent proteins. When using antibodies, it is therefore a necessity for the technique that these are functional. For all the antibody-based flow

cytometry experiments, control samples stained with secondary antibody alone have been included. This is a control of the primary antibody function, and reflects the background secondary antibody signal. Secondary antibody controls specific for each sample is a necessity for the evaluation of antibody-facilitated detection results. Finally, barcoding was included to reduce sample-to-sample variability, as explained in detail in section 5.1.6.

Of note is that cell cycle sub-populations have been gated manually from DNA profile histograms in this project, as shown in figure 5.23. The gates were placed only by eye, and not by use of cell cycle phase-determining algorithms. As we wanted qualitative and not quantitative data from the cell cycle phase gates (the distribution rates in gated phase populations were of minor interest in these experiments), such manually placed gates are considered suitable. The phase gates were made sure to exclude as many cells of other phases as possible, and hence separated by favourable gaps based on the histogram curve.

6.2.4 Western blotting

Contrasting the flow cytometry approach, western blotting of proteins detects the total level of protein from an entire population, and is thereby not able to discriminate signals from individual cells. For the comparison of different samples, protein concentration measurements may be included for equal loading of cell lysates between the samples. In addition, it is vital for the assay to have one or more loading controls. The loading controls are blotting of proteins considered to be expressed evenly between the samples (independent of the treatments), and therefore directly indicate the relative cell numbers between the samples. To check the linearity of antibody binding, chosen samples were loaded in gradients of 100, 75 and 50 per cent (data not shown). This was typically done for the sample expected to give highest signal of interest. Linearity evaluation is done to ensure that the antibodies are kept in linear ranges, with concentrations below the point of interaction saturation.

6.2.5 Antibody reliability

When using antibodies for detection of specific cellular components, the results depend on the reliability of the antibodies. For the CRT assay, we tested that the anti-CRT antibody

stained a pattern consistent with the location of the ER in fixed cells, in order to evaluate its reliability (figure 5.1). For the Western blotting experiment, it was always checked whether the antibodies were specific to protein bands of expected size. Yet, the optimal test for antibody reliability would be to conduct knockout experiments where the antibody target is knocked down, *e.g.* by siRNA transfection or CRISPR/Cas9 gene deletion. By comparing antibody signals from such cell samples with the signal from wild-type expressing cell samples, a better test of the reliability is achieved.

In this project, the antibodies used in compared experiments have been taken from the same batch. This minimise the possibility of signalling variance between the experiments due to variation in antibody efficiency between batches. The use of relative signals for experiment comparison will anyway disable such effects.

6.2.6 Luminometry

Luminometry is an easy and rapid detection method, and is based upon the emission of light. In this project, luminometry was used to detect secretion of ATP, in which an added reagent produced light when combined with ATP (see section 4.7). The chemiluminescence approach is very sensitive, as it is based on enzyme-driven reactions under optimal conditions, provided a redundancy of the *CellTiter-Glo* solution (*i.e.* the involved reactants apart from ATP) is added. The detection is done by spectrophotometry. For the measurements in this project, it was important to have both plate controls (empty wells) and medium controls for the evaluation of the results. An ATP standard curve was also added in most of the experiments, in order to evaluate the results based on the sensitive range of the assay (see section 5.2.6 and figure 5.14). A weakness of the detection method is that signals transmit from one well to its neighbouring wells. We therefore always used plates with white walls in order to minimise signal transmittance. Usually, the transmitted values are too small to impinge upon the results, but it was considered wise to add some spaces between the samples on the plate, in order to avoid such signal contamination. Of note is that the bigger the value of a well, the more widespread the transmitted light is on the plate.

6.3 Concluding remarks

In this thesis, detection techniques for three hallmark factors of immunogenic cell death have been optimised, in order to evaluate the *in vitro* effect of ATR inhibitors on radiation-induced ICD. The study has been executed with the two ATR inhibitors VE822 and AZD6738, of which both are in clinical trials. We find that co-treatment with the ATR inhibitors and IR may contribute to an increased ICD signalling through increased ATP secretion and HMGB1 exodus, but not through ecto-CRT presentation. Further studies are needed to substantiate these results. We also find that ecto-CRT presentation (and perhaps also HMGB1 exodus) is affected by cell cycle phase effects, which to our knowledge is a novel aspect in the field of ICD.

If ATRi can promote the ICD signalling following radiation therapy to such extent that a systemic anti-tumour immune response can be achieved, this may in the long term contribute to increased efficiency of clinical radiotherapy. In addition, a deeper insight into the immune modulatory possibilities of ATR inhibition may comprehend the use of ATR as a therapeutic target.

7 Acknowledgements

This Master project was conducted at the Department for Radiation Biology at the Norwegian Radium Hospital, Oslo University Hospital.

I would like to address my sincere thanks to my main supervisor Randi G. Syljuåsen, Ph.D (group leader) and co-supervisor Sissel Hauge, M.Sc (Ph.D candidate) for all the help, supervision and mentoring during the project. Thank you for all the hours you have put into me. You have always made time for all my questions, and I could not have hoped for better persons to scientifically shape me.

Next, I would like to thank the other members of the research group: Lise Ellefsen Sandquist, M.Sc (Ph.D candidate), Christian Naucke, M.Sc (Ph.D candidate), Gro Elise Rødland, Ph.D (post doc.), Mrinal Joel, Ph.D (post doc.) and Helga Bjarnason Landsverk, Ph.D (researcher). You have included and helped me from day one. Thank you for contributing to a wonderful working environment.

I would also like to thank the people at the Flow Cytometry Core Facility, which is located at our department, for all the help and tips regarding flow cytometry. Finally, I want to thank all the others at the department for creating a nice environment, and my fellow students for encouragement, tips and general chit-chat.

Oslo, May 2018

Adrian Eek Mariampillai

8 List of abbreviations

α	Anti (Greek letter alpha)
µg	Microgram
µl	Microlitre
µM	Micromolar
Alt-NHEJ	Alternative NHEJ
AP	Apurinic/apyrimidinic
APC	Antigen-presenting cell
APE1	AP endonuclease 1
ATM	Ataxia telangiectasia mutated
ATP	Adenosine 5'-triphosphate
ATR	ATM and RAD3 related
ATRi	ATR inhibition
ATRIP	ATR-interacting protein
BAK	Blc-2 homologous antagonist/killer
BAP31	B-cell receptor-associated protein 31
BAX	Bcl-2-associated X protein
BCA	Bicinchoninic acid
BER	Base excision repair
BLM	Bloom
B-NHEJ	Backup NHEJ
BRCA1	Breast cancer type 1 susceptibility protein
BRCA2	Breast cancer type 2 susceptibility protein
BSA	Bovine serum albumin
CD	Cluster differentiation
CDC25A	Cell division cycle 25A
CDC25C	Cell division cycle 25C
CDI	CDK-inhibitor
CDK	Cyclin-dependent kinase
CDKN2A	Cyclin-dependent kinase inhibitor 2A gene
cGAMP	Cyclic dinucleotide GMP/AMP
cGAS	Cyclic GMP/AMP synthase
CHK1	Checkpoint kinase 1
CHK2	Checkpoint kinase 2
cm	Centimetre
CRT	Calreticulin
CtIP	C-terminal binding protein 1 interacting protein
CTLA-4	Cytotoxic T-lymphocyte-associated antigen 4
DAMP	Damage-associated molecular pattern (danger-associated molecular pattern)
DAPI	4',6-diamidino-2-phenylindole
DDR	DNA damage response
dH_2O	Distilled water
DMEM	Dulbecco's modified Eagle's medium

DNA	Deoxyribonucleic acid
DNA-PK	DNA-dependent protein kinase
dRP	5'-deoxyribose phosphate
DSB	Double-stranded DNA-break
dsDNA	Double-stranded DNA
E. coli	*Escherichia coli*
ECL	Enhanced chemiluminescence
Ecto-CRT	Surface presented calreticulin
EDTA	Ethylenediaminetetraacetic acid
eIF2a	Eukaryotic translation initiation factor 2A
ELISA	Enzyme-linked immunosorbent assay
Endo-CRT	Intracellular calreticulin
ER	Endoplasmic reticulum
ETAA1	Erwig's tumour-associated antigen 1
EtOH	Ethanol
EXO1	Exonuclease 1
FBS	Foetal bovine serum
FEN1	Flap endonuclease 1
FSC	Forward-scatter
g	Gram
g	Gravitational force
GFP	Green fluorescent protein
Gy	Gray
H4 pan	Histone 4, all types
hCMV	Human cytomegalovirus
HMGB1	High-mobility group box 1
$HO^{\bullet}$	Hydroxyl radical
HR	Homologous recombination
HRP	Horseradish peroxidase
HSP	Heat-shock protein
IC_{50}	Half maximal inhibitory concentration
ICD	Immunogenic cell death
IFN	Interferon
IKK	IκB kinase
IL	Interleukin
IR	Ionising radiation
IRF3	Interferon regulatory factor-3
IU	International units
JAK	Janus-like activating kinase
kDa	Kilodalton
LAMP1	Lysosomal-associated membrane glycoprotein-1
LB	Lysogeny broth
LPS	Lipopolysaccharide
LRP1	LDL-receptor-related protein

LSB	Loading Sample Buffer
MDM2	Mouse double minute 2 homolog
MeOH	Methanol
MHC	Major histocompability complex
ml	Millilitre
mm	Millimetre
MMEJ	Microhomology-mediated end-joining
MMR	Mismatch repair pathway
mQ dH_2O	MilliQ filtered distilled water
MRE11	Meiotic recombination 11
MRN	MRE11–RAD50–NBS1
mTOR	Mammalian Target of rapamycin
MTX	Mitoxantrone
***n* (or *N*)**	Number
NBS1	Nijmegen breakage syndrome 1
NER	Nucleotide excision repair
NFκB	Nuclear factor-κB
ng	Nanogram
NHEJ	Non-homologous end-joining
NK	Natural killer
nm	Nanometre
nM	Nanomolar
NSCLC	Non-small-cell lung cancer
nt	Nucleotide
OGG1	8-oxoguanine DNA glycosylase
PALB2	Partner and localiser of BRCA2
PAMP	Pathogen-associated molecular pattern
PARP1	Poly-[ADP-ribose] polymerase-1
PARP2	Poly-[ADP-ribose] polymerase-2
PBS	Phosphate buffered saline solution
PBST	Phosphate buffered saline solution with Tween 20
pCMV	Cytomegalovirus promoter
PCNA	Proliferating cell nuclear antigen
PD-1	Programmed cell death receptor 1
PD-L1	PD-1 ligand
Pen-strep	Penicillin-streptomycin
PERK	Protein kinase RNA-like ER kinase
PI	Propidium iodide
PI3K	Phosphatidylinositol 3-kinase
PIKK	Phosphatidylinositol-3 kinase-related kinase
PNUTS	Phosphatase 1 nuclear targeting subunit
PP_i	Free pyrophosphate
pRB	Retinoblastoma protein
PRR	Pattern recognition receptor

pSTAT1	Phosphorylated STAT1
PVDF	Polyvinylidine difluoride
RAGE/AGER	Receptor for advanced glycation endproducts
Rb	Rabbit
RF-C	Replication factor C
RLU	Relative luminescence units
RNA	Ribonucleic acid
RNaseA	Ribonuclease A
RNS	Reactive nitrogen species
ROS	Reactive oxygen species
RPA	Replication protein A
rpm	Rotations per minute
RPMI	Roswell Park Memorial Institute
SDS	Sodium dodecyl sulphate
SDS-PAGE	Sodium dodecyl sulphate polyacrylamide gel electrophoresis
SEM	Standard error of the mean
siRNA	Silencer RNA
SNARE	Soluble NSF attachment protein receptor
SOC	Super optimal broth with catabolite repression
SSB	Single-stranded DNA-break
SSBR	Single-stranded break repair
SSC	Side-scatter
ssDNA	Single-stranded DNA
STAT1	Signal transducer and activator of transcription-1
STING	Stimulator of interferon genes
STR	Short tandem repeat
TAA	Tumour-associated antigen
TBK1	TANK-binding kinase-1
TGF-β	Transforming growth factor β
T_H	Helper T-lymphocyte
TLR	Toll-like receptor
TNF-α	Tumour necrosis factor α
TopBP1	DNA topoisomerase-II-binding protein 1
T_{reg}	Regulatory T-lymphocyte
Tris-HCl	Tris(hydroxymethyl)aminomethane hydrochloride
VAMP1	Vesicle-associated membrane protein-1
VNUT	Vesicular nucleotide transporter
vs.	*Versus*
w/v	Weight volume
WRN	Werner
XLF	XRCC4-like factor
XRCC1	X-ray repair cross-complementing protein 1
XRCC4	X-ray repair cross-complementing protein 4

9 References

1. National Cancer Institute. *What is cancer?* 2015 [cited 2018 20 March]; Available from: https://www.cancer.gov/about-cancer/understanding/what-is-cancer.
2. World Health Organization. *Cancer*. 2018 [cited 2018 30 May]; Available from: http://www.who.int/news-room/fact-sheets/detail/cancer.
3. Cancer Registry of Norway, *Cancer in Norway 2016 - Cancer incidence, mortality, survival and prevalence in Norway*. Oslo: Cancer Registry of Norway, 2017.
4. Weber, A.M. and A.J. Ryan, *ATM and ATR as therapeutic targets in cancer.* Pharmacol Ther, 2015. **149**: p. 124-38.
5. Lindahl, T., *Instability and decay of the primary structure of DNA.* Nature, 1993. **362**(6422): p. 709-15.
6. Helleday, T., E. Petermann, C. Lundin, B. Hodgson, and R.A. Sharma, *DNA repair pathways as targets for cancer therapy.* Nat Rev Cancer, 2008. **8**(3): p. 193-204.
7. Mladenov, E., S. Magin, A. Soni, and G. Iliakis, *DNA double-strand break repair as determinant of cellular radiosensitivity to killing and target in radiation therapy.* Front Oncol, 2013. **3**: p. 113.
8. Hutchinson, F., *Chemical changes induced in DNA by ionizing radiation.* Prog Nucleic Acid Res Mol Biol, 1985. **32**: p. 115-54.
9. Sancar, A., L.A. Lindsey-Boltz, K. Unsal-Kacmaz, and S. Linn, *Molecular mechanisms of mammalian DNA repair and the DNA damage checkpoints.* Annu Rev Biochem, 2004. **73**: p. 39-85.
10. Jackson, S.P. and J. Bartek, *The DNA-damage response in human biology and disease.* Nature, 2009. **461**(7267): p. 1071-8.
11. Frey, B., A. Derer, H. Scheithauer, R. Wunderlich, R. Fietkau, and U.S. Gaipl, *Cancer Cell Death-Inducing Radiotherapy: Impact on Local Tumour Control, Tumour Cell Proliferation and Induction of Systemic Anti-tumour Immunity.* Adv Exp Med Biol, 2016. **930**: p. 151-72.
12. Syljuasen, R.G., G. Hasvold, S. Hauge, and A. Helland, *Targeting lung cancer through inhibition of checkpoint kinases.* Front Genet, 2015. **6**: p. 70.
13. Smith, J., L.M. Tho, N. Xu, and D.A. Gillespie, *The ATM-Chk2 and ATR-Chk1 pathways in DNA damage signaling and cancer.* Adv Cancer Res, 2010. **108**: p. 73-112.
14. Matsuoka, S., B.A. Ballif, A. Smogorzewska, E.R. McDonald, 3rd, K.E. Hurov, J. Luo, C.E. Bakalarski, Z. Zhao, N. Solimini, Y. Lerenthal, et al., *ATM and ATR substrate analysis reveals extensive protein networks responsive to DNA damage.* Science, 2007. **316**(5828): p. 1160-6.
15. Uziel, T., Y. Lerenthal, L. Moyal, Y. Andegeko, L. Mittelman, and Y. Shiloh, *Requirement of the MRN complex for ATM activation by DNA damage.* Embo j, 2003. **22**(20): p. 5612-21.
16. Lee, J.H. and T.T. Paull, *ATM activation by DNA double-strand breaks through the Mre11-Rad50-Nbs1 complex.* Science, 2005. **308**(5721): p. 551-4.
17. Bakkenist, C.J. and M.B. Kastan, *DNA damage activates ATM through intermolecular autophosphorylation and dimer dissociation.* Nature, 2003. **421**(6922): p. 499-506.
18. Kumagai, A., J. Lee, H.Y. Yoo, and W.G. Dunphy, *TopBP1 activates the ATR-ATRIP complex.* Cell, 2006. **124**(5): p. 943-55.

19. Kumagai, A., S.M. Kim, and W.G. Dunphy, *Claspin and the activated form of ATR-ATRIP collaborate in the activation of Chk1.* J Biol Chem, 2004. **279**(48): p. 49599-608.
20. Haahr, P., S. Hoffmann, M.A. Tollenaere, T. Ho, L.I. Toledo, M. Mann, S. Bekker-Jensen, M. Raschle, and N. Mailand, *Activation of the ATR kinase by the RPA-binding protein ETAA1.* Nat Cell Biol, 2016. **18**(11): p. 1196-1207.
21. Braun-Dullaeus, R.C., M.J. Mann, and V.J. Dzau, *Cell cycle progression: new therapeutic target for vascular proliferative disease.* Circulation, 1998. **98**(1): p. 82-9.
22. Malumbres, M. and M. Barbacid, *Cell cycle, CDKs and cancer: a changing paradigm.* Nat Rev Cancer, 2009. **9**(3): p. 153-66.
23. Grana, X. and E.P. Reddy, *Cell cycle control in mammalian cells: role of cyclins, cyclin dependent kinases (CDKs), growth suppressor genes and cyclin-dependent kinase inhibitors (CKIs).* Oncogene, 1995. **11**(2): p. 211-9.
24. Weinberg, R.A., *The Biology of Cancer*. 2nd ed. 2014: Garland Science.
25. Pardee, A.B., *A restriction point for control of normal animal cell proliferation.* Proc Natl Acad Sci U S A, 1974. **71**(4): p. 1286-90.
26. Weinberg, R.A., *The retinoblastoma protein and cell cycle control.* Cell, 1995. **81**(3): p. 323-30.
27. Planas-Silva, M.D. and R.A. Weinberg, *The restriction point and control of cell proliferation.* Curr Opin Cell Biol, 1997. **9**(6): p. 768-72.
28. Helin, K., E. Harlow, and A. Fattaey, *Inhibition of E2F-1 transactivation by direct binding of the retinoblastoma protein.* Mol Cell Biol, 1993. **13**(10): p. 6501-8.
29. Ezhevsky, S.A., H. Nagahara, A.M. Vocero-Akbani, D.R. Gius, M.C. Wei, and S.F. Dowdy, *Hypo-phosphorylation of the retinoblastoma protein (pRb) by cyclin D:Cdk4/6 complexes results in active pRb.* Proc Natl Acad Sci U S A, 1997. **94**(20): p. 10699-704.
30. Kuerbitz, S.J., B.S. Plunkett, W.V. Walsh, and M.B. Kastan, *Wild-type p53 is a cell cycle checkpoint determinant following irradiation.* Proc Natl Acad Sci U S A, 1992. **89**(16): p. 7491-5.
31. Lauber, K., A. Ernst, M. Orth, M. Herrmann, and C. Belka, *Dying cell clearance and its impact on the outcome of tumor radiotherapy.* Front Oncol, 2012. **2**: p. 116.
32. Xiong, Y., G.J. Hannon, H. Zhang, D. Casso, R. Kobayashi, and D. Beach, *p21 is a universal inhibitor of cyclin kinases.* Nature, 1993. **366**(6456): p. 701-4.
33. Waga, S., G.J. Hannon, D. Beach, and B. Stillman, *The p21 inhibitor of cyclin-dependent kinases controls DNA replication by interaction with PCNA.* Nature, 1994. **369**(6481): p. 574-8.
34. Mailand, N., J. Falck, C. Lukas, R.G. Syljuasen, M. Welcker, J. Bartek, and J. Lukas, *Rapid destruction of human Cdc25A in response to DNA damage.* Science, 2000. **288**(5470): p. 1425-9.
35. Ma, C.X., J.W. Janetka, and H. Piwnica-Worms, *Death by releasing the breaks: CHK1 inhibitors as cancer therapeutics.* Trends Mol Med, 2011. **17**(2): p. 88-96.
36. Kastan, M.B. and D.S. Lim, *The many substrates and functions of ATM.* Nat Rev Mol Cell Biol, 2000. **1**(3): p. 179-86.
37. Iliakis, G., Y. Wang, J. Guan, and H. Wang, *DNA damage checkpoint control in cells exposed to ionizing radiation.* Oncogene, 2003. **22**(37): p. 5834-47.
38. Innocente, S.A., J.L. Abrahamson, J.P. Cogswell, and J.M. Lee, *p53 regulates a G2 checkpoint through cyclin B1.* Proc Natl Acad Sci U S A, 1999. **96**(5): p. 2147-52.

39. O'Connell, M.J., J.M. Raleigh, H.M. Verkade, and P. Nurse, *Chk1 is a wee1 kinase in the G2 DNA damage checkpoint inhibiting cdc2 by Y15 phosphorylation.* Embo j, 1997. **16**(3): p. 545-54.
40. Lundgren, K., N. Walworth, R. Booher, M. Dembski, M. Kirschner, and D. Beach, *mik1 and wee1 cooperate in the inhibitory tyrosine phosphorylation of cdc2.* Cell, 1991. **64**(6): p. 1111-22.
41. Yarden, R.I., S. Pardo-Reoyo, M. Sgagias, K.H. Cowan, and L.C. Brody, *BRCA1 regulates the G2/M checkpoint by activating Chk1 kinase upon DNA damage.* Nat Genet, 2002. **30**(3): p. 285-9.
42. Menzel, T., V. Nahse-Kumpf, A.N. Kousholt, D.K. Klein, C. Lund-Andersen, M. Lees, J.V. Johansen, R.G. Syljuasen, and C.S. Sorensen, *A genetic screen identifies BRCA2 and PALB2 as key regulators of G2 checkpoint maintenance.* EMBO Rep, 2011. **12**(7): p. 705-12.
43. Venkitaraman, A.R., *Cancer susceptibility and the functions of BRCA1 and BRCA2.* Cell, 2002. **108**(2): p. 171-82.
44. Bruner, S.D., D.P. Norman, and G.L. Verdine, *Structural basis for recognition and repair of the endogenous mutagen 8-oxoguanine in DNA.* Nature, 2000. **403**(6772): p. 859-66.
45. Izumi, T., T.K. Hazra, I. Boldogh, A.E. Tomkinson, M.S. Park, S. Ikeda, and S. Mitra, *Requirement for human AP endonuclease 1 for repair of 3'-blocking damage at DNA single-strand breaks induced by reactive oxygen species.* Carcinogenesis, 2000. **21**(7): p. 1329-34.
46. de Murcia, J.M., C. Niedergang, C. Trucco, M. Ricoul, B. Dutrillaux, M. Mark, F.J. Oliver, M. Masson, A. Dierich, M. LeMeur, et al., *Requirement of poly(ADP-ribose) polymerase in recovery from DNA damage in mice and in cells.* Proc Natl Acad Sci U S A, 1997. **94**(14): p. 7303-7.
47. Dantzer, F., G. de La Rubia, J. Menissier-De Murcia, Z. Hostomsky, G. de Murcia, and V. Schreiber, *Base excision repair is impaired in mammalian cells lacking Poly(ADP-ribose) polymerase-1.* Biochemistry, 2000. **39**(25): p. 7559-69.
48. De Vos, M., V. Schreiber, and F. Dantzer, *The diverse roles and clinical relevance of PARPs in DNA damage repair: current state of the art.* Biochem Pharmacol, 2012. **84**(2): p. 137-46.
49. Kubota, Y., R.A. Nash, A. Klungland, P. Schar, D.E. Barnes, and T. Lindahl, *Reconstitution of DNA base excision-repair with purified human proteins: interaction between DNA polymerase beta and the XRCC1 protein.* Embo j, 1996. **15**(23): p. 6662-70.
50. Stucki, M., B. Pascucci, E. Parlanti, P. Fortini, S.H. Wilson, U. Hubscher, and E. Dogliotti, *Mammalian base excision repair by DNA polymerases delta and epsilon.* Oncogene, 1998. **17**(7): p. 835-43.
51. Gary, R., K. Kim, H.L. Cornelius, M.S. Park, and Y. Matsumoto, *Proliferating cell nuclear antigen facilitates excision in long-patch base excision repair.* J Biol Chem, 1999. **274**(7): p. 4354-63.
52. Prasad, R., G.L. Dianov, V.A. Bohr, and S.H. Wilson, *FEN1 stimulation of DNA polymerase beta mediates an excision step in mammalian long patch base excision repair.* J Biol Chem, 2000. **275**(6): p. 4460-6.

53. Sartori, A.A., C. Lukas, J. Coates, M. Mistrik, S. Fu, J. Bartek, R. Baer, J. Lukas, and S.P. Jackson, *Human CtIP promotes DNA end resection.* Nature, 2007. **450**(7169): p. 509-14.
54. Nicolette, M.L., K. Lee, Z. Guo, M. Rani, J.M. Chow, S.E. Lee, and T.T. Paull, *Mre11-Rad50-Xrs2 and Sae2 promote 5' strand resection of DNA double-strand breaks.* Nat Struct Mol Biol, 2010. **17**(12): p. 1478-85.
55. Van Dyck, E., A.Z. Stasiak, A. Stasiak, and S.C. West, *Binding of double-strand breaks in DNA by human Rad52 protein.* Nature, 1999. **398**(6729): p. 728-31.
56. New, J.H., T. Sugiyama, E. Zaitseva, and S.C. Kowalczykowski, *Rad52 protein stimulates DNA strand exchange by Rad51 and replication protein A.* Nature, 1998. **391**(6665): p. 407-10.
57. Sugiyama, T., J.H. New, and S.C. Kowalczykowski, *DNA annealing by RAD52 protein is stimulated by specific interaction with the complex of replication protein A and single-stranded DNA.* Proc Natl Acad Sci U S A, 1998. **95**(11): p. 6049-54.
58. Li, X., C.M. Stith, P.M. Burgers, and W.D. Heyer, *PCNA is required for initiation of recombination-associated DNA synthesis by DNA polymerase delta.* Mol Cell, 2009. **36**(4): p. 704-13.
59. Maloisel, L., F. Fabre, and S. Gangloff, *DNA polymerase delta is preferentially recruited during homologous recombination to promote heteroduplex DNA extension.* Mol Cell Biol, 2008. **28**(4): p. 1373-82.
60. Cox, M.M. and I.R. Lehman, *recA protein of Escherichia coli promotes branch migration, a kinetically distinct phase of DNA strand exchange.* Proc Natl Acad Sci U S A, 1981. **78**(6): p. 3433-7.
61. Holliday, R., *A mechanism for gene conversion in fungi.* Genet Res, 2007. **89**(5-6): p. 285-307.
62. Ip, S.C., U. Rass, M.G. Blanco, H.R. Flynn, J.M. Skehel, and S.C. West, *Identification of Holliday junction resolvases from humans and yeast.* Nature, 2008. **456**(7220): p. 357-61.
63. Goetz, J.D., T.A. Motycka, M. Han, M. Jasin, and A.E. Tomkinson, *Reduced repair of DNA double-strand breaks by homologous recombination in a DNA ligase I-deficient human cell line.* DNA Repair (Amst), 2005. **4**(6): p. 649-54.
64. Lieber, M.R., Y. Ma, U. Pannicke, and K. Schwarz, *Mechanism and regulation of human non-homologous DNA end-joining.* Nat Rev Mol Cell Biol, 2003. **4**(9): p. 712-20.
65. Nick McElhinny, S.A., C.M. Snowden, J. McCarville, and D.A. Ramsden, *Ku recruits the XRCC4-ligase IV complex to DNA ends.* Mol Cell Biol, 2000. **20**(9): p. 2996-3003.
66. Ahnesorg, P., P. Smith, and S.P. Jackson, *XLF interacts with the XRCC4-DNA ligase IV complex to promote DNA nonhomologous end-joining.* Cell, 2006. **124**(2): p. 301-13.
67. Callebaut, I., L. Malivert, A. Fischer, J.P. Mornon, P. Revy, and J.P. de Villartay, *Cernunnos interacts with the XRCC4 x DNA-ligase IV complex and is homologous to the yeast nonhomologous end-joining factor Nej1.* J Biol Chem, 2006. **281**(20): p. 13857-60.
68. Grawunder, U., M. Wilm, X. Wu, P. Kulesza, T.E. Wilson, M. Mann, and M.R. Lieber, *Activity of DNA ligase IV stimulated by complex formation with XRCC4 protein in mammalian cells.* Nature, 1997. **388**(6641): p. 492-5.

69. Keijzers, G., S. Maynard, R.A. Shamanna, L.J. Rasmussen, D.L. Croteau, and V.A. Bohr, *The role of RecQ helicases in non-homologous end-joining.* Crit Rev Biochem Mol Biol, 2014. **49**(6): p. 463-72.
70. El Ghissassi, F., R. Baan, K. Straif, Y. Grosse, B. Secretan, V. Bouvard, L. Benbrahim-Tallaa, N. Guha, C. Freeman, L. Galichet, et al., *A review of human carcinogens--part D: radiation.* Lancet Oncol, 2009. **10**(8): p. 751-2.
71. Allisy-Roberts, P.J., *Radiation quantities and units--understanding the sievert.* J Radiol Prot, 2005. **25**(1): p. 97-100.
72. Wyckoff, H.O., A. Allisy, and K. Liden, *The new special names of SI units in the field of ionizing radiations.* Rofo, 1975. **123**(6): p. 579-80.
73. Seibert, J.A., *X-ray imaging physics for nuclear medicine technologists. Part 1: Basic principles of x-ray production.* J Nucl Med Technol, 2004. **32**(3): p. 139-47.
74. Riley, P.A., *Free radicals in biology: oxidative stress and the effects of ionizing radiation.* Int J Radiat Biol, 1994. **65**(1): p. 27-33.
75. Leach, J.K., G. Van Tuyle, P.S. Lin, R. Schmidt-Ullrich, and R.B. Mikkelsen, *Ionizing radiation-induced, mitochondria-dependent generation of reactive oxygen/nitrogen.* Cancer Res, 2001. **61**(10): p. 3894-901.
76. Arnold, E., M. Joiner, and A. van der Kogel, *Basic Clinical Radiobiology*. 4th ed. 2009: Hodder Arnold.
77. Okada, H. and T.W. Mak, *Pathways of apoptotic and non-apoptotic death in tumour cells.* Nat Rev Cancer, 2004. **4**(8): p. 592-603.
78. Chu, K., N. Teele, M.W. Dewey, N. Albright, and W.C. Dewey, *Computerized video time lapse study of cell cycle delay and arrest, mitotic catastrophe, apoptosis and clonogenic survival in irradiated 14-3-3sigma and CDKN1A (p21) knockout cell lines.* Radiat Res, 2004. **162**(3): p. 270-86.
79. Ahmed, M.M., J.W. Hodge, C. Guha, E.J. Bernhard, B. Vikram, and C.N. Coleman, *Harnessing the potential of radiation-induced immune modulation for cancer therapy.* Cancer Immunol Res, 2013. **1**(5): p. 280-4.
80. Ganz, P.A., *Late effects of cancer and its treatment.* Semin Oncol Nurs, 2001. **17**(4): p. 241-8.
81. Kang, J., S. Demaria, and S. Formenti, *Current clinical trials testing the combination of immunotherapy with radiotherapy.* J Immunother Cancer, 2016. **4**: p. 51.
82. Bernier, J., E.J. Hall, and A. Giaccia, *Radiation oncology: a century of achievements.* Nat Rev Cancer, 2004. **4**(9): p. 737-47.
83. Castedo, M., J.L. Perfettini, T. Roumier, K. Andreau, R. Medema, and G. Kroemer, *Cell death by mitotic catastrophe: a molecular definition.* Oncogene, 2004. **23**(16): p. 2825-37.
84. Fokas, E., R. Prevo, J.R. Pollard, P.M. Reaper, P.A. Charlton, B. Cornelissen, K.A. Vallis, E.M. Hammond, M.M. Olcina, W. Gillies McKenna, et al., *Targeting ATR in vivo using the novel inhibitor VE-822 results in selective sensitization of pancreatic tumors to radiation.* Cell Death Dis, 2012. **3**: p. e441.
85. Reaper, P.M., M.R. Griffiths, J.M. Long, J.D. Charrier, S. Maccormick, P.A. Charlton, J.M. Golec, and J.R. Pollard, *Selective killing of ATM- or p53-deficient cancer cells through inhibition of ATR.* Nat Chem Biol, 2011. **7**(7): p. 428-30.
86. Sausville, E., P. Lorusso, M. Carducci, J. Carter, M.F. Quinn, L. Malburg, N. Azad, D. Cosgrove, R. Knight, P. Barker, et al., *Phase I dose-escalation study of AZD7762, a*

checkpoint kinase inhibitor, in combination with gemcitabine in US patients with advanced solid tumors. Cancer Chemother Pharmacol, 2014. **73**(3): p. 539-49.
87. Sorensen, C.S. and R.G. Syljuasen, *Safeguarding genome integrity: the checkpoint kinases ATR, CHK1 and WEE1 restrain CDK activity during normal DNA replication.* Nucleic Acids Res, 2012. **40**(2): p. 477-86.
88. Prevo, R., E. Fokas, P.M. Reaper, P.A. Charlton, J.R. Pollard, W.G. McKenna, R.J. Muschel, and T.B. Brunner, *The novel ATR inhibitor VE-821 increases sensitivity of pancreatic cancer cells to radiation and chemotherapy.* Cancer Biol Ther, 2012. **13**(11): p. 1072-81.
89. Selleckchem. *VE-822*. 2018; Available from: http://www.selleckchem.com/products/ve-822.html.
90. Selleckchem. *AZD6738*. 2018; Available from: http://www.selleckchem.com/products/azd6738.html.
91. Kasahara, M., J. Nakaya, Y. Satta, and N. Takahata, *Chromosomal duplication and the emergence of the adaptive immune system.* Trends Genet, 1997. **13**(3): p. 90-2.
92. Janeway, C.A., Jr., P. Travers, M. Walport, and M.J. Shlomchik, *Immunobiology: The Immune System in Health and Disease*. 5th ed. 2001: Garland Science.
93. Mantovani, A., P. Allavena, A. Sica, and F. Balkwill, *Cancer-related inflammation.* Nature, 2008. **454**(7203): p. 436-44.
94. Medzhitov, R. and C.A. Janeway, Jr., *Decoding the patterns of self and nonself by the innate immune system.* Science, 2002. **296**(5566): p. 298-300.
95. Karre, K., H.G. Ljunggren, G. Piontek, and R. Kiessling, *Selective rejection of H-2-deficient lymphoma variants suggests alternative immune defence strategy.* Nature, 1986. **319**(6055): p. 675-8.
96. Matzinger, P., *The danger model: a renewed sense of self.* Science, 2002. **296**(5566): p. 301-5.
97. Sakaguchi, S., N. Sakaguchi, M. Asano, M. Itoh, and M. Toda, *Immunologic self-tolerance maintained by activated T cells expressing IL-2 receptor alpha-chains (CD25). Breakdown of a single mechanism of self-tolerance causes various autoimmune diseases.* J Immunol, 1995. **155**(3): p. 1151-64.
98. Topalian, S.L., C.G. Drake, and D.M. Pardoll, *Immune checkpoint blockade: a common denominator approach to cancer therapy.* Cancer Cell, 2015. **27**(4): p. 450-61.
99. Le Blanc, K. and D. Mougiakakos, *Multipotent mesenchymal stromal cells and the innate immune system.* Nat Rev Immunol, 2012. **12**(5): p. 383-96.
100. Gasque, P., *Complement: a unique innate immune sensor for danger signals.* Mol Immunol, 2004. **41**(11): p. 1089-98.
101. Atkinson, J.P. and T. Farries, *Separation of self from non-self in the complement system.* Immunol Today, 1987. **8**(7-8): p. 212-5.
102. Medzhitov, R. and C.A. Janeway, Jr., *Innate immunity: the virtues of a nonclonal system of recognition.* Cell, 1997. **91**(3): p. 295-8.
103. Stahl, P.D., *The mannose receptor and other macrophage lectins.* Curr Opin Immunol, 1992. **4**(1): p. 49-52.
104. Pearson, A.M., *Scavenger receptors in innate immunity.* Curr Opin Immunol, 1996. **8**(1): p. 20-8.
105. Akira, S., S. Uematsu, and O. Takeuchi, *Pathogen recognition and innate immunity.* Cell, 2006. **124**(4): p. 783-801.

106. Li, X.D., J. Wu, D. Gao, H. Wang, L. Sun, and Z.J. Chen, *Pivotal roles of cGAS-cGAMP signaling in antiviral defense and immune adjuvant effects.* Science, 2013. **341**(6152): p. 1390-4.
107. Sun, L., J. Wu, F. Du, X. Chen, and Z.J. Chen, *Cyclic GMP-AMP synthase is a cytosolic DNA sensor that activates the type I interferon pathway.* Science, 2013. **339**(6121): p. 786-91.
108. Batista, F.D. and N.E. Harwood, *The who, how and where of antigen presentation to B cells.* Nat Rev Immunol, 2009. **9**(1): p. 15-27.
109. Lanzavecchia, A. and F. Sallusto, *Regulation of T cell immunity by dendritic cells.* Cell, 2001. **106**(3): p. 263-6.
110. Noelle, R.J., M. Roy, D.M. Shepherd, I. Stamenkovic, J.A. Ledbetter, and A. Aruffo, *A 39-kDa protein on activated helper T cells binds CD40 and transduces the signal for cognate activation of B cells.* Proceedings of the National Academy of Sciences, 1992. **89**(14): p. 6550-6554.
111. Banchereau, J. and R.M. Steinman, *Dendritic cells and the control of immunity.* Nature, 1998. **392**(6673): p. 245-52.
112. Hanahan, D. and R.A. Weinberg, *Hallmarks of cancer: the next generation.* Cell, 2011. **144**(5): p. 646-74.
113. Walunas, T.L., D.J. Lenschow, C.Y. Bakker, P.S. Linsley, G.J. Freeman, J.M. Green, C.B. Thompson, and J.A. Bluestone, *CTLA-4 can function as a negative regulator of T cell activation.* Immunity, 1994. **1**(5): p. 405-13.
114. Carter, L., L.A. Fouser, J. Jussif, L. Fitz, B. Deng, C.R. Wood, M. Collins, T. Honjo, G.J. Freeman, and B.M. Carreno, *PD-1:PD-L inhibitory pathway affects both CD4(+) and CD8(+) T cells and is overcome by IL-2.* Eur J Immunol, 2002. **32**(3): p. 634-43.
115. Pardoll, D.M., *The blockade of immune checkpoints in cancer immunotherapy.* Nat Rev Cancer, 2012. **12**(4): p. 252-64.
116. Patel, S.P. and R. Kurzrock, *PD-L1 Expression as a Predictive Biomarker in Cancer Immunotherapy.* Mol Cancer Ther, 2015. **14**(4): p. 847-56.
117. Iwai, Y., J. Hamanishi, K. Chamoto, and T. Honjo, *Cancer immunotherapies targeting the PD-1 signaling pathway.* J Biomed Sci, 2017. **24**(1): p. 26.
118. Patel, S.A. and A.J. Minn, *Combination cancer therapy with immune checkpoint blockade: mechanisms and strategies.* Immunity, 2018. **48**(3): p. 417-433.
119. Blachere, N.E., R.B. Darnell, and M.L. Albert, *Apoptotic cells deliver processed antigen to dendritic cells for cross-presentation.* PLoS Biol, 2005. **3**(6): p. e185.
120. Obeid, M., T. Panaretakis, A. Tesniere, N. Joza, R. Tufi, L. Apetoh, F. Ghiringhelli, L. Zitvogel, and G. Kroemer, *Leveraging the immune system during chemotherapy: moving calreticulin to the cell surface converts apoptotic death from "silent" to immunogenic.* Cancer Res, 2007. **67**(17): p. 7941-4.
121. Krysko, D.V., A.D. Garg, A. Kaczmarek, O. Krysko, P. Agostinis, and P. Vandenabeele, *Immunogenic cell death and DAMPs in cancer therapy.* Nat Rev Cancer, 2012. **12**(12): p. 860-75.
122. Golden, E.B., D. Frances, I. Pellicciotta, S. Demaria, M. Helen Barcellos-Hoff, and S.C. Formenti, *Radiation fosters dose-dependent and chemotherapy-induced immunogenic cell death.* Oncoimmunology, 2014. **3**: p. e28518.
123. Gameiro, S.R., M.L. Jammeh, M.M. Wattenberg, K.Y. Tsang, S. Ferrone, and J.W. Hodge, *Radiation-induced immunogenic modulation of tumor enhances antigen*

processing and calreticulin exposure, resulting in enhanced T-cell killing. Oncotarget, 2014. **5**(2): p. 403-16.
124. Vatner, R.E., B.T. Cooper, C. Vanpouille-Box, S. Demaria, and S.C. Formenti, *Combinations of immunotherapy and radiation in cancer therapy.* Front Oncol, 2014. **4**: p. 325.
125. Siva, S., M.P. MacManus, R.F. Martin, and O.A. Martin, *Abscopal effects of radiation therapy: a clinical review for the radiobiologist.* Cancer Lett, 2015. **356**(1): p. 82-90.
126. Mole, R., *Whole body irradiation—radiobiology or medicine?* The British journal of radiology, 1953. **26**(305): p. 234-241.
127. Demaria, S., B. Ng, M.L. Devitt, J.S. Babb, N. Kawashima, L. Liebes, and S.C. Formenti, *Ionizing radiation inhibition of distant untreated tumors (abscopal effect) is immune mediated.* Int J Radiat Oncol Biol Phys, 2004. **58**(3): p. 862-70.
128. Lin, A., B. Truong, S. Patel, N. Kaushik, E.H. Choi, G. Fridman, A. Fridman, and V. Miller, *Nanosecond-Pulsed DBD Plasma-Generated Reactive Oxygen Species Trigger Immunogenic Cell Death in A549 Lung Carcinoma Cells through Intracellular Oxidative Stress.* Int J Mol Sci, 2017. **18**(5).
129. Kepp, O., L. Senovilla, I. Vitale, E. Vacchelli, S. Adjemian, P. Agostinis, L. Apetoh, F. Aranda, V. Barnaba, N. Bloy, et al., *Consensus guidelines for the detection of immunogenic cell death.* Oncoimmunology, 2014. **3**(9): p. e955691.
130. Garg, A.D., D.V. Krysko, T. Verfaillie, A. Kaczmarek, G.B. Ferreira, T. Marysael, N. Rubio, M. Firczuk, C. Mathieu, A.J. Roebroek, et al., *A novel pathway combining calreticulin exposure and ATP secretion in immunogenic cancer cell death.* Embo j, 2012. **31**(5): p. 1062-79.
131. Krause, K.H. and M. Michalak, *Calreticulin.* Cell, 1997. **88**(4): p. 439-43.
132. Gao, B., R. Adhikari, M. Howarth, K. Nakamura, M.C. Gold, A.B. Hill, R. Knee, M. Michalak, and T. Elliott, *Assembly and antigen-presenting function of MHC class I molecules in cells lacking the ER chaperone calreticulin.* Immunity, 2002. **16**(1): p. 99-109.
133. Panaretakis, T., O. Kepp, U. Brockmeier, A. Tesniere, A.C. Bjorklund, D.C. Chapman, M. Durchschlag, N. Joza, G. Pierron, P. van Endert, et al., *Mechanisms of pre-apoptotic calreticulin exposure in immunogenic cell death.* Embo j, 2009. **28**(5): p. 578-90.
134. Ghiran, I., L.B. Klickstein, and A. Nicholson-Weller, *Calreticulin is at the surface of circulating neutrophils and uses CD59 as an adaptor molecule.* J Biol Chem, 2003. **278**(23): p. 21024-31.
135. Gardai, S.J., K.A. McPhillips, S.C. Frasch, W.J. Janssen, A. Starefeldt, J.E. Murphy-Ullrich, D.L. Bratton, P.A. Oldenborg, M. Michalak, and P.M. Henson, *Cell-surface calreticulin initiates clearance of viable or apoptotic cells through trans-activation of LRP on the phagocyte.* Cell, 2005. **123**(2): p. 321-34.
136. Arosa, F.A., O. de Jesus, G. Porto, A.M. Carmo, and M. de Sousa, *Calreticulin is expressed on the cell surface of activated human peripheral blood T lymphocytes in association with major histocompatibility complex class I molecules.* J Biol Chem, 1999. **274**(24): p. 16917-22.
137. Obeid, M., A. Tesniere, F. Ghiringhelli, G.M. Fimia, L. Apetoh, J.L. Perfettini, M. Castedo, G. Mignot, T. Panaretakis, N. Casares, et al., *Calreticulin exposure dictates the immunogenicity of cancer cell death.* Nat Med, 2007. **13**(1): p. 54-61.

138. Parkkinen, J., E. Raulo, J. Merenmies, R. Nolo, E.O. Kajander, M. Baumann, and H. Rauvala, *Amphoterin, the 30-kDa protein in a family of HMG1-type polypeptides. Enhanced expression in transformed cells, leading edge localization, and interactions with plasminogen activation.* J Biol Chem, 1993. **268**(26): p. 19726-38.
139. Andersson, U. and K.J. Tracey, *HMGB1 in sepsis.* Scand J Infect Dis, 2003. **35**(9): p. 577-84.
140. Giese, K., J. Cox, and R. Grosschedl, *The HMG domain of lymphoid enhancer factor 1 bends DNA and facilitates assembly of functional nucleoprotein structures.* Cell, 1992. **69**(1): p. 185-95.
141. Paull, T.T., M.J. Haykinson, and R.C. Johnson, *The nonspecific DNA-binding and -bending proteins HMG1 and HMG2 promote the assembly of complex nucleoprotein structures.* Genes Dev, 1993. **7**(8): p. 1521-34.
142. Bergeron, S., T. Madathiparambil, and P.C. Swanson, *Both high mobility group (HMG)-boxes and the acidic tail of HMGB1 regulate recombination-activating gene (RAG)-mediated recombination signal synapsis and cleavage in vitro.* J Biol Chem, 2005. **280**(35): p. 31314-24.
143. Agresti, A., R. Lupo, M.E. Bianchi, and S. Muller, *HMGB1 interacts differentially with members of the Rel family of transcription factors.* Biochem Biophys Res Commun, 2003. **302**(2): p. 421-6.
144. Tang, D., R. Kang, K.M. Livesey, C.W. Cheh, A. Farkas, P. Loughran, G. Hoppe, M.E. Bianchi, K.J. Tracey, H.J. Zeh, 3rd, et al., *Endogenous HMGB1 regulates autophagy.* J Cell Biol, 2010. **190**(5): p. 881-92.
145. Gardella, S., C. Andrei, D. Ferrera, L.V. Lotti, M.R. Torrisi, M.E. Bianchi, and A. Rubartelli, *The nuclear protein HMGB1 is secreted by monocytes via a non-classical, vesicle-mediated secretory pathway.* EMBO Rep, 2002. **3**(10): p. 995-1001.
146. Bell, C.W., W. Jiang, C.F. Reich, 3rd, and D.S. Pisetsky, *The extracellular release of HMGB1 during apoptotic cell death.* Am J Physiol Cell Physiol, 2006. **291**(6): p. C1318-25.
147. Park, J.S., F. Gamboni-Robertson, Q. He, D. Svetkauskaite, J.Y. Kim, D. Strassheim, J.W. Sohn, S. Yamada, I. Maruyama, A. Banerjee, et al., *High mobility group box 1 protein interacts with multiple Toll-like receptors.* Am J Physiol Cell Physiol, 2006. **290**(3): p. C917-24.
148. Kokkola, R., A. Andersson, G. Mullins, T. Ostberg, C.J. Treutiger, B. Arnold, P. Nawroth, U. Andersson, R.A. Harris, and H.E. Harris, *RAGE is the major receptor for the proinflammatory activity of HMGB1 in rodent macrophages.* Scand J Immunol, 2005. **61**(1): p. 1-9.
149. Yu, M., H. Wang, A. Ding, D.T. Golenbock, E. Latz, C.J. Czura, M.J. Fenton, K.J. Tracey, and H. Yang, *HMGB1 signals through toll-like receptor (TLR) 4 and TLR2.* Shock, 2006. **26**(2): p. 174-9.
150. Wang, H., O. Bloom, M. Zhang, J.M. Vishnubhakat, M. Ombrellino, J. Che, A. Frazier, H. Yang, S. Ivanova, L. Borovikova, et al., *HMG-1 as a late mediator of endotoxin lethality in mice.* Science, 1999. **285**(5425): p. 248-51.
151. Wang, H., J.M. Vishnubhakat, O. Bloom, M. Zhang, M. Ombrellino, A. Sama, and K.J. Tracey, *Proinflammatory cytokines (tumor necrosis factor and interleukin 1) stimulate release of high mobility group protein-1 by pituicytes.* Surgery, 1999. **126**(2): p. 389-92.

152. Michaud, M., I. Martins, A.Q. Sukkurwala, S. Adjemian, Y. Ma, P. Pellegatti, S. Shen, O. Kepp, M. Scoazec, G. Mignot, et al., *Autophagy-dependent anticancer immune responses induced by chemotherapeutic agents in mice.* Science, 2011. **334**(6062): p. 1573-7.
153. Ghiringhelli, F., L. Apetoh, A. Tesniere, L. Aymeric, Y. Ma, C. Ortiz, K. Vermaelen, T. Panaretakis, G. Mignot, E. Ullrich, et al., *Activation of the NLRP3 inflammasome in dendritic cells induces IL-1beta-dependent adaptive immunity against tumors.* Nat Med, 2009. **15**(10): p. 1170-8.
154. Martins, I., Y. Wang, M. Michaud, Y. Ma, A.Q. Sukkurwala, S. Shen, O. Kepp, D. Metivier, L. Galluzzi, J.L. Perfettini, et al., *Molecular mechanisms of ATP secretion during immunogenic cell death.* Cell Death Differ, 2014. **21**(1): p. 79-91.
155. Elliott, M.R., F.B. Chekeni, P.C. Trampont, E.R. Lazarowski, A. Kadl, S.F. Walk, D. Park, R.I. Woodson, M. Ostankovich, P. Sharma, et al., *Nucleotides released by apoptotic cells act as a find-me signal to promote phagocytic clearance.* Nature, 2009. **461**(7261): p. 282-6.
156. Ayna, G., D.V. Krysko, A. Kaczmarek, G. Petrovski, P. Vandenabeele, and L. Fesus, *ATP release from dying autophagic cells and their phagocytosis are crucial for inflammasome activation in macrophages.* PLoS One, 2012. **7**(6): p. e40069.
157. Ishii, K.J., C. Coban, H. Kato, K. Takahashi, Y. Torii, F. Takeshita, H. Ludwig, G. Sutter, K. Suzuki, H. Hemmi, et al., *A Toll-like receptor-independent antiviral response induced by double-stranded B-form DNA.* Nat Immunol, 2006. **7**(1): p. 40-8.
158. Paludan, S.R., *Activation and regulation of DNA-driven immune responses.* Microbiol Mol Biol Rev, 2015. **79**(2): p. 225-41.
159. Doyle, S., S. Vaidya, R. O'Connell, H. Dadgostar, P. Dempsey, T. Wu, G. Rao, R. Sun, M. Haberland, R. Modlin, et al., *IRF3 mediates a TLR3/TLR4-specific antiviral gene program.* Immunity, 2002. **17**(3): p. 251-63.
160. Stark, G.R., I.M. Kerr, B.R. Williams, R.H. Silverman, and R.D. Schreiber, *How cells respond to interferons.* Annu Rev Biochem, 1998. **67**: p. 227-64.
161. Zhang, C.Z., A. Spektor, H. Cornils, J.M. Francis, E.K. Jackson, S. Liu, M. Meyerson, and D. Pellman, *Chromothripsis from DNA damage in micronuclei.* Nature, 2015. **522**(7555): p. 179-84.
162. Harding, S.M., J.L. Benci, J. Irianto, D.E. Discher, A.J. Minn, and R.A. Greenberg, *Mitotic progression following DNA damage enables pattern recognition within micronuclei.* Nature, 2017. **548**(7668): p. 466-470.
163. Mackenzie, K.J., P. Carroll, C.A. Martin, O. Murina, A. Fluteau, D.J. Simpson, N. Olova, H. Sutcliffe, J.K. Rainger, A. Leitch, et al., *cGAS surveillance of micronuclei links genome instability to innate immunity.* Nature, 2017. **548**(7668): p. 461-465.
164. Collection, A.T.C., *ATCC Cell Lines by Gene Mutation*. 2014.
165. Ormerod, M.G. *Flow Cytometry - A Basic Introduction*. 2008 [cited 2018 4 January]; [Chapter 2 and 3]. Available from: http://flowbook.denovosoftware.com/.
166. Adan, A., G. Alizada, Y. Kiraz, Y. Baran, and A. Nalbant, *Flow cytometry: basic principles and applications.* Crit Rev Biotechnol, 2017. **37**(2): p. 163-176.
167. Snow, C., *Flow cytometer electronics.* Cytometry A, 2004. **57**(2): p. 63-9.
168. Loken, M.R., D.R. Parks, and L.A. Herzenberg, *Two-color immunofluorescence using a fluorescence-activated cell sorter.* J Histochem Cytochem, 1977. **25**(7): p. 899-907.
169. Krutzik, P.O. and G.P. Nolan, *Fluorescent cell barcoding in flow cytometry allows high-throughput drug screening and signaling profiling.* Nat Methods, 2006. **3**(5): p. 361-8.

170. Angelova, A.L., S.P. Grekova, A. Heller, O. Kuhlmann, E. Soyka, T. Giese, M. Aprahamian, G. Bour, S. Ruffer, C. Cziepluch, et al., *Complementary induction of immunogenic cell death by oncolytic parvovirus H-1PV and gemcitabine in pancreatic cancer.* J Virol, 2014. **88**(10): p. 5263-76.
171. Liu, C.C., P. Leclair, M. Monajemi, L.M. Sly, G.S. Reid, and C.J. Lim, *alpha-Integrin expression and function modulates presentation of cell surface calreticulin.* Cell Death Dis, 2016. **7**: p. e2268.
172. Zhou, H., S. Forveille, A. Sauvat, T. Yamazaki, L. Senovilla, Y. Ma, P. Liu, H. Yang, L. Bezu, K. Muller, et al., *The oncolytic peptide LTX-315 triggers immunogenic cell death.* Cell Death Dis, 2016. **7**: p. e2134.
173. Martins, I., O. Kepp, F. Schlemmer, S. Adjemian, M. Tailler, S. Shen, M. Michaud, L. Menger, A. Gdoura, N. Tajeddine, et al., *Restoration of the immunogenicity of cisplatin-induced cancer cell death by endoplasmic reticulum stress.* Oncogene, 2011. **30**(10): p. 1147-58.
174. Martins, I., A. Tesniere, O. Kepp, M. Michaud, F. Schlemmer, L. Senovilla, C. Seror, D. Metivier, J.L. Perfettini, L. Zitvogel, et al., *Chemotherapy induces ATP release from tumor cells.* Cell Cycle, 2009. **8**(22): p. 3723-8.
175. Adkins, I., L. Sadilkova, N. Hradilova, J. Tomala, M. Kovar, and R. Spisek, *Severe, but not mild heat-shock treatment induces immunogenic cell death in cancer cells.* Oncoimmunology, 2017. **6**(5): p. e1311433.
176. Block, G.J., G.D. DiMattia, and D.J. Prockop, *Stanniocalcin-1 regulates extracellular ATP-induced calcium waves in human epithelial cancer cells by stimulating ATP release from bystander cells.* PLoS One, 2010. **5**(4): p. e10237.
177. Schneider, K., V. Bol, and V. Gregoire, *Lack of differences in radiation-induced immunogenicity parameters between HPV-positive and HPV-negative human HNSCC cell lines.* Radiother Oncol, 2017. **124**(3): p. 411-417.
178. Martins, I., O. Kepp, L. Menger, M. Michaud, S. Adjemian, A.Q. Sukkurwala, E. Vacchelli, L. Galluzzi, and G. Kroemer, *Fluorescent biosensors for the detection of HMGB1 release.* Methods Mol Biol, 2013. **1004**: p. 43-56.
179. Matlock, B., *Assessment of Nucleic Acid Purity*. 2015, Thermo Scientific.
180. Mehta, A.K., S.S. Majumdar, P. Alam, N. Gulati, and V. Brahmachari, *Epigenetic regulation of cytomegalovirus major immediate-early promoter activity in transgenic mice.* Gene, 2009. **428**(1-2): p. 20-4.
181. Brooks, A.R., R.N. Harkins, P. Wang, H.S. Qian, P. Liu, and G.M. Rubanyi, *Transcriptional silencing is associated with extensive methylation of the CMV promoter following adenoviral gene delivery to muscle.* J Gene Med, 2004. **6**(4): p. 395-404.
182. Sato, H., A. Niimi, T. Yasuhara, T.B.M. Permata, Y. Hagiwara, M. Isono, E. Nuryadi, R. Sekine, T. Oike, S. Kakoti, et al., *DNA double-strand break repair pathway regulates PD-L1 expression in cancer cells.* Nat Commun, 2017. **8**(1): p. 1751.
183. Sharabi, A.B., M. Lim, T.L. DeWeese, and C.G. Drake, *Radiation and checkpoint blockade immunotherapy: radiosensitisation and potential mechanisms of synergy.* Lancet Oncol, 2015. **16**(13): p. e498-509.

10 Appendix

Centrifuge speed to gravitational force:

Table A.1. Table showing the relative centrifugal force in x g (RCF) for the centrifuge speeds used in the project (rounds per minute, RPM). The use of the different centrifuges and speeds refers to the text of the thesis. Values calculated by use of the formula $g = (1.118 \cdot 10^{-5})R\,S^2$, where *g* is gravitational force, *R* is the centrifuge radius in centimetres and *S* is the centrifuge speed in RPM.

Use	RPM	Centrifuge	Approx. rotor radius (cm)	RCF (x g)
Cell harvest	1500	Himac CT6E	16.19	407.25
Cell staining	1500	Rotina 380 R	20.99	528.00
ATP assay	13400	Eppendorf MiniSpin	6.027	12100.0

Cytometer settings and lasers:

Table A.2. Table showing the flow cytometer settings used for detection of chosen parameters in the project.

Parameter:	Laser:	Supplier	Bandpass filter (nm):	Longpass dichroic filter (nm)
Alexa Fluor 488	Blue, 488nm (20mW)	Coherent	530/30	505
Hoechst	UV, 355nm (20mW)	JDSU	450/50	-
Propidium iodide	Blue, 488nm (20mW)	Coherent	610/20	600
GFP	Blue, 488nm (20mW)	Coherent	530/30	505
Pacific blue	Violet, 405nm (13mW)	Coherent	450/50	-
FxCycle Far Red	Red, 633nm (20mW)	JDSU	660/20	-

Calculation of cell area when the volume doubles:

$$V = \frac{4}{3}\pi r^3$$

$$2 \cdot V = 2 \cdot \frac{4}{3}\pi r^3$$

$$\frac{4}{3}\pi(r \cdot x)^3 = 2 \cdot \frac{4}{3}\pi r^3$$

$$(r \cdot x)^2 = 2r^2$$

$$\underline{x = \sqrt[3]{2}}$$

$$A_{2 \cdot V} = 4\pi(\sqrt[3]{2} \cdot r)^2 = 4\pi \cdot \sqrt[3]{2^2} \cdot r^2$$

Equation A.1. Shows the calculation of the increase in radius when the volume of a sphere doubles, and how this would increase the surface area.

Plasmid isolation purity curve:

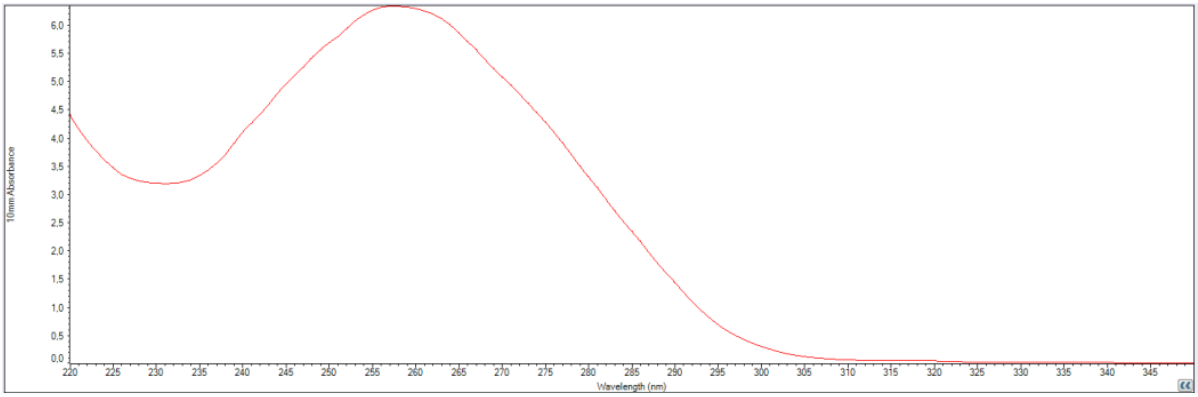

Figure A.1. Figure showing the absorbance curve for the final *GFP-HMGB1* plasmid solution at a distance of 10mm. Along the x axis is the wavelength in nm, whilst the y axis shows the relative absorbance.

Note on figures:

Figure 1.2, 1.5-6, 1.10-11, 2.1, 4.2-3, 5.3, 5.7, 5.11, 5.17 and 5.22 were made with elements from the free-of-use medical illustration collection SMART Servier Medical Art by *Laboratoires Servier*.